# *Stellar Tracers*

# *—and—*

# *Galactic Exploration*

A Disseration by John J. Vickers

Dissertation
submitted to the
Combined Faculties of the Natural Sciences and Mathematics
of the Ruperto-Carola-University of Heidelberg. Germany for the degree of
Doctor of Natural Sciences

Put forward by:
John J Vickers
Born in: West Melbourne, Florida, United States of America
Oral examination: November 27, 2014

# Stellar Tracers and Galactic Exploration

**Referees**

Professor Eva K. Grebel

—and—

Doctor Coryn Bailer-Jones

# Abstract

This dissertation discusses various techniques for studying the structure of the Milky Way via the use of stellar tracers. One of the most widely used stellar tracers is blue horizontal branch stars, which are prized for their predictable and substantial intrinsic brightnesses and their old ages. We begin by creating a $z$ based photometric color cut for the selection of blue horizontal branch stars which may be used in data produced by the Panoramic Survey Telescope and Rapid Response System. Using this color cut, we select a sample of blue horizontal branch stars and pass them through a newly devised search algorithm which is capable of finding overdensities in incomplete and patchy data. From this, we rediscover a number of well known Milky Way features and discover a new constraining detection of the Sagittarius tidal streams.

If we use spectroscopy in addition to photometry, we can isolate another stellar tracer, main sequence stars. A main sequence star's intrinsic magnitude is a function primarily of the mass and metallicity of the star; so with spectroscopy and photometry we can easily estimate the distance to these types of objects.

We collect a sample of F-M type dwarf stars from the Sloan Digital Sky Survey spectroscopic data set. Having spectroscopy and astrometry, we may assign six-dimensional phase information to these objects and then use that information to study their bulk motions as a function of position. Here, instead of looking for large structure, we instead look to aberrations from large structure: using this relationship between motion and position as a probability density function, we select and characterize significant outliers. We also identify phenomenological objects such as hypervelocity and Hills stars. These types of stars are indirect probes of the Milky Way and are most useful for studying: the potential of the Milky Way, the locations of extreme overdensities such as spiral arms or black holes, and the structure of observationally obscure areas like the Galactic nucleus.

During these studies of the motions and positions of stellar tracers in the Milky Way, accurate reports of the proper motions are of critical importance. To investigate this we closely examine proper motions in the Sloan Digital Sky Survey and the PPMXL proper motion catalogs and devise metrics for estimating the accuracy of these proper motion valuations and corrections to erroneous proper motions where applicable.

# Zusammenfassung

Diese Dissertation befasst sich mit verschiedenen Techniken zur Untersuchung der Strukturen der Milchstraße mit Hilfe von ausgewählten Sternen. Zu den am Häufigsten verwendeten Sternen zählen die des blauen Horizontalastes. Diese sind bekannt für die Intensität ihrer intrensischen Helligkeit sowie ihr hohes Alter. Im ersten Teil der Arbeit beginnen wir mit der farblichen Einschränkung der Sterne des blauen Horizontalastes basierend auf der Photometrie des $z$-Filters. Diese Einschränkung kann anschließend auf den Daten des Panoramic Survey Telescope und Rapid Response System angewandt werden. Mit Hilfe dieser Farbeinschränkung können wir Sterne des blauen Horizontalastes herausfiltern und diese einem neu entwickelten Suchalgorithmus übergeben, der in der Lage ist, Überdichten in unvollständigen oder lückenhaften Daten zu finden. Damit haben wir eine Vielzahl schon bekannter Strukturen der Milchstraße gefunden, sowie eine neue, einschränkende Detektionsmethode für den Sagittarius - Gezeitenstrom entdeckt.

Wenn wir zusätzlich zur Photometrie auch Spektroskopie benutzen, können wir noch eine weitere Sternenklasse hinzunehmen: die Hauptreihensterne. Die intrinsische Helligkeit dieser Hauptreihensterne ist hauptsächliche eine Funktion der Masse sowie der Metallizität. Somit können wir mit der Photometrie in Kombination mit der Spektroskopie sowohl die Typen, als auch die die Entfernungen dieser Objekte abschätzen.

Im zweiten Teil nutzen wir zunächst die spektroskopischen Daten einer Auswahl an F-M Zwergen aus dem Sloan Digital Sky Survey. Die Spektroskopie zusammen mit der Astrometrie gibt uns einen sechsdimensionalen Phasenraum. Mit diesen Informationen sind wir in der Lage, die Bulkbewegung dieser Objekte, als Funktion der Position, zu untersuchen. Anstatt uns auf großräumige Strukturen zu konzentrieren, schauen wir auf Abweichungen von diesen: Mit Hilfe des Zusammenhangs zwischen Bewegung und Position als Dichtefunktion, können wir signifikante Ausreißer bestimmen und diese charakterisieren. Wir identifizieren auch phänomenologische Objekte wie Hyperschnellläufer und Hillsterne. Diese Klassen von Sternen sind die geeignetsten zur Untersuchung des Milchstraßenpotenzials, der Lage von extremen Überdichten wie Spiralarme und der Strukturen von schlecht zu beobachtenden Stellen, wie zum Beispiel den Galaxienkern.

Für die Untersuchungen der Bewegung und Positionen dieser ausgewählten Sterne in der Milchstraße, sind genaue Informationen über die Eigenbewegung von unschätzbarer Wichtigkeit. Deswegen haben wir diese Eigenbewegung im Sloan Digital Sky Survey und im PPMXL Eigenbewegungskatalog auf das genaueste untersucht und eine Metrik entworfen, welche die Genauigkeit dieser Eigenbewegung abschätzt und diese, wenn nötig, korrigiert.

*'Twas brillig, and the slithy toves*
*Did gyre and gimble in the wabe:*
*All mimsy were the borogoves,*
*And the mome raths outgrabe.*

*"Beware the Jabberwock, my son!*
*The jaws that bite, the claws that catch!*
*Beware the Jubjub bird, and shun*
*The frumious Bandersnatch!"*

*He took his vorpal sword in hand:*
*Long time the manxome foe he sought–*
*So rested he by the Tumtum tree,*
*And stood awhile in thought.*

*And, as in uffish thought he stood,*
*The Jabberwock, with eyes of flame,*
*Came whiffling through the tulgey wood,*
*And burbled as it came!*

*One, two! One, two! And through and through*
*The vorpal blade went snicker-snack!*
*He left it dead, and with its head*
*He went galumphing back.*

*"And, has thou slain the Jabberwock?*
*Come to my arms, my beamish boy!*
*O frabjous day! Callooh! Callay!"*
*He chortled in his joy.*

*'Twas brillig, and the slithy toves*
*Did gyre and gimble in the wabe;*
*All mimsy were the borogoves,*
*And the mome raths outgrabe.*

- Lewis Carroll

# Contents

# List of Figures

# List of Tables

# Abbreviations

| | |
|---|---|
| **2MASS** | **2** Micron **A**ll **S**ky **S**urvey |
| **BHB** | **B**lue **H**orizontal **B**ranch |
| **FWHM** | **F**ull **W**idth at **H**alf **M**aximum |
| **ICRS** | **I**nternational **C**elestial **R**eference **S**ystem |
| **LAMOST** | **L**arge Sky **A**rea **M**ulti-**O**bject Fibre **S**pectroscopic **T**elescope |
| **LSD** | **L**arge **S**urvey **D**atabase |
| **MSA** | **M**ain **S**equence **A** |
| **Pan-STARRS** | **Pan**oramic **S**urvey **T**elescope **A**nd **R**apid **R**esponse **S**ystem |
| **PSF** | **P**oint **S**pread **F**unction |
| **QSO** | **Q**uasi **S**tellar **O**bject |
| **RAVE** | **RA**dial **V**elocity **E**xperiment |
| **SDSS** | **S**loan **D**igital **S**ky **S**urvey |
| **SMBH** | **S**uper **M**assive **B**lack **H**ole |
| **UCAC** | **U**SNO **C**CD **A**strograph **C**atalog |
| **USNO** | **U**nited **S**tates **N**aval **O**bservatory |
| **WISE** | **W**idefield **I**nfrared **S**urvey **E**xplorer |

# Chapter 1

# Introduction

In general, studying the structure of a system requires just the three dimensional locations of the objects within the system. And studying the dynamics of a system requires just the locations and motions – or six dimensional phase information of the objects within the system – and some inferred physical laws. Add in chemistry – metallicity, alpha abundances, chemical fingerprinting – and you have Galactic exploration.

In this dissertation, we will cover a variety tools and techniques that are all aimed at one overarching question: what is the structure of the Milky Way. This question has several aspects: for example the structure of the stars in the Milky Way, with the stars concentrated in a disk with clumpy spiral arms radiating outward and lumpy dwarf galaxies and clusters orbiting, is entirely different from the inferred structure of the dark matter halo, which is thought to be a triaxial spheroid with a generally smoothly decreasing radial density with small lumps floating about.

We first look at the question directly: what is the observable structure of a portion of the Milky Way, the stellar halo. To do this, we use data from the new Panoramic Survey Telescope and Rapid Response System and investigate blue horizontal branch stars – or, more precisely, overdensities of blue horizontal branch stars. In general blue horizontal branch stars reside in a flattened spheroidal distribution of the Milky Way's halo; however, this smooth halo is peppered with dense streams, clusters, and dwarf galaxies. In the large footprint of this survey, we characterize well known structures, such as the Sagittarius tidal tails, in new areas uncovered by similar surveys.

Next we explore a new idea for studying structure indirectly: looking at extreme outliers. In general stars in the Milky Way, and all systems, behave in predictable ways, usually traveling in smooth orbits along with stellar siblings. However, sometimes stars are seen flying alone at extreme speeds out of systems – this is an indication that the star interacted with some sort of overdense system which strongly perturbed it into a new phase space. By looking at objects flying on these incongruous orbits and calculating their positions back in time, we can find the locations of where these objects originated, and this will tell us where large overdensities are when we cannot necessarily observe. We use this idea to indirectly look at the positions of the Milky Way spiral arms and the orientations of planes of matter in the galactic nucleus.

An important part of all of this is the accurate determination of the positions and velocities of the stars we observe, so we also spend time assessing and correcting proper motion estimates from various catalogs so as to have the most reliable information possible. This is critical for identifying legitimate outlier stars.

Here we will briefly outline the data we use and talk about our topics of study in a bit more depth before beginning the Dissertation proper. At the end, we close with a brief review.

## 1.1 Surveys Used in this Work

This thesis presents a number of large data set analyses. All the data used drawn from public and still proprietary surveys and then analyzed in bulk. The main challenges of this thesis are the identification of certain types of objects using photometry and spectroscopy, and then analyzing the structural density and kinematics of the selected populations.

For example in Part I we first identify blue horizontal branch stars [BHB stars] on the basis of their Sloan Digital Sky Survey [SDSS; York et al. (2000)] spectra in order to define photometric descriptions which may be used to separate these objects from other hot objects by use of photometry only: this technique is then extended to be used on data from the Panoramic Survey Telescope and Rapid Response System survey [Pan-STARRS; Kaiser et al. (2010)]. In Part II we use SDSS spectroscopy to identify main sequence stars and then calculate the bulk motions of all main sequence stars in order to find kinematic outliers. In Part III we use data from the Wide-Field Infrared Survey Explorer survey [WISE; Wright et al. (2010)] and the 2 Micron All Sky Survey [2MASS; Skrutskie et al. (2006)] to identify Galactic and extragalactic objects and then analyze their respective proper motions in the PPMXL proper motion catalog (Roeser et al., 2010).

The main observational aspects of these surveys are detailed in Table 1.1, and their filter curves are shown in Figure 1.1.

It would be useful to introduce some nomenclature at this juncture. In general, throughout the Dissertation we make use of the extinction maps of Schlegel et al. (1998). These extinction maps are produced by comparing the colors and magnitudes of external elliptical galaxies. In general we use the subscript '0' to denote an object which has been dereddened using these extinction maps. These maps are generally only used for Galactic studies at high latitudes however, since at low latitudes the full column density is the only information available which would wildly overestimate the extinction for nearby objects in the plane of the Milky Way.

We will also use the subscripts 'SDSS' and 'PS' at various points to differentiate between SDSS and Pan-STARRS data since their filter sets are similar but unique.

The following is a brief summary of the surveys:

### 1.1.1 The Sloan Digital Sky Survey

The SDSS is a long-running survey [the first data release being more than a decade ago, see Stoughton et al. 2002] which, as of the tenth data release (Ahn et al., 2014), has imaged over a third of the sky in five photometric bands [$ugriz_{SDSS}$: for information on the survey strategy, see York et al. 2000; for information on the filters and imager, see Fukugita et al. 1996 and Gunn et al. 1998, respectively]. The SDSS 2.5 meter telescope is situated at Apache Point Observatory in New Mexico.

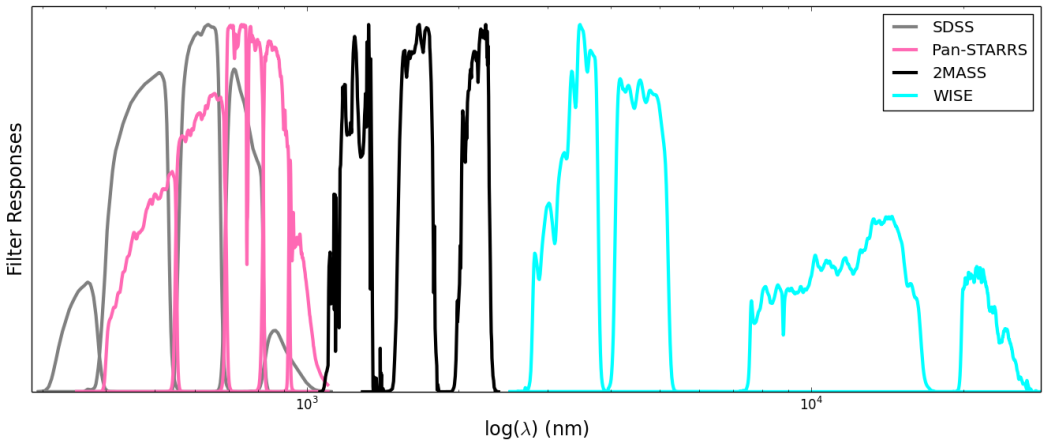


FIGURE 1.1: The filter efficiency curves for the data sets utilized in this thesis.

| Survey | Filter | Wavelength | Magnitude Range | FWHM (arcseconds) | Coverage |
|---|---|---|---|---|---|
| SDSS | | | | | 2/3 Sky |
| | u | 3551 Å | 12.0 - 22.0 | 0.56 | |
| | g | 4686 Å | 14.1 - 22.2 | 1.37 | |
| | r | 6165 Å | 14.1 - 22.2 | 1.37 | |
| | i | 7481 Å | 13.8 - 21.3 | 1.51 | |
| | z | 8931 Å | 12.3 - 20.5 | 0.94 | |
| Pan-STARRS | | | Variable | | 3$\pi$ Sky |
| | g | 481 nm | | 0.99 | |
| | r | 617 nm | | 0.98 | |
| | i | 752 nm | | 0.9 | |
| | z | 866 nm | | 0.72 | |
| | y | 962 nm | | 0.89 | |
| 2MASS | | | | | All Sky |
| | J | 1.25 $\mu$m | 9.0 - 15.8 | 2.9 | |
| | H | 1.65 $\mu$m | 8.5 - 15.1 | 2.8 | |
| | K | 2.17 $\mu$m | 8.0 - 14.3 | 2.9 | |
| WISE | | | | | All Sky |
| | W1 | 3.4 $\mu$m | 8.1 - 16.6 | 6.1 | |
| | W2 | 4.6 $\mu$m | 6.7 - 15.6 | 6.4 | |
| | W3 | 12.0 $\mu$m | 3.4 - 11.3 | 6.5 | |
| | W4 | 22.0 $\mu$m | -0.4 - 8.0 | 12.0 | |

TABLE 1.1: Summary of the coverage, effective wavelengths, and magnitude ranges of the data used in this thesis. Note that in Pan-STARRS we use the magnitude range 'variable;' this is because there are no published magnitude limits and in many ways it is difficult to assign global limits owing to the differential coverage across the sky. It is usually up to the researcher to determine what magnitude ranges they find acceptable.

The survey is performed in drift-scan mode, an observing strategy where the telescope pointing is stationary and the sky is allowed to pass over the detector. The survey strategy was initially extragalactically motivated as can be seen in the choice of a high Galactic latitude footprint with a few 'spider legs' crossing the plane. The narrow filter set is most useful for hunting down high redshift objects, and the use of the $u_{SDSS}$ filter is useful for identifying quasi-stellar objects [QSOs; (Richards et al., 2009)].

This drift-scan technique notable because of its simultaneous collection of data in all five of the SDSS filters as well as its overlapping stripes survey strategy, which allows for greater accuracy übercalibration[1], since photometry is taken in all bands at the same time in identical observing conditions.

The SDSS telescope is also outfitted with twin multifiber spectrographs which can take up to 640 spectral readings simultaneously on 3" fibers. The spectrographs operate over the visual range [3900Å to 9000Å] at a moderate resolution [R∼1850 - 2200]. Originally it was anticipated that the project would capture one million galaxy spectra and 100,000 quasar spectra.

However, it was quickly noticed that, although the survey proved illuminating in its primary mission of extragalactic exploration, is was also proficient at elucidating the mysteries of our own Milky Way and its complex formation history [see for example Yanny et al. 2000, Newberg et al. 2002, Belokurov et al. 2006 and references therein]. As such, additional programs, such as the 'Sloan Extension for Galactic Understanding and Exploration' [SEGUE; (Yanny et al., 2009)] shifted spectroscopic observing time away from extragalactic objects and targeted stars in our own Milky Way. The SEGUE project papers and SDSS websites[2] outline the basic information pertaining to the stellar spectroscopy.

The SEGUE Stellar Parameters Pipeline [SSPP, see Lee et al. 2008] database is also available on the SDSS website and provides atmospheric parameter estimates, calculated by a variety of methods, for the entire spectroscopic database.

The SDSS data products also offer an internal proper motion table (Munn et al., 2004) where proper motions are obtained by comparing United States Naval Observatory astrometry [USNO; Monet et al. 2003] and SDSS astrometry. The proper motions are obtained by comparing earlier photographic plate surveys and the SDSS observations; they use the SDSS galaxy sample as a stationary reference frame. This catalog of proper motions is 90% complete to $g_{SDSS} \sim 19.7$.

### 1.1.2 The Panoramic Survey Telescope And Rapid Response System

The Pan-STARRS survey is carried out by a 1.8 meter optical telescope located at Haleakala Crater in Hawaii. The project initially called for four telescopes and the second telescope is currently under construction; but in this Dissertation we only use data from the Pan-STARRS 1 prototype telescope. This telescope uses a 'point-and-shoot' survey strategy, and features photometric passbands modeled after the SDSS passbands [see Figures 1.1 and 4.1]. While not exactly the same, the filters are close enough to adapt science strategies used by the SDSS to the Pan-STARRS data.

The survey's main project is near earth object and transient studies [supernovae detection and alerts, pulsating variables, etc.]. As such, much of the survey is conducted using an ultra-wide $w_{PS}$ filter, whose only purpose is to collect as much light as possible to detect solar system objects. The survey is performed by using many short pointings as opposed to a few long ones. By introducing a cadence

[1] Übercalibration is the process by which photometry in different areas of the sky is brought into global agreement by comparing overlaps of the observing fields and bootstrapping to the whole survey.

[2] http://www.sdss3.org/

into the photometric data product, you unlock the realm of 'time domain astronomy' and enable the discovery of all sorts of transient objects – from supernovae to pulsating stars – at the cost of non-uniform conditions between observations in the same or different filters. This makes übercalibration more difficult; although, great efforts are being made to übercalibrate the survey to a photometric precision greater than that of the SDSS [see Schlafly et al. 2012].

Pan-STARRS is also a $3\pi$ survey, extending down to $\delta$ =-30° so it has a little more than twice as much coverage as the SDSS survey. Also, unlike the SDSS survey, Pan-STARRS is peering into the plane of the Milky Way instead of avoiding it. This enables it to perform many exciting new studies in the bulge and anticenter regions; the SDSS only observes these regions in sparse 'spider leg' paths.

One of Pan-STARRS most notable contributions is the publication of a large-footprint, three dimensional dust map (Schlafly et al., 2014), which will vastly enhance the accuracy of photometric studies within the disk. While not all-sky as the maps of Schlegel et al. (1998), it still covers a significant area.

It is worth noting that Pan-STARRS has no in-house spectrograph; however the Chinese Large Sky Area Multi-Object Fibre Spectroscopic Telescope [LAMOST; Cui et al. 2012] is collecting a vast amount of spectra in the plane of the disk at similar resolution to the SDSS spectral library; this will vastly aid in kinematic studies which are outside of the SDSS footprint.

### 1.1.3 The Two Micron All Sky Survey

The 2MASS was an all sky survey which used two 1.3 meter telescopes to scan the sky in three infrared bands. The northern telescope was at Mt. Hopkins, Arizona, and the southern hemisphere telescope was located at Cerro Tololo Inter-American Observatory, Chile.

The science goals of the 2MASS survey were mainly aimed at low mass stellar studies, brown dwarf characterization and the detection of galaxies in the so called 'zone of avoidance.' However, as expected, some of its most famous science results came from alternative studies, such as the characterization of the Sagittarius tidal tails [originally discovered by Ibata et al. (1994)] in K and M giants by Majewski et al. (2003).

The 2MASS catalog is also used in the creation of the PPMXL proper motion catalog of Roeser et al. (2010) by crossmatching 2MASS data with USNO-B data.

### 1.1.4 The Wide-field Infrared Survey Explorer

The WISE survey is relatively new and the only space based survey used in this work. It has a 0.4 meter aperture and images the sky in 4 infrared bands ranging from near to far infrared. It has been used to study asteroids, planetary nebula, distant galaxies, and discovered the first Y-dwarf stars (Kirkpatrick et al., 2011).

It is an all sky survey which covered the entire sky 8 times. Its ten month mission was supplemented by a four month mission to hunt near earth objects after the hydrogen coolant was depleted – then it was placed into hibernation.

We use it because of a serendipitous discovery in Kovács & Szapudi (2013) and Pradhan et al. (2014), where it was found that 2MASS J and WISE W1 produce a strong color cut between galaxies and stars. The selection is much stronger than the discrimination allowed by the large full width at half maximum [FWHM] of 2MASS alone.

## 1.2 Introduction to Topics Presented in This Dissertation

### 1.2.1 Blue Horizontal Branch Stars and the Galactic Halo

The horizontal branch feature of the color-magnitude diagram [see Figure 1.2] has long been used as a standard candle in Galactic astronomy. Essentially, the horizontal branch may be thought of as analogous to the main sequence. The physical difference between the two branches is that stars on the main sequence are core hydrogen burning while stars on the horizontal branch have already completed hydrogen burning, risen up the red giant branch, and now burn helium in their cores with a shell of hydrogen burning around the core [see Section 5.1.2 of Binney & Merrifield 1998 pp. 263-267]

The horizontal branch has quite a range in color space, extending from $0.3 < (g\text{-}i)_{PS,0} < 0.5$, or even bluer if one considers the 'extreme horizontal branch' [although here it is no longer 'horizontal,' see Figure 1.2] stars which are thought to be post aysmptotic giant branch stars. In metal rich populations, the horizontal branch will be redder and stubbier. Metal poor populations have horizontal branches extending to much bluer colors and sometimes growing to include extreme horizontal branch stars. Blue horizontal branch [BHB] stars are generally very old [$\geq$12 Gyr in many globular clusters, Dotter et al. 2010], and metal poor – which makes them ideal for studying old halo populations and for contrasting old and young populations in the same substructures [as done by Bell et al. 2010 using old BHB stars and younger main sequence turnoff stars]. The horizontal and extreme horizontal branches have shapes that are generally thought to vary as functions of age, metallicity and helium abundance.

Between the 'red' and 'blue' horizontal branches, there is a region known as the 'RR Lyrae gap' which is home to the pulsating horizontal branch stars, RR Lyrae. This region falls into the instability strip as do other pulsating stars like Cepheids [in the red giant area of the color magnitude diagram] and ZZ Ceti [in the white dwarf regime]. RR Lyrae are commonly used standard candles as well, and enjoy growing popularity as multi-epoch surveys such as – SDSS Stripe 82, Pan-STARRS, and the upcoming Large Synoptic Survey Telescope (Ivezic et al., 2008) – become more prolific [see for example Sesar et al. 2010 and Abbas et al. 2014].

As mentioned, the horizontal branch, especially the blue horizontal branch [BHB] is a prized distance indicator for Galactic studies [e.g. Clewley & Jarvis 2006, Ruhland 2011, Wilhelm et al. 1999, Xue et al. 2008] owing to the steadiness of the absolute magnitude with respect to color and their intrinsic brightness. To a first order approximation, the horizontal branch can be assumed to be at about a constant magnitude of 0.7 in $g_{SDSS}$; although it is preferable to do actual fits of absolute magnitude versus color [as in Deason et al. (2011) and Section 4.1].

The color magnitude diagram is sparsely populated in the hot color range of the blue horizontal branch [from about 7,000 K to 10,000 K], which is a boon when trying to remove contaminating objects. The most common contaminants are white dwarfs, quasars and main sequence A [MSA] stars.

The most accurate way to separate a BHB star from these contaminants is via spectroscopy. Spectral templates will immediately eliminate white dwarf and quasar contamination [as white dwarfs have very broad absorption lines, and quasars have strong emission rather than absorption lines]. To separate MSA stars from BHB stars spectroscopically, two main approaches exist: first a comparison of Balmer line depth [$f_m$] and broadening [$D_{0.2}$] caused by the different surface temperatures and surface gravities, respectively [see Pier 1983], of the stars; and secondly the scale-width-shape method described by Clewley et al. (2002) which separates the two species based on the Balmer line fits to a Sérsic profile.

In the absence of spectroscopic data however, photometric methods may be applied to separate BHB stars from other blue species. This has been shown to be quite effective in several studies. For example:

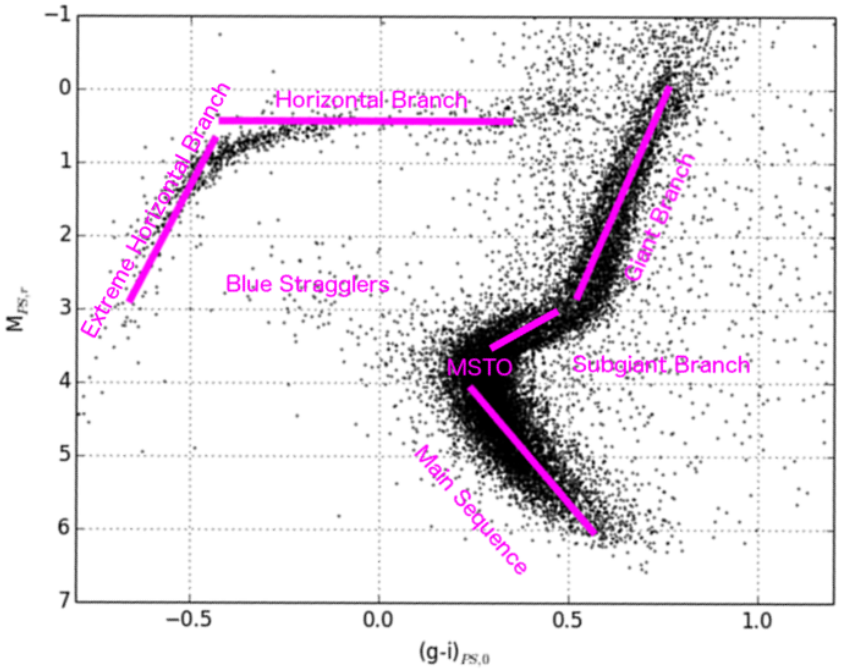


FIGURE 1.2: Combined color-magnitude diagram of all globular clusters in the Pan-STARRS footprint which are above $|b| > 30°$. The globular cluster photometry is collected within half a tidal radius of the objects and then is put onto an absolute magnitude scale in order to be coplotted with the data from the other clusters. Tidal radii and distances are drawn from the catalog of Harris (1996), 2010 revision. The diagram is annotated with various features which emerge as a result of stellar evolution. In this work we are most interested in the horizontal branch and the main sequence features of the diagram. Evidence for metallicity differences between the clusters are apparent in the color spread of the red giant branch and the main sequence turnoff, as well as in the spread in color of the horizontal branch.

Yanny et al. (2000) demonstrated a filter cut in the SDSS which separates BHB stars from MSA stars adequately enough to discern significant structure in the plane of the celestial equator; Sirko et al. (2004) use a 'stringent' cut similar to that proposed by Yanny et al. (2000) on the basis of spectroscopic data and a combination of the scale-width-shape method and the $D_{0.2}$ and $f_m$ methods in their kinematic studies of the Galactic halo; more recently Bell et al. (2010) further refine this 'stringent' cut in their investigation of the ratios of BHB to main sequence turn off stars in the halo.

This color splitting was predicted by Lenz et al. (1998) using Kurucz model spectra and SDSS filter response curves. They suggested that optimal gravitational separation for blue A-type stars lies in the $(u-g)_{SDSS,0}$ color space, but also that $(i-z)_{SDSS,0}$ color was usable to split A type stars.

The reason for this separation between MSA stars and BHB stars is because of the gravitational sensitivity of the widths of absorption lines in the stars' spectra. The Balmer and Paschen breaks occur when an electron transfers between the $\infty^{th}$ and $2^{nd}$, $3^{rd}$ [respectively] energy levels. According to the Rydberg formula –

$$\frac{1}{\lambda} = R_H \left( \frac{1}{m^2} - \frac{1}{n^2} \right), \tag{1.1}$$

where $R_h = 1.097 \times 10^7 m^{-1}$ is Rydberg's constant – these breaks occur at 365 nm [in the $u$ band] and 820 nm [in the $z$ band]. At the positions of these breaks, many absorption lines overlap, and so gravitational widening of the features can have a noticable effect on the strength of the continuum as a whole in these regions, and can therefore change the amount of flux relative to other parts of the spectra. This is what causes MSA stars and BHB stars to have different colors in these bandpasses.

This gravitational splitting in the $z_{SDSS}$ band is a serendipitous development with regards to the ongoing Pan-STARRS project, which has a $z_{PS}$ band but no band analogous to the $u_{SDSS}$ band. By implementing a $z_{PS}$ based selection for BHB stars, we can begin to explore the Galactic halo using Pan-STARRS data. This is exciting because Pan-STARRS covers a much larger area of sky, to fainter magnitudes, than the SDSS.

### 1.2.2 Main Sequence Stars and Runaways

The term 'runaway' has traditionally been used to describe O and B stars which are found in the Galactic halo. Since O and B type stars require gas rich, high density environments to form, their presence far from the Galactic disk is puzzling. Adding to the confusion is the observation that these stars may have intrinsically large peculiar velocities, which is difficult to explain if one assumes that these stars did in fact form in the Galactic disk. Several theories have been posited to explain how these stars may have been ejected from the populations they were born into.

The first theory is the so-called *Binary Ejection Mechanism*. Proposed by Blaauw (1961), this theory postulates that these runaway stars originated in binary systems and were 'kicked' out of their systems by the death of their companions. If the companion goes supernova, its gravitational attraction will be greatly lessened by the shedding of mass, which can unbind the runaway and send it into the field. Additional effects may come from asymmetric explosions which are known to impart large kicks [sometimes in excess of of 1000 km $s^{-1}$] to the neutron star remnant (Scheck et al., 2006). This mechanism usually yields a runaway with a velocity similar to that of its pre-dissociated orbital velocity.

The second theory, the *Dynamical Ejection Mechanism*, was suggested by Poveda et al. (1967). In the case of binary systems interacting with another very massive star, one member of the binary may be captured by the interloping star, while the other could be ejected with high velocity [several hundred km $s^{-1}$, Gvaramadze et al. 2009]. Similar effects could occur in interacting binaries (Leonard & Duncan, 1990), or dynamically unstable tertiary systems. In these interactions, the kick imparted is usually close to the orbital speed of the binary components, but may be as large as the escape velocity from the surface of the most massive interacting object (Gvaramadze, 2009). This process is expected to dominate in crowded regions such as star clusters. In the low velocity regime, this mechanism is responsible for 'stellar evaporation' and leads to the observed mass segregation in clusters.

A third ejection process, involving interaction of a binary system with a black hole, operates in much the same way as the dynamical ejection mechanism [in the case of a binary colliding with a massive star] but is capable of imparting much larger kicks due to the extreme mass of the black hole. This method of ejection is known as the *Hills Mechanism* (Hills, 1988). Stars ejected in such a manner were observationally confirmed first by Brown et al. (2005) and later shown to have non-isotropic distributions (Brown et al., 2012). This anisotropy is thought to be an effect of the accretion patterns of the supermassive black hole in the center-most regions of the Galaxy.

A fourth process, capable of imparting kicks of a few hundred km $s^{-1}$, the *Turbovelocity Ejection Mechanism*, occurs when single stars are tidally disrupted by interaction with super massive black holes [SMBH; Manukian et al. 2013]. The star, orbiting the SMBH at a radius near the disruption radius, will develop asymmetric tidal tails in its atmosphere. As the interior tidal tail becomes strongly

bound to the SMBH, orbital energy exchange is possible between this tail and the core of the star: this allows for a 'kick' to eject the star from the SMBH's sphere of influence.

### 1.2.3 Proper Motions and Proper Motion Catalogs

Proper motions are calculated in many different ways, and each method has various benefits.

Some catalogs use the Hipparcos (ESA, 1997) and Tycho catalogs as a standard as they are the primary realizations of the International Celestial Reference System [ICRS[3], Fey et al. 2009]. For example the USNO CCD Astrograph Catalog [UCAC; Zacharias et al. 2000] catalog combines SuperCosmos[4] (Hambly et al., 2001) Schmidt plate scans with observations from the USNO CCD instrument which was first located at Tololo Interamerican Observatory in Chile and later moved to the Naval Observatory Flagstaff Station in Arizona. The long baseline between the two surveys allows for relative proper motions to be calculated, which are then made absolute by comparison to the Tycho-2 catalog. The PPMXL proper motion catalog is similar, but uses USNO-B data [collected from almost 7500 photographic plates; Monet et al. 2003] and matches it to 2MASS data instead, before comparing to the Tycho-2 catalog.

The main advantage of this method is the existence of a standard reference frame which is clearly defined [the system of Hipparcos] and communicable between all surveys.

Another method is to use galaxies and quasars as the reference frame, and to calculate proper motions relative to that frame. This is the approach favored for the SDSS internal proper motions; calculated by Munn et al. (2004), the SDSS proper motions again use the USNO-B catalog for the long time difference, but then force the system into agreement with *external galaxies* instead of into the Hipparcos system.

The main advantage of this method lies in the sheer number of galaxies and quasars observed by the SDSS which provides a very stable background to calculate relative proper motions against.

One weakness of all of the above methods is, strangely, one of their greatest strengths. The long time baseline that allows for more accurate recording of [particularly small] proper motions requires that data from photographic plates be used. It is known that many plates have plate-dependent distortions and larger positional errors than modern instruments. To combat this, it has recently come into vogue to calculate internal only proper motions using only observations of modern, high resolution surveys.

The best examples of this are the stripe 82 re-reductions of Bramich et al. (2008) and Koposov et al. (2013) who constructed their own proper motions by considering the seven years of SDSS reimaging in stripe 82. This usually results in much smaller proper motion errors owing to the more precise position determination on modern instruments. The Pan-STARRS project is also working on calculating internal proper motions in such a way.

## 1.3 This Dissertation

This Dissertation is split into three separate parts: Part I, 'Blue Horizontal Branch Stars and the Galactic Halo,' a direct observation of the structure of the Milky Way's halo; Part II, 'A Fresh Look

[3]http://hpiers.obspm.fr/icrs-pc/icrf2/icrf2.html

[4]The SuperCosmos project is the primary effort for digitizing the UK Schmidt, ESO Schmidt, and Palomar photographic plate data. See: http://www-wfau.roe.ac.uk/sss//surveys.html

at Runaway Stars,' an indirect look at overdensities in the Milky Way via ejected stars; and Part III, 'An Examination of Proper Motions,' an important study of proper motions estimates which is used in Part II.

In Part I, we look at a photometric technique, first used by Yanny et al. (2000) to identify BHB stars based on their SDSS colors. This technique was designed for use using the $u_{SDSS}$, $g_{SDSS}$ and $r_{SDSS}$ filters. It was shown that this photometric separation was tied to the widths of the Hydrogen Balmer series absorption lines theoretically by Lenz et al. (1998); and the connection between spectroscopic line shapes and photometric colors was shown empirically by Sirko et al. (2004). We expand upon this work by instead examining the hydrogen Paschen series of absorption lines. This is an important investigation due to the up and coming Pan-STARRS data products which will not include $u_{SDSS}$ band photometry, the band in which the 'Balmer break' occurs, but instead features a sensitive $z_{PS}$ band, the band in which the analogous 'Paschen break' occurs. We show that using the Paschen lines for BHB star identification is possible both spectroscopically and photometrically. We go on to use this technique to study the physical structure of the Halo in the Pan-STARRS footprint. We find, similar to others, that the Galactic halo is not just a smooth distribution, but also hosts a variety of compact and extended regions which are overdense with BHB stars. We find a number of features which have not been noted in BHB stars before, especially in the areas of the sky covered by Pan-STARRS but not the SDSS.

In Part II, we indirectly investigate the density of the Milky Way, or rather extreme perturbations in the density, by investigating stars which have been kicked into extreme phase space coordinated by interacting with overdense potentials. These overdense potentials could be caused by singularities like black holes, or more generally by the lumpy structure of baryons in the Milky Way, lumpy structures like the spiral arms. When a star gets close to these overdensities, the opportunity for a dynamical interaction to expel the star becomes much higher than if the star is in a quiescent space.

It has long been known that stars are sometimes ejected from their birth populations into anomalous velocity spaces via various dynamical effects. These stars are known by the blanket term of 'Runaway Stars,' with special types of 'Runaway Stars,' such as 'Hypervelocity' and 'Hills' stars, being defined by special ejection scenarios. In previous literature, however, the main approach for studying these stars has revolved around identifying such outliers as 'young stars far away from young star environments' [see for example: Brown et al. (2005) or Gvaramadze (2009)]. Since large number spectroscopic surveys such as SDSS and the RAdial Velocity Experiment [RAVE; Steinmetz et al. (2006)] exist today, as well as all sky proper motion catalogs such as the PPMXL, we decided to approach the same problem on the basis of kinematics rather than position. Our approach allows the investigation of the production of runaway stars in a completely new class of object – F-M type main sequence dwarfs – which would be difficult to find using the same approach as is used for finding early B-type runaways. Our analysis provides new insight into runaway production, bounds velocity ranges of ejection techniques, and hints at the stellar distribution in the Galactic nucleus.

In Part III, we analyze the accuracy and precisions of a variety of proper motion catalogs. For our study of runaway stars, proper motions are one of the most integral and error prone measurements in our analysis, so it is crucial that we understand their systematics and possible causes of errors. For our study of the dynamics of these objects, we utilize SDSS proper motions; here we propose a series of quality control metrics which can be used to seperate out unreliable proper motion estimates. During the course of this study we notice a systematic offset between the SDSS proper motion catalog and the PPMXL proper motion catalog. Upon further investigation, it is found that the PPMXL proper motion catalog has a systematic pattern for the proper motions of extragalactic objects, such as galaxies and quasars, and a global offset of around two mas $\mathrm{yr}^{-1}$. We fit the proper motions on the sky to a series of spherical harmonics, and produce a methodology for correcting these proper motion offsets.

Each part also includes a small discussion with suggestions for future work to be performed, and a final discussion is situated at the end of the Dissertation. Supplemental information is provided in the Appendix.

# Part I

# Blue Horizontal Branch Stars and the Galactic Halo

*"The Caterpillar and Alice looked at each other for some time in silence: at last the Caterpillar took the hookah out of its mouth, and addressed her in a languid, sleepy voice."*

- Lewis Carroll, *Alice in Wonderland*

# Chapter 2

# Introduction to Part I

Here we plan to study the baryonic stucture of the Milky Way halo by isolating samples of blue horizontal branch stars and looking at them in three dimensional space. We wish to use photometric information only and to isolate a sample of these objects from the Pan-STARRS survey and look at the spatial distribution of these candidates.

In the Introduction, we described some commonly used methods to identify BHBs by virtue of their colors and their spectra. We also mentioned some of the aspects of the upcoming Pan-STARRS mission, most notably: 1) the Pan-STARRS footprint is about twice as big as that of the SDSS and 2) Pan-STARRS lacks the $u_{SDSS}$ photometric filter that previous studies have relied on to photometrically identify BHBs.

With this in mind, we create a color space cut to select out BHB stars from the primary contaminants [QSOs, MSA stars, white dwarfs] based on surface gravity measurements, but rather than exploiting $u_{SDSS}$ band separation, we explore the usefulness of the $z_{SDSS}$ band. With an end-goal of structure mapping and halo studies in mind, we aim primarily for a high purity selection at the cost of completeness. We attempt to achieve accuracies similar to those quoted by Sirko et al. (2004) and Bell et al. (2010) [$< 30\%$ contamination], however, we also expect a lowered sample completeness because of the poorer gravitational separation in this color space. We then wish to use this color cut to select a sample of BHB stars and use them to map out Galactic substructure.

In Chapter 3 we will only work with SDSS data, and it serves mostly as a 'proof of concept.' In that Chapter, we will describe a series of tests for estimating the purity and completeness of the BHB sample collected [Sections 3.1 and 3.2], investigate the technique's viability for structural studies in Section 3.3 and discuss why the technique works in Section 3.4. In Chapter 4 we will apply the technique to actual Pan-STARRS data [with a small digression to recreate the technique using actual Pan-STARRS filters in Section 4.1] and hunt for substructure in the BHB populations of the Milky Way [in Sections 4.2 and 4.3].

We then have a small section on future work and improvements that may be made to our current work.

# Chapter 3

# Identifying Blue Horizontal Branch Stars via the SDSS $z$ Filter

## 3.1 Color Cut

To investigate the separation of various blue objects in the $(i-z)_{SDSS,0}$ color space suggested by Lenz et al. (1998), we select spectra from SDSS DR8 (Aihara et al., 2011). DR8 extends the SDSS footprint to now cover a full third of the celestial sphere and increases the total number of spectra to over 1.8 million[1].

We selected spectroscopic data from the entire SDSS footprint, only clean [not near saturated pixels] objects evaluated as point sources were selected. We used only primary measurements [in the case of multiply observed objects, the highest signal to noise reading is flagged as the primary one]. To make our study consistent with those of Sirko et al. (2004) and Bell et al. (2010) we select only stars with $g_{SDSS} < 18$.

In Figure 3.1, we plot the adopted log(g) value as calculated by the SSPP against $(g-r)_{PS,0}$ [note that while we use Pan-STARRS photometry in this image, it would look identical in SDSS colors]. We note that in the blue color space of -0.3 $< (g-r)_{PS,0} <$ 0.0 there is excellent differentiation of the lower gravity BHB stars, residing in the range of 3.0 $<$ log(g) $<$ 3.75, and the higher gravity MSA stars [3.75 $<$ log(g) $<$ 5.0]. These color and gravity ranges form the basis for our identification of these two types of star in this Chapter.

Some contaminants have no SSPP atmospheric parameters, so we cannot identify them based on their log(g) estimates: the two principal examples are white dwarf stars and quasars. White dwarf stars raise critical flags in the SSPP because of the width of their Balmer lines [$D_{0.2} > 35.0$ Å] and quasars raise critical flags due to their strong emission lines (Lee et al., 2008). To identify these contaminants, we rely on the ELODIE template matches [the ELODIE archive is a set of high resolution spectroscopic readings collected using the ELODIE spectrograph, which has been operating on the Observatoire de Haute-Provence 1.93 m telescope since 1993; Moultaka et al. 2004] as output by the SSPP. The remaining contaminants are binned together– they mostly consist of A and F stars for which the SSPP gravity reading was either inconclusive or outside the bounds of the prior mentioned BHB and MSA star bins.

[0]The work presented in this Chapter was published in Vickers et al. (2012).

[1]http://www.sdss3.org/dr8/

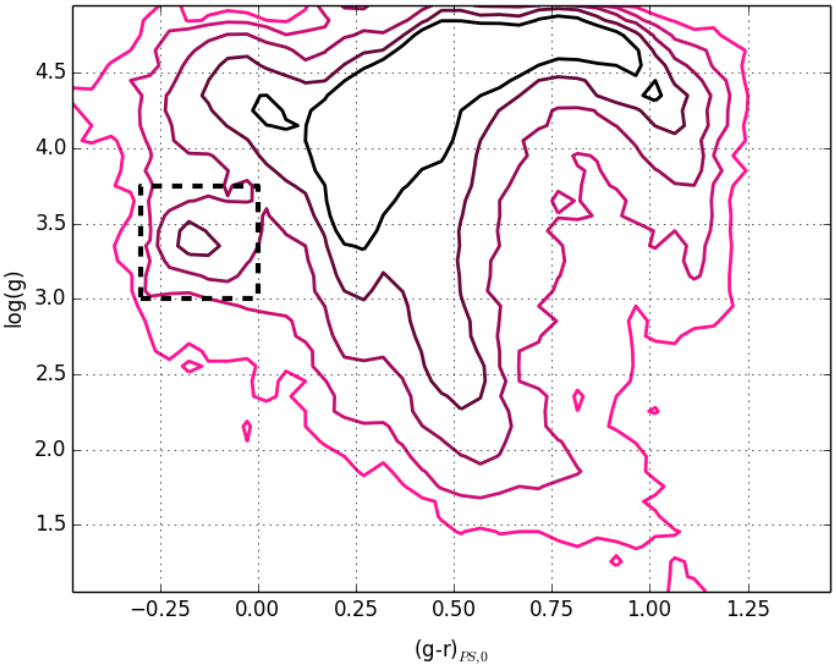


FIGURE 3.1: Dereddened $(g-r)_{PS,0}$ color versus log(g) as calculated by the SSPP pipeline for all spectroscopic sources with valid log(g) measurements. In the A-star colors [ranging from about $-0.3 < (g-r)_{PS,0} < 0.0$] we see two distinct stellar species: the lower surface gravity blue horizontal branch stars and the high surface gravity MSA stars. It is important to note that white dwarfs are largely absent in this diagram [as are quasars] since the SSPP adopted log(g) algorithm fails for these objects. Lee et al. (2008) estimate the average uncertainty in the log(g) measurement from the SSPP to be 0.29 dex. The dashed box roughly outlines the area inhabited by BHB stars.

Using this data set we look to construct a photometric color cut in $(g-r)_{SDSS,0}$ [a temperature indicator] vs $(i-z)_{SDSS,0}$ [a surface gravity indicator] color space [see Figure 3.2]. To do this we use a k-nearest-neighbors classification algorithm. This algorithm classifies unknown objects based on their proximity to known objects. We compare a uniform grid in $(g-r)_{SDSS,0}$ vs $(i-z)_{SDSS,0}$ color space [the grid consisting of 101x101 nodes over the color space -0.3 $< (g-r)_{SDSS,0} <$ 0.0 and -0.25 $< (i-z)_{SDSS,0} <$ 0.05] to the spectroscopic data– grid nodes with 50% or more of their 5 nearest neighbors having been classified as BHB stars were said to reside in BHB color space. We then drew a rough selection box around this BHB color space defined by the points: $[(g-r)_{SDSS,0},(i-z)_{SDSS,0}]$ = [-0.30,-0.18], [-0.05,-0.06], [-0.05,-0.02], [-0.30,-0.02].

In Figure 3.2 we plot these 5 datasets: high gravity MSA stars, low gravity BHB stars, spectroscopically identified white dwarfs, spectroscopically identified quasars and inconclusive points. The lower panel of the plot is a $(g-r)_{SDSS,0}$ vs $(i-z)_{SDSS,0}$ color-color plot: BHB stars are plotted with diamonds while contaminants are plotted with points. Note that only 1 in 5 data-points are shown in the lower panel of the plot to avoid obscuration. However, the upper histograms shows all of the objects which are inside the selection box as a function of color. It is apparent that this separation culls white dwarfs with acceptable efficiency. Note that type DC white dwarfs were neglected from this analysis due to a lack of a SSPP "DC white dwarf" classification and their intrinsically low numbers [<4% of all white dwarfs]. Additionally, one could use a proper motion diagram to remove some of the remaining white dwarfs and some of the closer MSA stars.

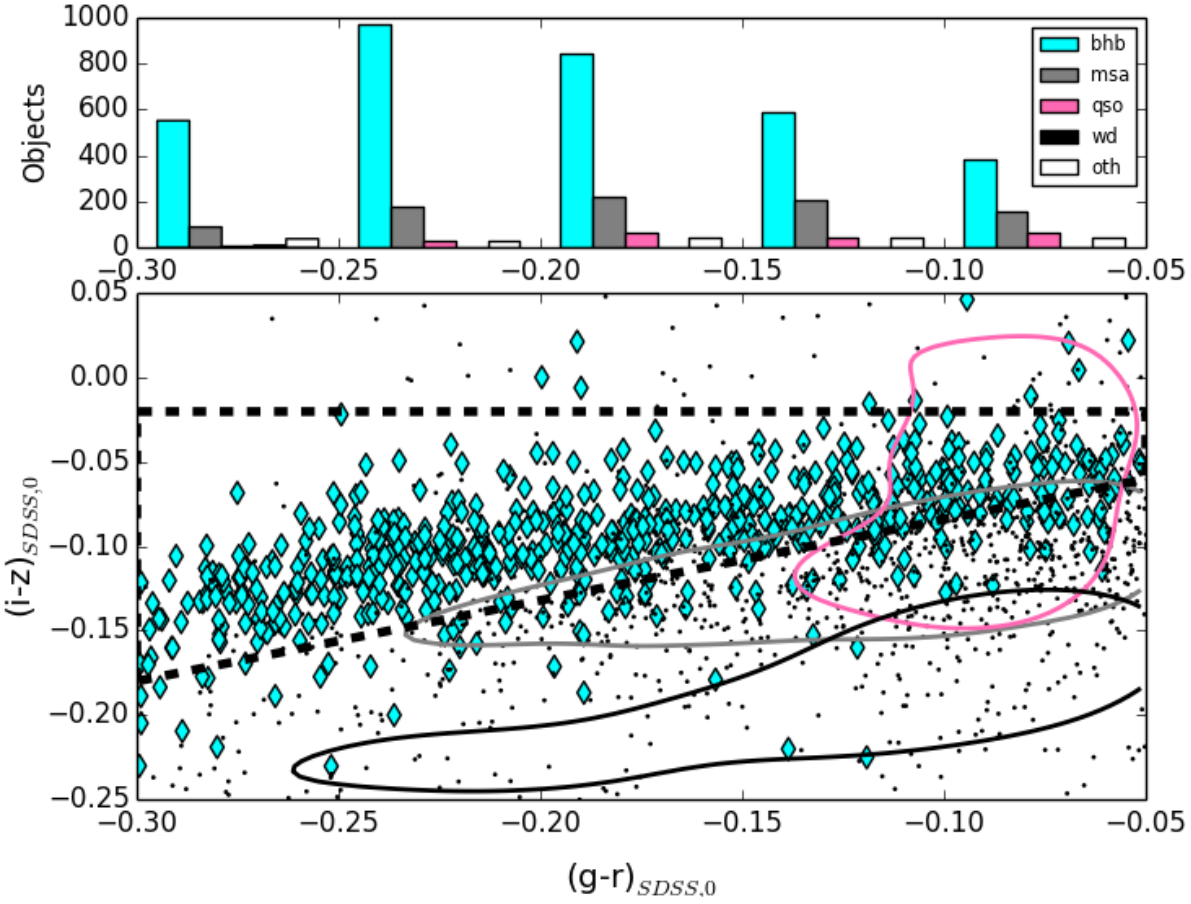


FIGURE 3.2: The lower panel of this plot shows the distribution of objects in the $(g-r)_{SDSS,0}$ versus $(i-z)_{SDSS,0}$ color space. Plotted with diamonds are the BHB stars [as determined by color and surface gravity] and contaminants to this population are plotted as points– only 1 in 5 points from the entire dataset are plotted to avoid overcrowding. The contour lines show the general locations, in this color box, of quasars [qso, the reddest in $(i-z)_{SDSS,0}$ with a locus of about $(i-z)_{SDSS,0}$ = -0.07], main sequence A stars [msa, having a locus at around $(i-z)_{SDSS,0}$ = -0.12] and white dwarfs [wd, the bluest, residing around $(i-z)_{SDSS,0}$=-0.20]: other contaminants [oth] are mostly A and F stars for which the SSPP failed to assign a gravity or assigned a gravity outside of the selection for either BHB or MSA described in the text. In the upper panel, the number and type of objects in the BHB selection box [the dashed polygon] are histogrammed as a function of $(g-r)_{SDSS,0}$ color – all of the dataset is presented in this frame. We see that hardly any white dwarfs pass this color cut.

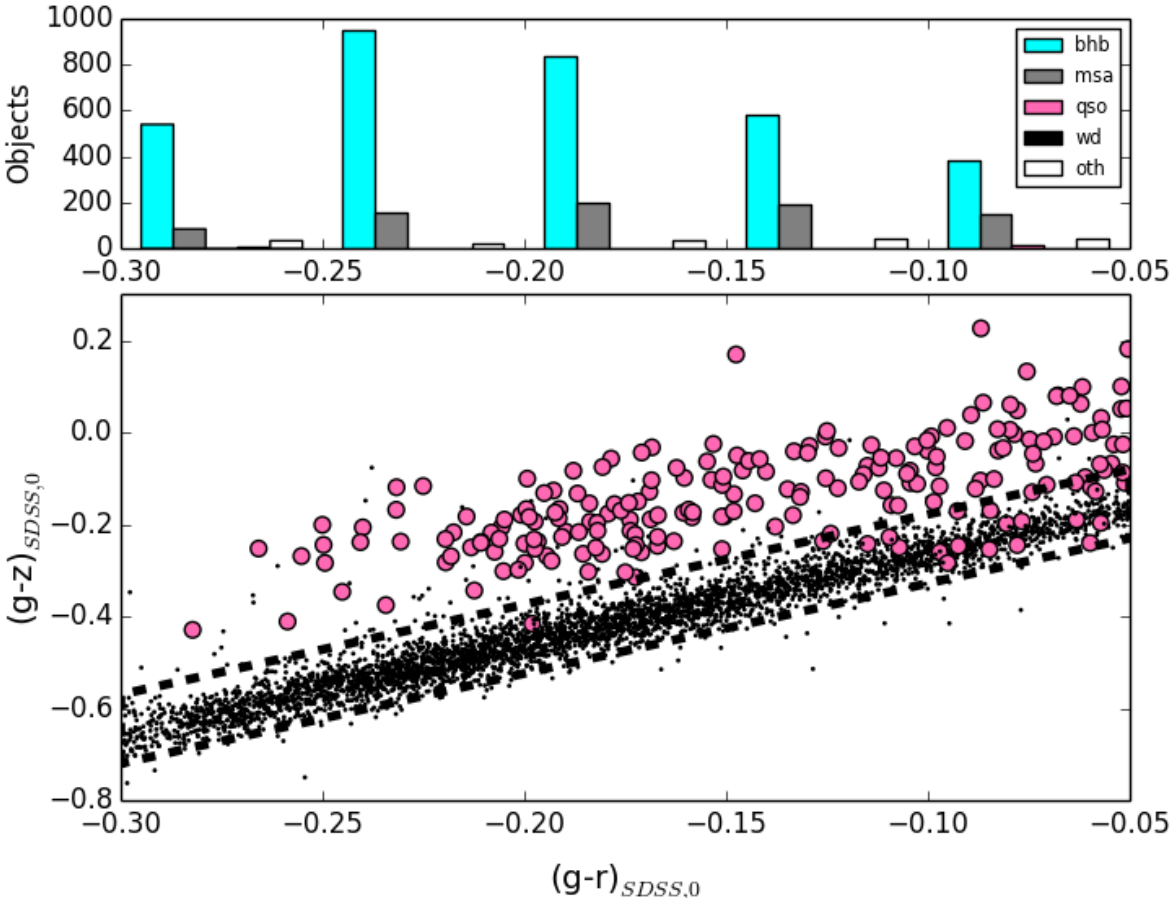


FIGURE 3.3: The lower panel shows the distribution of stellar objects [BHBs, MSAs and white dwarfs; plotted as dots] in $(g-r)_{SDSS,0}$ vs $(g-z)_{SDSS,0}$ color space as compared to that of quasars [plotted as circles]. Only data which pass the color-color cut shown in Figure 3.2 are presented here. The upper panel histograms the number of objects in the BHB selection after this second color-color cut as a function of $(g-r)_{SDSS,0}$ color. Comparison to Figure 3.2 shows that this second color cut is instrumental in removing quasars from the selection sample.

We do not get much more separation from the stellar contaminants in other color spaces. However, we can more efficiently select out quasar contaminants in the $(g-r)_{SDSS,0}$ vs $(g-z)_{SDSS,0}$ color space. We use $(g-z)_{SDSS,0}$ color space due to the spectral profiles of blue stars which are characterized by the tail end of blackbody profiles [tending to lower $(g-z)_{SDSS,0}$ values] and quasars which are more uniform emitters [tending to higher $(g-z)_{SDSS,0}$ values – especially in the case of high redshifts]. In Figure 3.3 we present this additional color cut. This cut is defined by the points: $[(g-r)_{SDSS,0},(g-z)_{SDSS,0})$ = [-0.3,-0.72], [-0.3,-0.57], [-0.05,-0.08], [-0.05,-0.23]. We plot only the data which pass the cut shown in Figure 3.2. Quasars are plotted as circles and stellar sources are plotted as dots to accentuate the separation. Again histogrammed above are the objects passing the color cut. As expected, we see very little change in the stellar contaminants, but quasar contamination drops significantly.

As a test of accuracy, we consider the number of stars falling within the color cut which are not BHB stars. Out of ∼4300 spectra which pass this cut, we find ∼77% of them to be BHB stars; this represents a sample of ∼74% of the stars originally identified as BHB stars. For comparison, we run a similar test

| Cluster Name | $\alpha$ | $\delta$ | $R_\odot$ (kpc) | E(B−V) | $R_{tidal}$ (') | $g$ box |
|---|---|---|---|---|---|---|
| NGC 4147 | 12 10 06.30 | +18 32 33.5 | 19.3 | 0.02 | 6.08 | 16.5-17.5 |
| NGC 5024 | 13 12 55.25 | +18 10 05.4 | 17.9 | 0.02 | 18.36 | 16.25-17.25 |
| NGC 5053 | 13 16 27.09 | +17 42 00.9 | 17.4 | 0.01 | 11.43 | 16-17 |
| NGC 5272 | 13 42 11.62 | +28 22 38.2 | 10.2 | 0.01 | 28.72 | 15-16 |
| NGC 5466 | 14 05 27.29 | +28 32 04.0 | 16.0 | 0.00 | 15.68 | 16-17 |
| NGC 5904 | 15 18 33.22 | +02 04 51.7 | 7.5 | 0.03 | 23.63 | 14.5-15.5 |
| NGC 6205 | 16 41 41.24 | +36 27 35.5 | 7.1 | 0.02 | 21.01 | 14.5-15.5 |
| NGC 6341 | 17 17 07.39 | +43 08 09.4 | 8.3 | 0.02 | 12.44 | 14.6-15.6 |
| NGC 7078 | 21 29 58.33 | +12 10 01.2 | 10.4 | 0.10 | 27.30 | 15-16 |
| NGC 7089 | 21 33 27.02 | -00 49 23.7 | 11.5 | 0.06 | 12.45 | 15.3-16.3 |

TABLE 3.1: General properties of the globular clusters used in our SDSS completeness test. All information is taken from the Harris (1996) Catalog, 2010 revision, excepting the $g$ selection box. The $g$ selection box extends from $g - r$ = -0.3 to 0.0 in all cases.

on the same data using the color cut suggested by Bell et al. (2010) which is similar to the "stringent" color cut employed by Sirko et al. (2004):

$$0.98 < (u-g)_{SDSS,0} < 1.28, \tag{3.1a}$$

$$-0.2 < (g-r)_{SDSS,0} < -0.06, \tag{3.1b}$$

$$\frac{(u-g)_{SDSS,0} - 0.98^2}{0.215} + \frac{(g-r)_{SDSS,0} + 0.06^2}{0.17} > 1. \tag{3.1c}$$

Using this refined $u_{SDSS}$ band dependent test, we similarly select a sample that is ∼74% pure and ∼72% complete. This test is biased by the SDSS spectroscopic selection algorithms, and so is neither a strict test of purity nor completeness.

## 3.2 Globular Cluster Test

We use a completeness test similar to the one employed by Bell et al. (2010). Using Jordi & Grebel (2010) as a reference, we select 10 globular clusters from the SDSS footprint with pronounced BHBs. By running the constituent stars through the photometric cut described in the prior section, we may get a second measure of how effective the algorithm is at extracting BHB stars. The clusters chosen and pertinent information is tabulated in Table 3.1.

Since the SDSS *photoObjAll* pipeline fails for crowded fields, the cores of dense objects, such as globular clusters, are often omitted from the general photometric data. For accurate and complete cluster photometry we turn to the SDSS "value added" catalogs[2]– in particular we use the "*ugriz* DAOPHOT photometry of SDSS+SEGUE Globular and Open Clusters" catalog produced by An et al. (2008).

Since the An et al. (2008) value added catalog was created with SDSS Data Release Seven [DR7; Abazajian et al. 2009] imaging and pipelines, we use DR7 photometric data for this cluster analysis.

[2]http://www.sdss.org/DR7/products/value_added/index.html

Data are selected from DR7 within one third of the tidal radii of the relevant clusters [Harris 1996 catalog, 2010 revision] and then matched to the DAOPHOT photometry. In the cases of duplicate points, DAOPHOT photometry is preferred. The stellar magnitudes and colors are extinction corrected and dereddened according to the Harris Catalog E(B-V) values.

By examining the color-magnitude diagrams of the clusters, we visually select 1-magnitude wide boxes encompassing the main portion of the blue horizontal branch in the $-0.3 < (g-r)_{SDSS,0} < 0.0$ regime. This selection box contains the stars we will consider "true" BHBs. All stars outside of these boxes will be considered "false." It is apparent from clusters such as NGC 7078 and NGC 5272 that these 1-magnitude boxes suffer RR Lyrae contamination on the red end and in the clusters NGC 6205 and NGC 6341 we see hot sub-dwarf contamination on the blue end. However, in general, these boxes should consist mainly of BHB stars. The ranges for these magnitude boxes are also given in Table 3.1 and the cluster color-magnitude diagrams with the selection boxes superimposed are shown in Figure 3.4.

From these clusters, we select only stars passing the color-cut selection described in Section 3.1. We do not consider this test to be a test of accuracy due to the selective enrichment of BHB stars in these cluster-fields – however, we do consider this to be a good test of completeness. Stars passing our $z_{SDSS}$ based color cut constitute a sample that is ∼95% pure and ∼51% complete. As in Section 3.1 2, we again cut the data using the $u_{SDSS}$ based "stringent" color selection and find a sample that is ∼92% pure and ∼57% complete [see Table 3.2].

We consider the statistics on the spectroscopic data to be a better indicator of accuracy and the globular cluster statistics to be a better indicator of completeness. Thus, when considering this test in conjunction with the spectroscopic statistics, we consider the $u_{SDSS}$ based cut to be ∼74% pure and ∼57% complete which is in agreement with the values quoted by Bell et al. (2010) and Sirko et al. (2004). The $z_{SDSS}$ based cut similarly has a ∼77% purity and a ∼51% completeness.

| Cluster Name | [Fe/H] | Total BHBs | Purity$_{griz}$ | Completeness$_{griz}$ | Purity$_{ugr}$ | Completeness$_{ugr}$ |
|---|---|---|---|---|---|---|
| NGC 5904 | -1.29 | 184 | 0.96 | 0.38 | 0.94 | 0.53 |
| NGC 5272 | -1.5 | 233 | 0.94 | 0.40 | 0.89 | 0.54 |
| NGC 6205 | -1.53 | 251 | 0.94 | 0.47 | 0.84 | 0.54 |
| NGC 7089 | -1.65 | 318 | 0.94 | 0.37 | 0.94 | 0.36 |
| NGC 4147 | -1.8 | 60 | 0.96 | 0.45 | 0.94 | 0.48 |
| NGC 5466 | -1.98 | 115 | 1.00 | 0.84 | 0.96 | 0.84 |
| NGC 5024 | -2.1 | 351 | 0.96 | 0.70 | 0.94 | 0.70 |
| NGC 5053 | -2.27 | 28 | 0.92 | 0.82 | 0.96 | 0.79 |
| NGC 6341 | -2.31 | 154 | 0.98 | 0.34 | 0.96 | 0.60 |
| NGC 7078 | -2.37 | 194 | 0.88 | 0.57 | 0.90 | 0.58 |
| Total | | 1888 | 0.95 | 0.51 | 0.92 | 0.57 |

TABLE 3.2: This table shows the accuracy and effectiveness of the two tests in extracting BHB stars from the chosen globular clusters. Metallicities from the Harris (1996) catalog, 2010 revision, are included and the globular clusters are sorted by this property– one can see a slight trend in both tests to more effectively select BHB stars at lower metallicities, especially in the area around -2.0 dex. This is most likely an effect of our color cut being formulated by the color distribution of halo BHB stars spectroscopically observed by the SDSS, which have an average metallicity of -2.0 dex (Xue et al., 2008).

## 3.3 The Celestial Equator

To show the ability of this selection method to probe features of the Milky Way's structure, we examine the celestial equator. This area [$-1.26^\circ < \delta < 1.26^\circ$] has been almost completely imaged in the SDSS, excepting areas too close to the Galactic plane. The portion of this great circle above the Galactic equator is known as stripe 10 [see Stoughton et al. (2002) for stripe naming conventions in the SDSS] and the portion residing in the southern Galactic hemisphere is stripe 82. Stripe 82 has been imaged repeatedly to promote studies of variable objects, such as supernovae (Frieman et al., 2008), RR Lyraes (Sesar et al., 2010) and quasars. Owing to the multiple epoch observations, this area of sky not only is optimal for transient studies, it also goes about two magnitudes deeper than the rest of the survey. As such, this section of the sky has been extensively probed for evidence of substructure [see Newberg et al. 2002 and Sesar et al. 2007 for examples].

We create a sample of candidate BHB stars by selecting all photometrically clean sources identified as point sources [selecting only primary measurements in the case of duplicates] residing in the plane of the celestial equator and pass their dereddened photometric data through the color cut suggested in Section 3.1. We note that, in general, noise in spectra of stars fainter than $g_{SDSS}$=18 throw errors into the parameter determinations [Sirko et al. 2004; exceptions include SEGUE pencil beams which were imaged for various time scales to maximize signal to noise ratios at two main magnitude bins and so may go fainter than the general spectroscopy, see Yanny et al. 2009]– but since the CCD camera can reliably determine colors to much fainter magnitudes (Gunn et al., 1998), photometric separation is still practical. Photometric separation has the parallel benefit of being viable for a much more complete sample of stars when compared to spectroscopic methods.

The results of our photometric selection are plotted in Figure 3.5. Immediately evident are several well documented structures: among these are the Sagittarius stream in both the northern and southern Galactic hemispheres (Yanny et al., 2000), the Virgo overdensity (Vivas et al., 2001) in the north, and the Hercules-Aquila cloud in both the north and the south noted independently by Newberg et al.

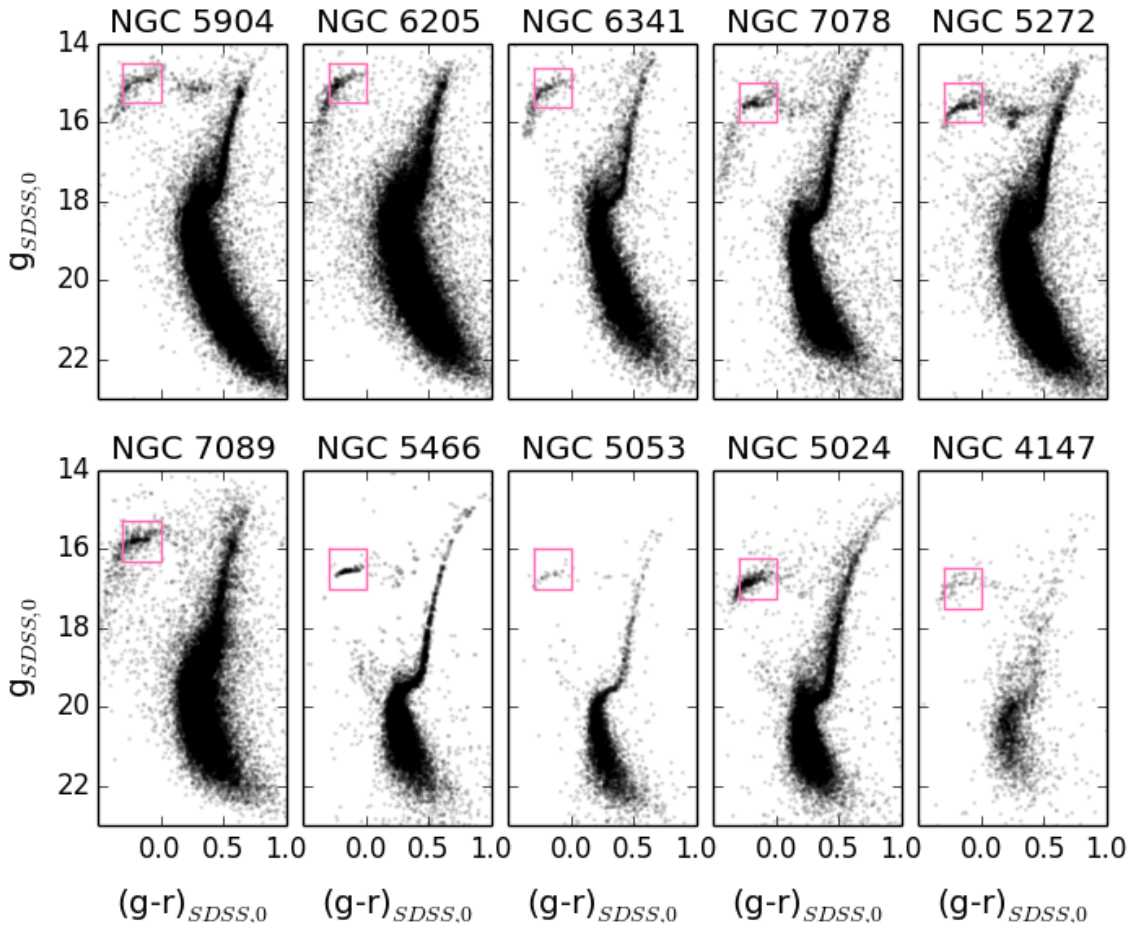


FIGURE 3.4: Color-magnitude diagrams of 10 globular clusters found in the SDSS footprint, arranged by radial distance from the sun [Harris 1996 catalog, 2010 revision values; Table 3.1]. The data are all photometry from the inner one third of the projected tidal radius of the cluster. The drawn boxes indicate the general location [as selected by eye] of the 'true' BHBs used for the completeness test described in Section 3.2. Each box extends 1 magnitude in $g_{SDSS}$ from $(g-r)_{SDSS,0} = -0.3$ to 0.0. Clusters such as NGC 7078 and NGC 5272 show RR Lyrae contamination on the red end of the box and clusters such as NGC 6205 and NGC 6341 show extreme horizontal branch contamination on its blue end.

(2002) and Belokurov et al. (2007), and the anomalous density at $\alpha = 160°$ noted by Newberg et al. (2002).

## 3.4 Spectral Reasoning

We suspect that the $z_{SDSS}$ band shows gravitational separation due to the gravitationally sensitive Paschen features [the Paschen analog to the Balmer jump resides at 8201Å], which lie in the $z_{SDSS}$ band. We anticipate that this separation may be even more effective on the Pan-STARRS telescope which has a much more infrared sensitive CCD than the SDSS imaging camera, and thus a more responsive $z_{SDSS}$ filter (Stubbs et al., 2010). Figure 3.6 depicts spectra of the objects discussed in this chapter [BHB stars, MSA stars, white dwarfs, and quasars] and includes the throughput functions of both the SDSS 2.5 m telescope and the Pan-STARRS 1.8 m telescope.

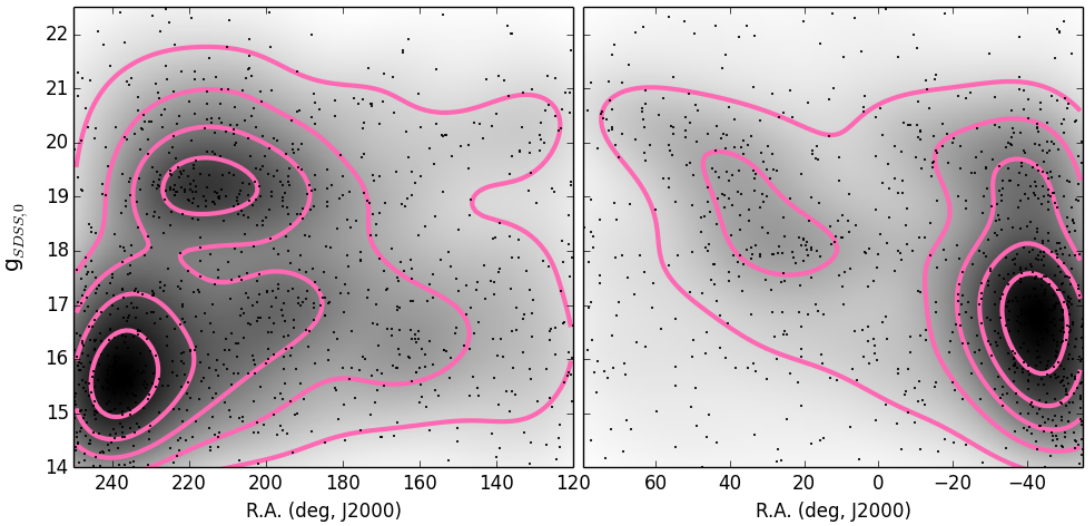


FIGURE 3.5: Left: The northern Galactic hemisphere section of the celestial equator [stripe 10]. Photometric objects passing the color cuts shown in Figures 3.2 and 3.3 are presumed to be BHB stars and are plotted here. The density of the points is shown via a gray-scaled density estimate which is accentuated by the pink contours. We see the Hercules-Aquila cloud at $\alpha \approx 240^\circ$ and $g \approx 16$; from $\alpha \approx 230^\circ$ to $\approx 200^\circ$ the Sagittarius dwarf spheroidal's tidal stream is apparent at $g \approx 19$; the Virgo overdensity can be seen at $\alpha \approx 200^\circ$ and $g \approx 17$, the overdensity at $\alpha \approx 160^\circ$ and $g \approx 16$ is noted in F-turnoff stars by Newberg et al. (2002).
Right:The southern Galactic hemisphere section of the celestial equator [stripe 82]. Once again we see evidence for major known structures such as Sagittarius at $\alpha \approx 30^\circ$ and $g \approx 18$ and the Hercules Aquila cloud at R.A $\approx$ -40° and $g \approx 17$.

To explain the difference in $(i-z)_{SDSS,0}$ colors of BHB stars and MSA stars, we examine high signal-to-noise spectra from the SDSS survey with particular attention paid to the 7000Å-9200Å range. We collect FITS images of all spectra in the SDSS survey which have a signal-to-noise ratio $\geq 50$, are primary science readings, and classified as stars. Similar to Section 3.1, we select stars in the -0.3 $< (g-r)_{SDSS,0} <$ 0.0 color range and define BHB stars as those in the 3.0 $<$ log(g) $<$ 3.75 gravity range; MSA stars are defined as having 3.75 $<$ log(g) $<$ 5.0.

We construct two "super-spectra" by combining all spectra from each population. The spectra were individually shifted in wavelength such that the minimum of their Balmer-$\alpha$ absorption feature fell at 6563Å to account for differing radial velocities. They were then normalized to their flux value at 7500Å. It became apparent that, since our sample consisted of the whole -0.3 $< (g-r)_{SDSS,0} <$ 0.0 color range [which spans from about 7500K to 10000K] a systematic difference in temperature needed to be accounted for [as our BHB sample is centered on this color range, but our MSA sample trends toward cooler, redder colors]. We select BHB stars in the color range -0.15 $< (g-r)_{SDSS,0} <$ -0.10 and MSA stars in the color range -0.17 $< (g-r)_{SDSS,0} <$ -0.12– these color ranges produced composite spectra which had approximately equal continua and Balmer line depths. We then bin the spectra into 2Å wide bins and accept the median values of these bins as the composite value.

Figure 3.7 shows the well known Balmer-$\alpha$ absorption feature for our two super-spectra. We easily discern the differing profile widths and shapes that are the basis for differentiation of these types of stars in spectroscopic studies [e.g. Pier 1983, Clewley et al. 2002; the BHB star features are significantly slimmer than their MSA star analogs]. In the second frame we expand the Paschen features of these two types of stars. It is unsurprising that we see a similar effect in the $z_{SDSS}$ band features– the BHB

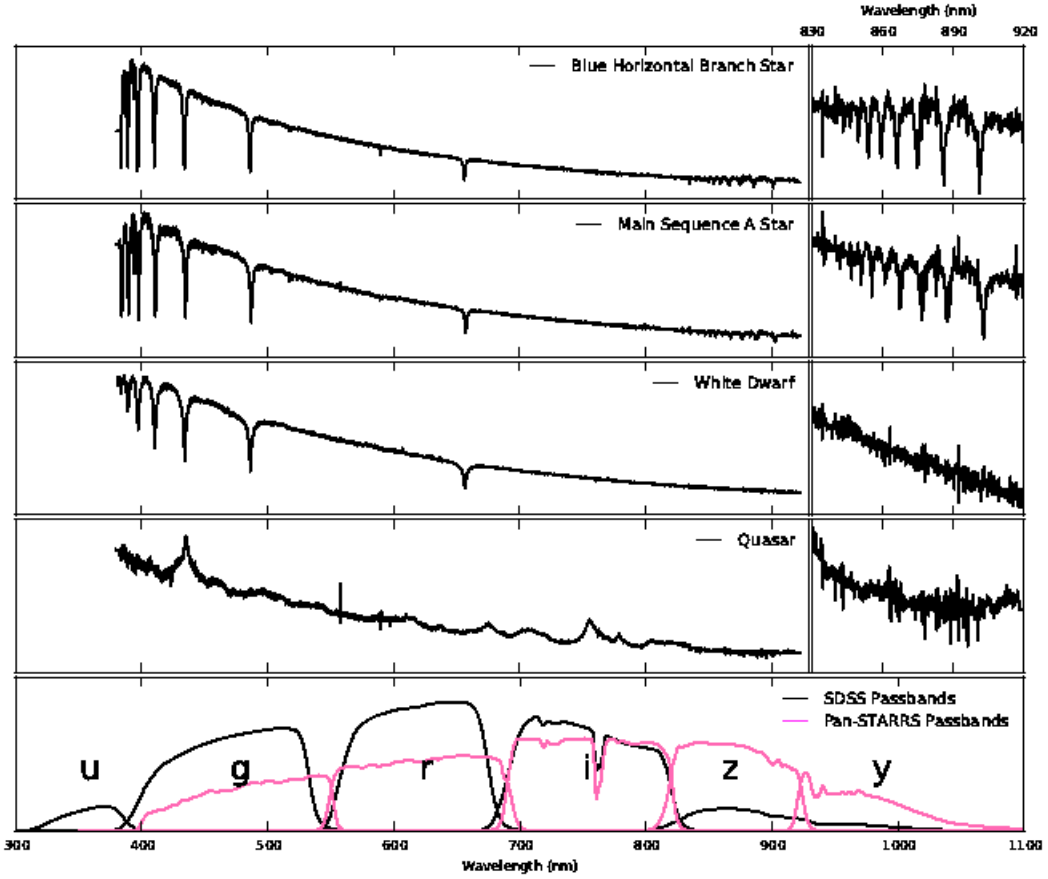


FIGURE 3.6: The top four frames of this image are SDSS spectra of a typical BHB star, MSA star, white dwarf and low redshift quasar, respectively. The bottom frame depicts the SDSS passband functions [$ugriz_{SDSS}$, from left to right] as described by Doi et al. (2010) and the Pan-STARRS passband functions [$grizy_{PS}$, from left to right] provided on the Pan-STARRS website[3]. In the spectra of the BHB and MSA stars, we see the Paschen features in the 830 nm to 920 nm range [which falls in the z-band of both systems; expanded to the right]– these features will cause a difference in $z$ band based colors for BHB and MSA stars since they are susceptible to gravitational pressure broadening.

star features are much narrower. Near a hydrogen absorption series limit, the features will overlap to form a quasi-continuum, thus the more intense Stark pressure broadening of the MSA stars makes their features wider and forces their pseudo-continua lower. This combination of slimmer absorption features and a higher Paschen continuum explains the difference in $z_{SDSS}$ band magnitude for BHB and MSA stars at the same temperature.

An interesting corollary to this result is the possibility of using only the Paschen features to separate BHB and MSA stars spectroscopically. To examine this, we consider only the area of the spectra between 8500Åand 9000Å; we only use this portion of the spectra since fitting to the entire spectra provides especially poor fits in the Paschen region. The continuum is defined to be the portion of the spectra exactly in between any two Paschen minima $\pm$5Å [two standard deviation outliers are discarded]– the continuum is then fit to a tertiatic, which is divided out. The resulting normalized spectra are analyzed

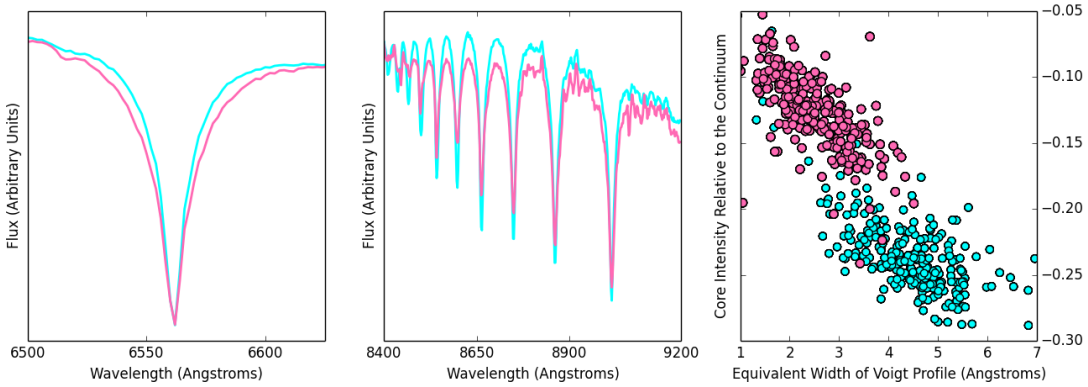


FIGURE 3.7: The left frame shows the Balmer-$\alpha$ line for a composite MSA star [pink] and a composite BHB star [cyan]. Due to Stark pressure broadening, these two absorption line profiles have different line widths and shapes which allows separation of these two species of star based on their differing surface gravities. The middle frame shows the Paschen absorption features in the $z$ band region. These features show a similar behavior with the BHB spectra [pink] having slimmer absorption lines than the MSA star [cyan]. Since the continuum at this point is actually a quasi-continuum formed by the Paschen features flowing into each other, the BHB star appears to have a higher continuum than the MSA star [since broader features would push the effective continuum lower]– this is the effect responsible for the differing $z$ band magnitudes. The rightmost frame depicts the difference in equivalent width versus core intensity for the Paschen feature residing at 8596Å [the Paschen 14 line] for BHB stars [cyan; having $3.0 < \log(g) < 3.75$] and MSA stars [pink; having $3.75 < \log(g) < 5.0$]. This plot was constructed using the high signal to noise [$\geq 50$] spectra which contributed to the combined spectra [described in Section 3.4]. We see a distinct separation between these two species of stars in this parameter space; the pseudo-continuum is higher in the BHB stars which causes the feature to have a larger equivalent width and a higher core intensity.

using an IRAF[4] (Tody, 1986) fitting routine. Included in Figure 8 is a plot of intensity vs the Voigt profile equivalent width of the Paschen line at ∼8596Å [the Paschen 14 line] for the entire high signal to noise dataset. We see good separation of BHB and MSA stars in this plot. Notably, in this region, we see the BHB stars as having larger equivalent widths, which is counterintuitive. This is an effect of the pseudo-continuum shrinking the MSA features artificially owing to their broad and extended wings (Fremat et al., 1996)– an effect corroborated by the correspondingly higher core intensities of the BHB stars.

[4]IRAF is distributed by the National Optical Astronomy Observatories, which are operated by the Association of Universities for Research in Astronomy, Inc., under cooperative agreement with the National Science Foundation.

# Chapter 4

# Blue Horizontal Branch Stars in Pan-STARRS

Having successfully demonstrated the efficacy of using the $z_{SDSS}$ passband to select BHBs in the previous chapter, we now extend that technique to the survey which motivated its development: Pan-STARRS. While the technique is basically the same, a few differences must be taken into account to successfully apply the technique to Pan-STARRS.

The most prominent difference between the two surveys is the photometry. While the Pan-STARRS passbands are designed to be similar to the SDSS passbands, the filter curves do differ in their throughput functions; see Figure 4.1. This is a combined effect of the filter production and also improved techniques in instrument production – for example the infrared cutoff on the Pan-STARRS CCD is much redder than that of the SDSS thanks to improved silicon manufacturing techniques.

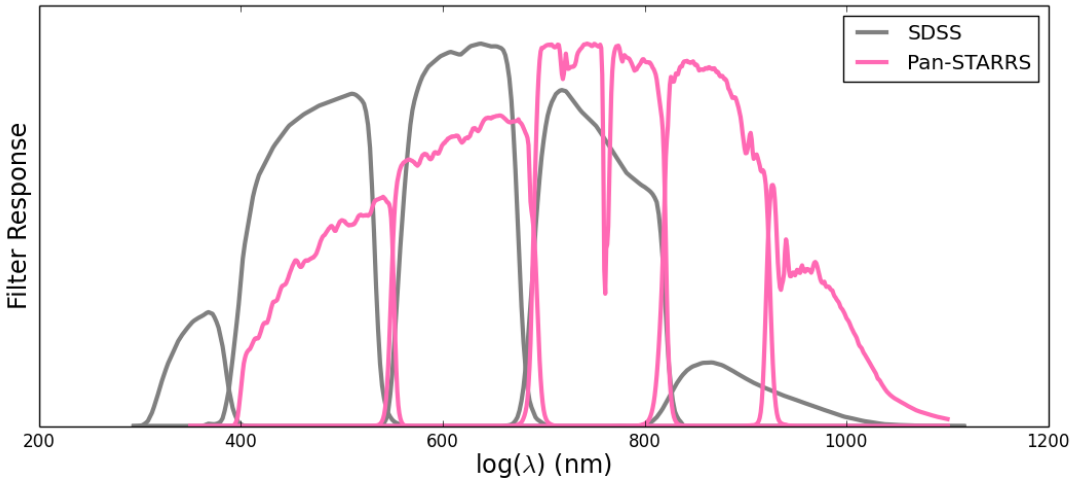


FIGURE 4.1: As seen here, the filter responses for the Pan-STARRS and SDSS instruments are quite different, especially in the infrared. The $z_{SDSS}$ band has no infrared cut and it's response is instead silicon limited. As we have improved manufacturing techniques, the $z_{PS}$ filter has a cutoff and the y filter instead is the silicon limited one. Note also that the $z_{PS}$ is much more responsive in relation to the whole system than the $z_{SDSS}$ filter. This will affect the color selection boxes that we use to isolate BHB stars.

To account for this, we must recreate the color cuts described in Section 3.1 using actual Pan-STARRS photometry. While conversion coefficients between the two systems exist, we feel that using actual data is the proper way to deal with the problem and are lucky enough to have access to said data.

In Section 4.1 we describe the selection criteria for the Pan-STARRS data and essentially repeat Section 3.1 and Section 3.2 using native Pan-STARRS photometry. In Section 4.2 we describe an automated technique for searching for Galactic substructure; in Section 4.3 we report our Galactic substructure detections.

## 4.1 Adapting the Selection to Pan-STARRS

As mentioned, while the SDSS and Pan-STARRS instruments have similar filters, there is enough of a difference [especially in the $z$ band] to warrant redoing the color cut derived in Section 3.1 using actual Pan-STARRS photometry.

The first step is to select point source objects. When using SDSS data from the SSPP pipeline, it is easy to select point sources based on the flag "PSF = 1;" however the Pan-STARRS Large Survey Database [LSD] does not have a point source flag. Instead a variety of magnitude measurements are provided and the researcher must use their own discretion to determine what is and isn't a point source.

The LSD database provides, among other things: average, median and aperture magnitudes. The average and median magnitudes are point spread function magnitudes and are so named owing to the fact that the Pan-STARRS sources have multiple measurements in each band [$\sim$6 measurements per band, on average]. For our study we opt to use the median magnitudes, as low number averages could be significantly skewed by one poor measurement.

By comparing the PSF magnitudes with the aperture magnitudes, one can see a separation of point sources and extended sources [see Figure 4.2] with extended sources tending to be brighter in the aperture magnitudes. At fainter observational magnitudes – for example, past $21^{st}$ magnitude in Figure 4.2 – photometric errors cause this separation to become less precise and more confused. For this work we use data which obeys:

$$|g_{PS,median} - g_{PS,aperture}| < 0.1; 13 < g_{PS,median} < 20. \tag{4.1}$$

To derive the color cuts, we follow the same methodology as before. Namely we collect Pan-STARRS photometry for the entire SDSS spectroscopic catalog and the entire globular cluster catalog of Harris (1996) [2010 revision].

We begin with the SSPP spectroscopy and Pan-STARRS photometry. We define any object in the data set which has a surface gravity of $0.0 < \log(g) < 3.75$ and is in our blue color range of $(g\text{-}r)_{PS,0} < 0.0$ as a true BHB. The lower limit on the surface gravity is to seed out pipeline failures; when the SSPP pipeline fails to assign a surface gravity to an object, the value -9999 is assigned.

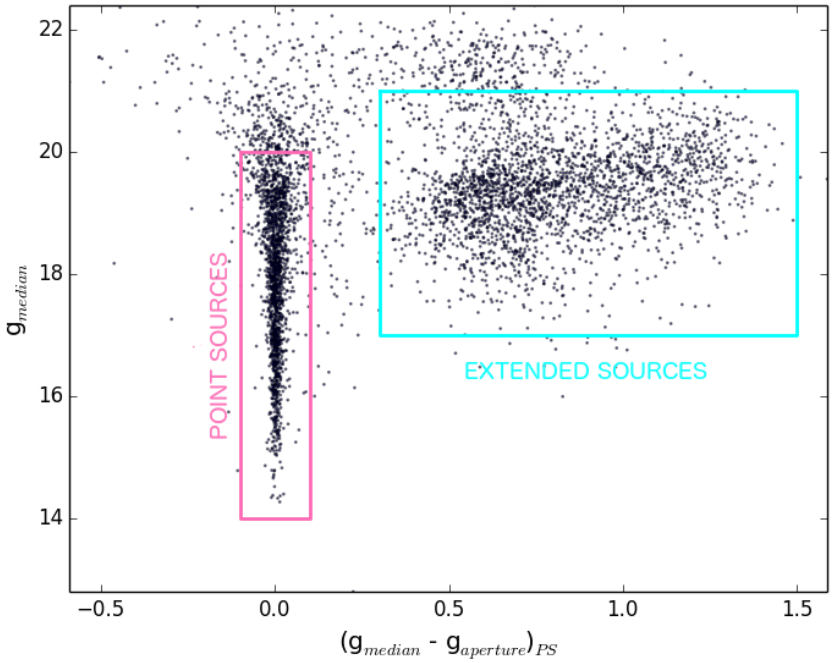


FIGURE 4.2: The difference in point spread function magnitude and aperture magnitude for a sample of objects in Pan-STARRS vs the point spread function magnitude. The current Pan-STARRS data product does not have a flag to indicate point source versus extended source photometry as in the SDSS *photoObjAll* catalog. In the plot there are two distinct groups of objects: point source objects such as stars and quasars, and extended objects such as galaxies and nebula. For our study with BHBs we use only objects in the pink selection box.

Investigating these data, we come up with the color selection shown in Figure 4.3 and defined by the relations:

$$(g-r)_{PS,0} < -0.03, \tag{4.2a}$$
$$(g-r)_{PS,0} > -0.3, \tag{4.2b}$$
$$(i-z)_{PS,0} < -0.03, \tag{4.2c}$$
$$(i-z)_{PS,0} > 0.50((g-r)_{PS,0} + 0.3) - 0.20, \tag{4.2d}$$
$$(g-z)_{PS,0} > 1.95((g-r)_{PS,0} + 0.05) - 0.25, \tag{4.2e}$$
$$(g-z)_{PS,0} < 1.95((g-r)_{PS,0} + 0.05) - 0.15. \tag{4.2f}$$

According the SSPP data, this produces a color cut which, below $18^{th}$ magnitude in $g_{PS}$ is about 75.2% pure. We say below $18^{th}$ magnitude because, past $18^{th}$ magnitude, the calculated purity drops drastically. However, in our substructure search in Section 4.2 we use data extending to $20^{th}$ magnitude. The reason for this is simple: we feel that the purity drop is artificial and caused by SSPP pipeline failures causing BHB stars to be classified as non BHB stars due to log(g) measurement errors at the faint end of the spectroscopic data, while the photometric data looks precise down to about $20^{th}$ magnitude. See Figures 4.2 and 4.4 for example.

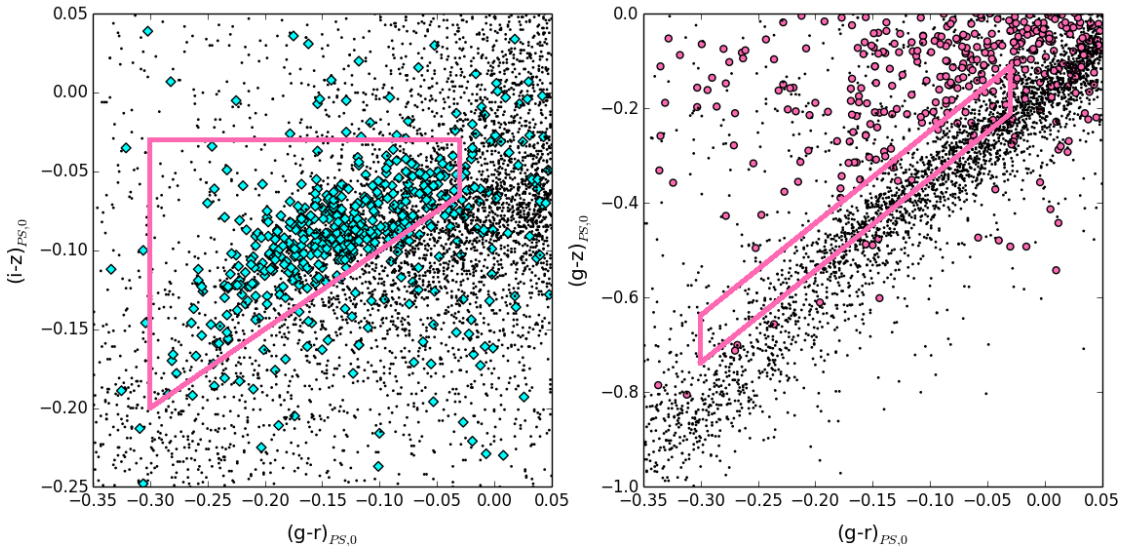


FIGURE 4.3: Our new color cuts for BHB stars using Pan-STARRS photometry.
*Left:* Similar to Figure 3.2. In cyan are stars which have surface gravities log(g) < 3.75, we consider these to be true BHB stars. The points are all other objects which intrude into our color box.
*Right:* Similar to Figure 3.3. In pink are spectroscopically identified quasars. This $(g-z)_{PS,0}$ cut is primarily to separate out quasars in the SDSS color cut, but in the more sensitive $z_{PS}$ filter, these is also an amount of separation between BHB stars and MSA stars on the stellar locus, for that reason we do not select the entire locus, but rather a slice of it.
These cuts are described in the text and select a sample of BHB candidates which is about 75.2% pure and 56.5% complete.

We next attempt to calculate the completeness of the color selection described above by applying it to various globular clusters in the Pan-STARRS footprint. We collect photometry for stars within half the tidal radius of their host cluster and define BHB stars as those lying in the box: -0.3 < $(g\text{-}r)_{PS,0}$ < 0.0 and 0.0 < $M_{PS,r}$ < 1.0; where $M_{PS,r}$ is determined by assuming the distances presented in Harris (1996), 2010 revision, and converting apparent magnitude to absolute magnitude in the usual fashion:

$$\mathrm{D\ (kpc)} = 0.01 \times 10^{\frac{m-M}{5}}. \tag{4.3}$$

For these 13 clusters, we apply our color cut to the members and calculate that our selection box captures roughly 56.5% of the BHB population. This purity and completeness are in agreement with what is expected from Section 3.2.

Finally, rather than assuming a constant magnitude for the entire BHB, we wish to assign slightly more precise absolute magnitudes by investigating the morphology of the horizontal branch as a function of color as was done in Deason et al. (2011). In the color range we currently investigate, this is not much of a correction, but when including bluer portions and the extreme horizontal branch, this more proper approach is critical. In Figure 4.5 we fit the horizontal branch absolute $r$ magnitude to a tertiatic as a function of $(g\text{-}i)_{PS,0}$ color [in the range -0.5 < $(g-r)_{PS,0}$ < 0.0 and 0 < $M_{r,PS}$ < 2.0] and obtain the following relation:

$$M_r = -10.13(g-i)^3_{PS,0} - 4.33(g-i)^2_{PS,0} - 1.31(g-i)_{PS,0} + 0.38. \tag{4.4}$$

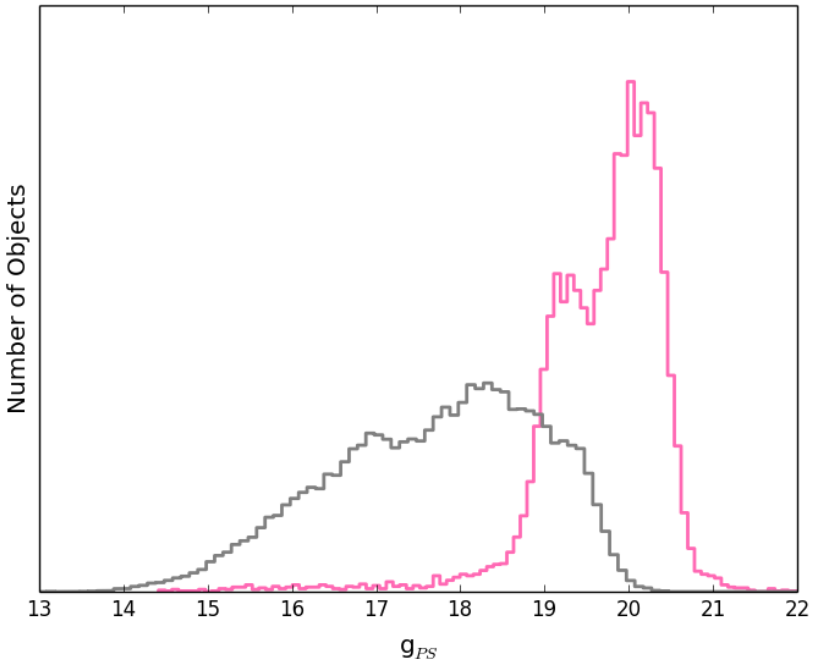


FIGURE 4.4: Histogrammed as a function of observed magnitude are the number of A star objects from the SSPP which have SSPP gravity determinations [grey] and for which the SSPP gravity determination errors out [pink]. In our calculations of the purity of the color cut in Figure 4.3, we consider only objects below $18^{th}$ magnitude, and yet in our substructure search in Section 4.2 we use objects out to $20^{th}$ magnitude. This is because the purity of the color cut artificially drops past $18^{th}$ magnitude since the surface gravity reading is part of our definition for a true BHB star and the pipeline just fails for faint, low signal to noise objects. Color on the other hand, should be accurate at fainter magnitudes than the SSPP is.

The astute reader may wonder why the box within which we fit the horizontal branch is so much larger than the box within which we are selecting BHB stars. The reason is that in Section 4.3 we will alter the color cut presented here to go much bluer in color space and to increase the completeness of the color cut at the expense of purity. This magnitude fit is not poorly affected on the red end by the inclusion of the bluer data.

## 4.2 A Structured Search Technique for Pan-STARRS

Rather than subjectively searching the sky for substructure and overdensities, we wish to create an objective, automated search algorithm which will identify such features. This is a difficult undertaking for a few reasons. First of all, the Pan-STARRS footprint is highly non-uniform; besides the instrumental cutoff at a $\delta$ of -30°, several observational holes exist in the data [most notably in the area of sky which is observable in winter due to bad winter weather]. Secondly, the data are of intermittent quality depending on the number of pointings which cover any given area; the number of photometric observations in any given band for our BHB candidates ranges from one to thirty, with no well defined distribution. See Figure 4.6 for the differential coverage of the Pan-STARRS data.

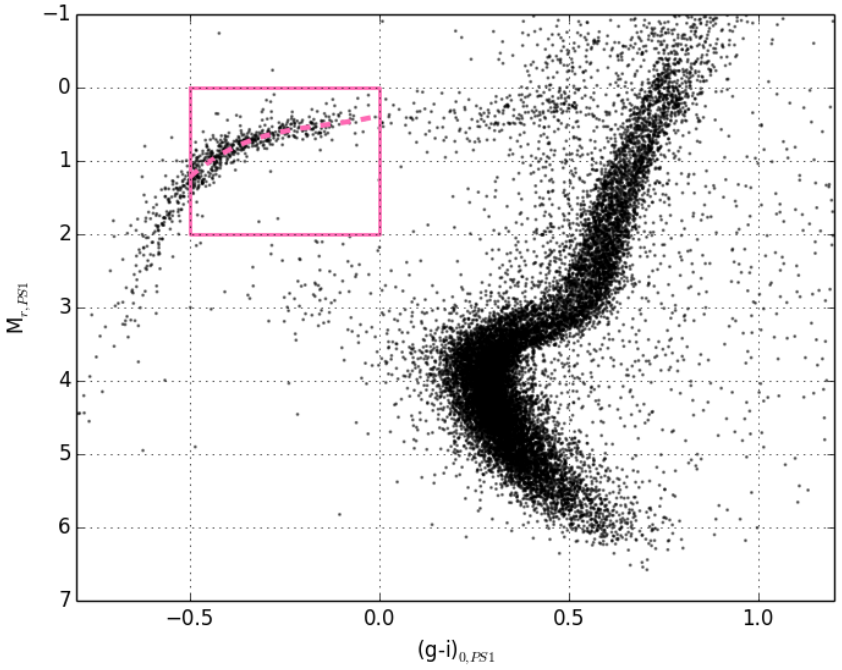


FIGURE 4.5: Distance to BHB stars is usually estimated by assuming a constant magnitude, however this is a bit simplistic, especially when expanding blueward to use the extreme horizontal branch [as we will do later]. Here we show a color-magnitude diagram for all the globular clusters in the Pan-STARRS footprint which have been put on an absolute magnitude scale by assuming the distances presented in the catalog of Harris (1996) [2010 edition]. The pink selection box shows the objects that we assume to be BHB stars for this fit. The dashed line is a fit tertiatic and is the basis for our determination of the distances to individual BHBs in the study as a function of both their color and apparent magnitude.

While we have no real solution to the second problem, the first problem may be circumvented by using a ratio based search: considering the relative number of objects at a certain distance in a pencil beam and then comparing that with the relative number of objects at a certain distance in a suitable control field should reveal overdensities even if a given pencil beam is only partially observed.

Our search methodology thus is as follows:

- Loop through all $l$, $b$, and r values on the celestial sphere with a radius of 100 kpc in steps of 2° and 2 kpc.
- At each loop position the on-field pencil beam is a 10° by 10° section of sky, and the observed cube is a section of that pencil beam 10 kpc thick.
- The comparison disk is the 10° wide strip of sky at the same galactic latitude as the on-field pencil beam, the comparison ring is the subset of this disk at the same radius as the observed cube. Note that all objects within 10° of the Sagittarius tidal debris [$|B_\odot| > 10$, with $B_\odot$ described by Majewski et al. (2003)] are removed from the comparison disk and ring.
- The point's concentration is the number of BHBs in the observed cube divided by the number of BHBs in the on-field pencil beam. The normal concentration of objects at that latitude is the

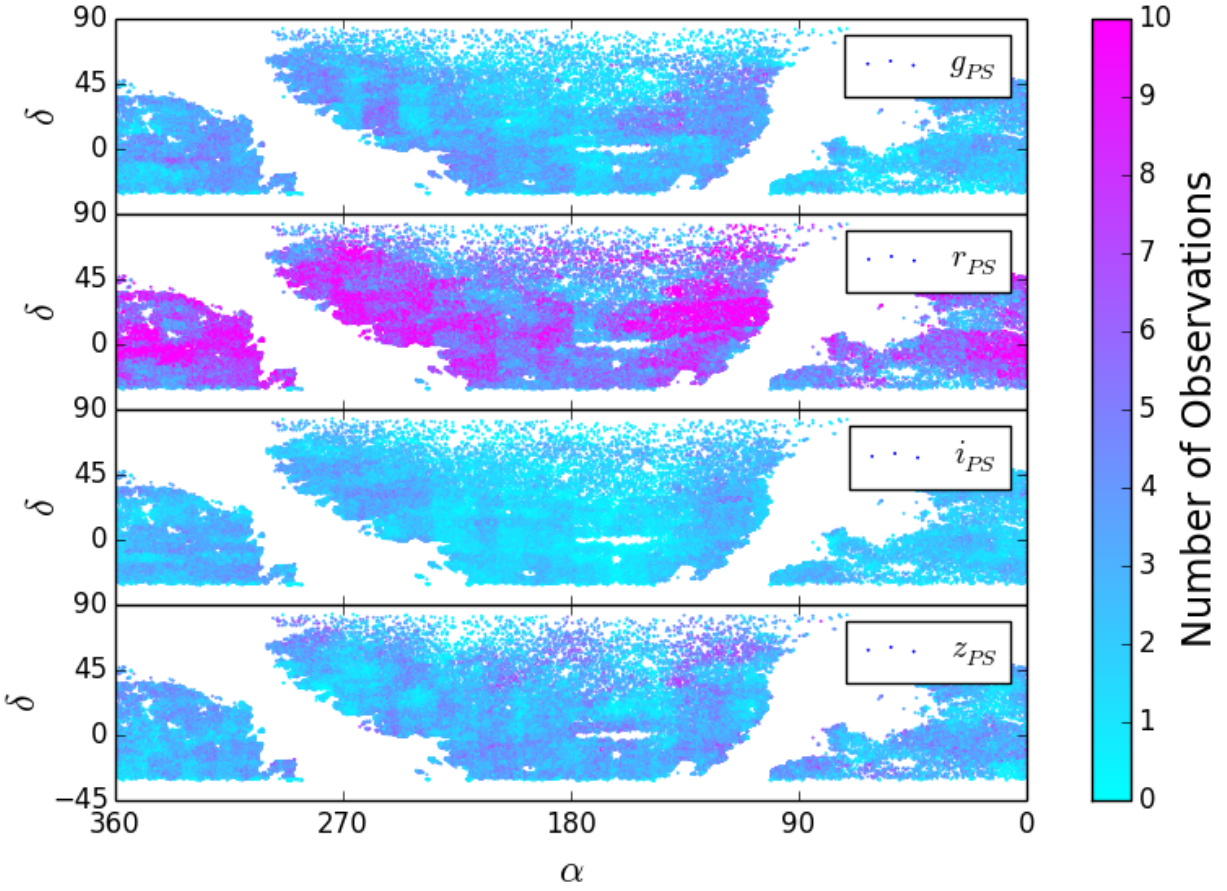


FIGURE 4.6: From top to bottom shows the number of observations in the four relevant Pan-STARRS passbands as a function of position on the sky. A few things are noticable: first, the coverage is not strongly correlated throughout the bands; secondly, the $r_{PS}$ filter seems to have more observations than the other bands; third, the holes in the data are essentially random.

number of points in the comparison ring divided by the number of points in the comparison disk. The error on the observation is assumed to be poissonian.

This search strategy allows us to reliably select comparison fields despite the patchiness of the Pan-STARRS data. Ideally one would want the comparison field for any given $(l,b)$ to be one of the points: $(-l,b)$, $(l,-b)$, $(-l,-b)$. However, this cannot be automated reliably in our data, so we opt for the pencil-ratio vs ring-ratio method. One weakness of our method is that false overdensities should inherently occur in the direction of the galactic center around the bulge.

A different way to put it, given the investigative point ($l'$,$b'$,$r'$):

$$\text{Cube} = \Sigma(\text{stars}) \quad \forall \quad |l_{\text{star}} - l'| < 5^\circ \quad \wedge \quad |b_{\text{star}} - b'| < 5^\circ \quad \wedge \quad |r_{\text{star}} - r'| < 5\text{kpc} \tag{4.5a}$$

$$\text{Pencil} = \Sigma(\text{stars}) \quad \forall \quad |l_{\text{star}} - l'| < 5^\circ \quad \wedge \quad |b_{\text{star}} - b'| < 5^\circ \tag{4.5b}$$

$$\text{Ring} = \Sigma(\text{stars}) \quad \forall \quad |l_{\text{star}} - l'| > 5^\circ \quad \wedge \quad |b_{\text{star}} - b'| < 5^\circ \quad \wedge \quad |r_{\text{star}} - r'| < 5\text{kpc} \tag{4.5c}$$

$$\text{Disk} = \Sigma(\text{stars}) \quad \forall \quad |l_{\text{star}} - l'| > 5^\circ \quad \wedge \quad |b_{\text{star}} - b'| < 5^\circ \tag{4.5d}$$

$$\text{Cube Concentration} = \frac{\text{Cube}}{\text{Pencil}} \quad ; \quad \text{Field Concentration} = \frac{\text{Ring}}{\text{Disk}} \quad ; \quad \sigma = \frac{\sqrt{\text{Cube}^2 + \text{Ring}^2}}{\text{Pencil}} \tag{4.5e}$$

$$\text{Degree Overdensity} = \frac{\text{Cube Concentration} - \text{Field Concentration}}{\sigma_{\text{Cube}}} \tag{4.5f}$$

See Figure 4.7 for a visual explanation of the search strategy.

## 4.3 Pan-STARRS Results

Here we present the results of running the search algorithm outlined in Section 4.2 on our Pan-STARRS data set. There are a few idiosyncrasies which we would like to note.

By the very design of the search algorithm – moving gridwise in $l$, $b$ and radius, r – the search is patently non-uniform. While our approach is sufficient for background subtraction purposes, sampling density is inherently anticorrelated with $|b|$ and heliocentric $r$. The results produce clustered grids of positive results by the nature of the search, as opposed to singular detections [in most cases].

The definition of 'overdensity' is a bit arbitrary. In this analysis we will constrain ourselves to the subset of samplings which have an overdensity degree [see Equation 4.5f] of at least three. This roughly corresponds to a $3\sigma$ overdensity over the background, but that definition is muddled by the presence of the spheroid [and any unmasked overdensity, such as the Virgo overdensity or the Hercules Aquila Cloud] in our comparison fields. The spheroid also produces positive results at low $l$ and $b$, this is problematic as it is also in the background field for all the other low $b$ fields, so this could make detection of anticenter features problematic.

In Figures 4.8 and 4.9 we show the collection of grid points which are significantly overdense, in a Kavrayskiy 7 projection $\alpha$-$\delta$ plot and a Galactocentric XYZ plot [respectively]. Also plotted are the data of the simulations of the Sagittarius tidal tails as calculated by Law & Majewski (2010). As expected from the nature of the search technique, there is a strong overdensity around the Galactic center – some of which may be attributable to the Hercules Aquila cloud discovered by Belokurov et al. (2007) and more recently analyzed by Simion et al. (2014).

The next most prominent features are those along the Sagittarius tidal stream. We find strong detections of both the leading and trailing arms which are in agreement with the previous Pan-STARRS Sagittarius study of Slater et al. (2013). However, while their study was performed using F-Turnoff stars, our intrinsically brighter BHBs allow us to probe deeper than they. We even see some hints of the Gemini arm which was noted first in BHBs by Newberg et al. (2003), later in BHBs by Clewley et al. (2005), in RR Lyrae stars by Drake et al. (2013), and by Belokurov et al. (2014) in BHBs, red giants and MSTO stars.

We also have an interesting little feature at [$\alpha$, $\delta$, r] = [143, -18, 30-40]. This feature happens to have been found by Starkenburg et al. (2009) ['group 6' of their Table 2] as a clumping of red giant stars in the Spaghetti Survey (Morrison et al., 2000) and is later confirmed by Avon Huxor in carbon stars

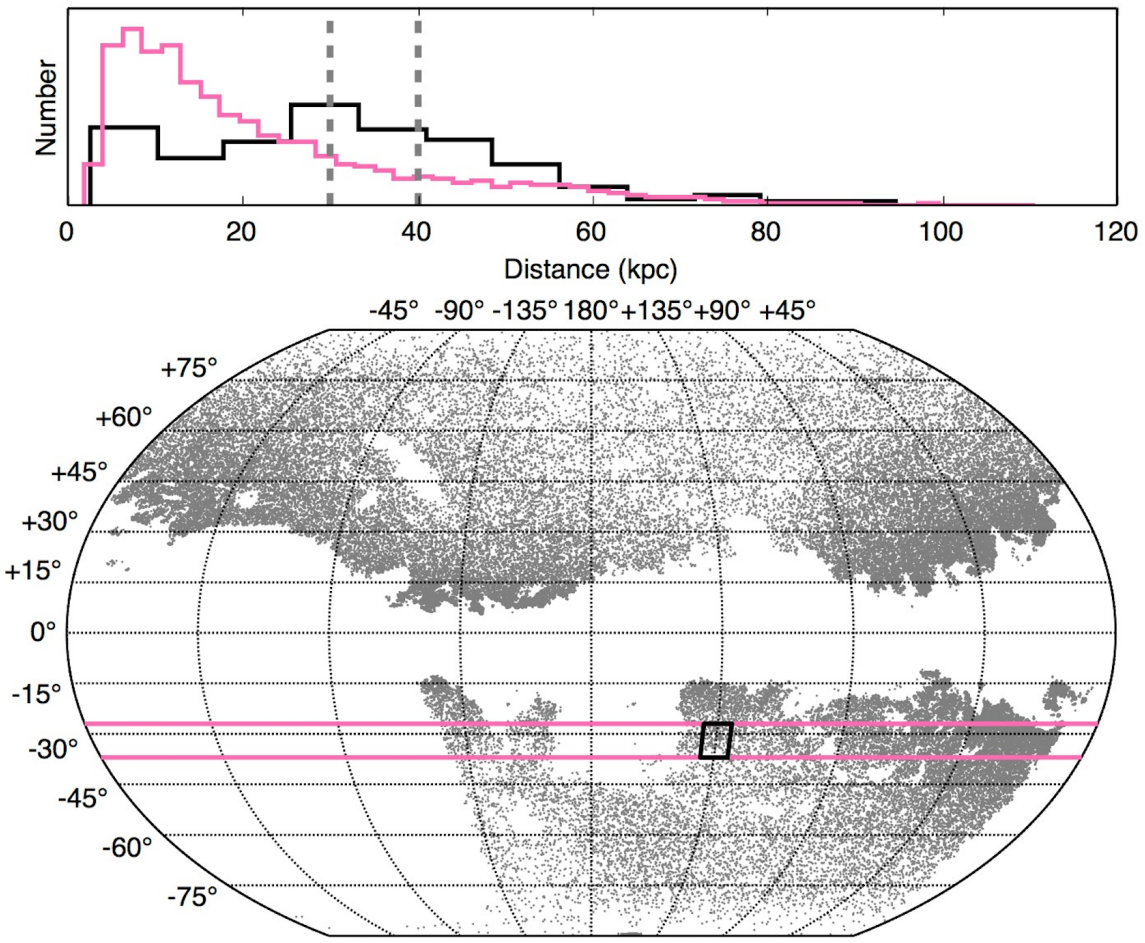


FIGURE 4.7: Pictorial explanation of the automated search strategy used to discover substructure in the Pan-STARRS data set. In the lower panel, we show the [$l$, $b$] positions of our BHB candidate data [grey] and one target-field pair [black and pink, respectively]. Note the negative space in the figure. In the bottom left of the figure is the section of sky not accessible at the observing site, the void is the area of sky below a $\delta$ of -30°; at 0, around the Galactic plane, is a wispy cut at an E(B-V) value of 0.1, so we see the profiles of dust tendrils emenating from the plane; the other patches, such as the one at [$l$, $b$] = [-100, 45] are caused by lack of sufficient observations in all colors [see Figure 4.6].

In the upper panel we histogram star counts as a function of distance in the target pencil beam [black] and the field [pink]; the distance was determined by comparing the apparent magnitude [reddening corrected by the maps of Schlegel et al. 1998] with the absolute magnitude give by Equation 4.4. The grey lines enclose a 10 kpc portion of the target histogram which would be identified as an overdensity of 3.3 sigma [since 18.2% of the data in the pencil beam is in this distance range, with an error of 3.4% and only 7.0% of field stars are in this distance range]. The entire sky is searched in a three dimensional grid in $l$, $b$ and r and assigned $\sigma$ overdensity values in such a manner.

[private communication]. It is interesting that we find this feature in both BHB stars and carbon stars since these objects probe quite different ages.

Then we have a few questionable detections. In the area of Triangulum Andromeda, we find two distinct detections; the northern one is at a distance of about 40 kpc from the sun, and the southern one looks to be a bit more distant, at 50 kpc. Two features have indeed been detected here by Sheffield et al. (2014), but they report the distances of the two structures to be at about 17 and 27 kpc, respectively. We note that our detection is on the fainter end of our investigative window, at about $19^{th}$ magnitude, and that this area of sky is rife with structure, and thus highly extincted. What could be causing this detection is main sequence stars being overcorrected for reddening and suchly shifted into our selection box. If we assume that this signal is purely MSA star contamination, and that the main sequence stars are a magnitude fainter then the BHBs, the distances change to 25 kpc and 31 kpc, which is closer to the literature value. However, if this is in fact a main sequence shadow to a BHB signal, it is perturbing that we see no sign of an actual signal at the corresponding distance. It is also strange that shadows are not evident elsewhere in our analysis. This problem needs to be investigated more thoroughly, most likely in a non-automated manner.

The spur of detections around [$\alpha$, $\delta$] = [275, 60] occurs at a well defined distance of 35 kpc and a blurred range from ∼42-48 kpc. This is in the same area of sky as Draco, but Draco is at a distance of 80 kpc. There are also no globular cluster in this area of sky according to the catalog of Harris (1996), 2010 revision. It would be interesting to revisit this with a different tracer.

The small clump at [$\alpha$, $\delta$] = [218, -28] is a detection at the very minima of our observing radius, so we disregard it as an edge effect.

We now return to a point alluded to in Chapter 3 – that of the tradeoff between color cut purity and color cut completeness. Out of curiosity, we modify our color cut to the much looser relations below:

$$(g-r)_{PS,0} < -0.015, \tag{4.6a}$$
$$(g-r)_{PS,0} > -0.5, \tag{4.6b}$$
$$(i-z)_{PS,0} < -0.025, \tag{4.6c}$$
$$(i-z)_{PS,0} > 0.45((g-r)_{PS,0} + 0.3) - 0.20, \tag{4.6d}$$
$$(g-z)_{PS,0} > 1.95((g-r)_{PS,0} + 0.05) - 0.30, \tag{4.6e}$$
$$(g-z)_{PS,0} < 1.95((g-r)_{PS,0} + 0.05) - 0.15. \tag{4.6f}$$

When instituting this color cut, by measure of the tests presented in Section 4.1, we select a sample that is only 55.3% pure but 70.8% complete [note that, when calculating the purity and completeness of this cut, we extend the color range of our 'true' BHB stars to go down to -0.5 and the magnitude box is allowed to go to 2.0 to account for the extreme horizontal branch]. This means that we should expect significant MSA shadows. Note that this color cut has a much bluer cutoff, hence the reason for our very blue $M_{r,PS}$ vs $(g\text{-}r)_{PS,0}$ fit in Section 4.1. We plot the results of running our search on these less stringent data and plot the results in Figures 4.10 and 4.11

Surprisingly the structure selection is very close to that of the more stringent color cut. One major difference is that another section of the Gemini arm appears, also at an extremely large distance. There appears to be more false detections in the plane, which is to be expected. Also, the unknown spur at [$\alpha$, $\delta$] = [275, 60] is greatly expanded in detection number and area and there appears to be a gradient in its distance.

The most interesting feature in this plot though, is the detection at [$\alpha$, $\delta$, ] = [0, -15, 50]. This is actually noticeable in the first iteration of this exercise, but the feature is much stronger now. This area is consistent with the position of the Sagittarius trailing tail in the models of Law & Majewski (2010) and is located in an area of sky not covered by the SDSS and which probes deeper than the study of Slater et al. (2013) in the same area.

Something additionally worth noting is the absence of certain structures. For example, we do not see many features in the area of the Monocerus or Virgo. This could be caused by a couple of effects. The absence of Virgo may be explained by Virgo's diffusivity on the sky compared to the found structures, it may indeed appear if the degree overdensity requirement is loosened – it is also relatively close to us, and near the limiting bounds of the search. The absence of the features in Monocerus could be explained by the background being systematically overestimated in the vicinity of the Galactic plane because of contamination to our search by the bulge. Another explanation could be that BHB stars do not adequately probe the populations which could be too young to host BHB populations.

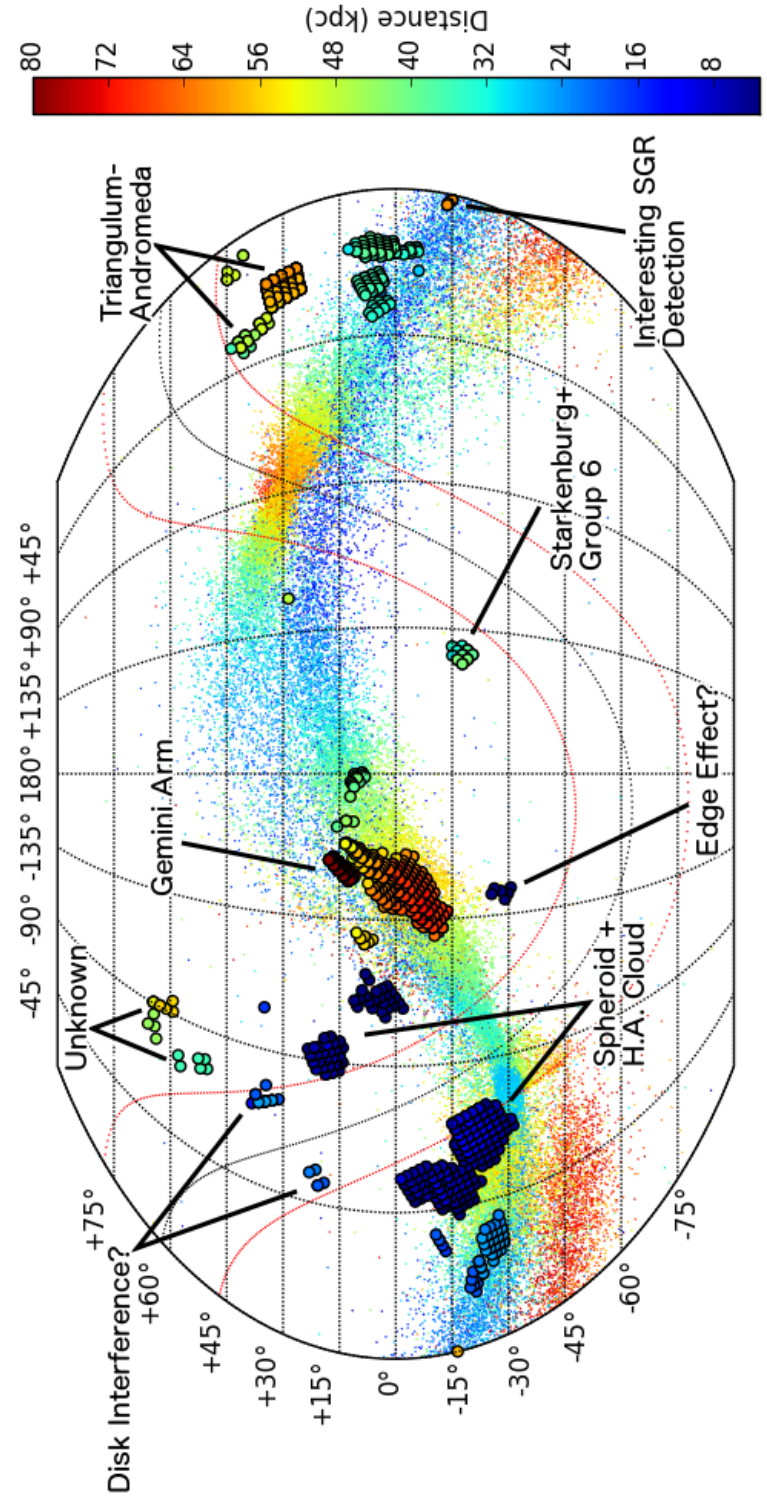


FIGURE 4.8: Kavrayskiy 7 projection in $\alpha$ and $\delta$ of our discovered overdensities (large circles) color coded by their distances from the Sun. In general the main features belong to the Sagittarius tidal debris (colored points). As noted in the text we recover many structures, which are labeled in the Figure. An important note is that the distance we find the Triangulum-Andromeda features disagrees strongly with that in the literature. Unless otherwise noted, detections are Sagittarius features. The footprint of the Pan-STARRS survey is shown in Figure 4.6. The Galactic plane is dotted in black and 15° from the plane is dotted in red.

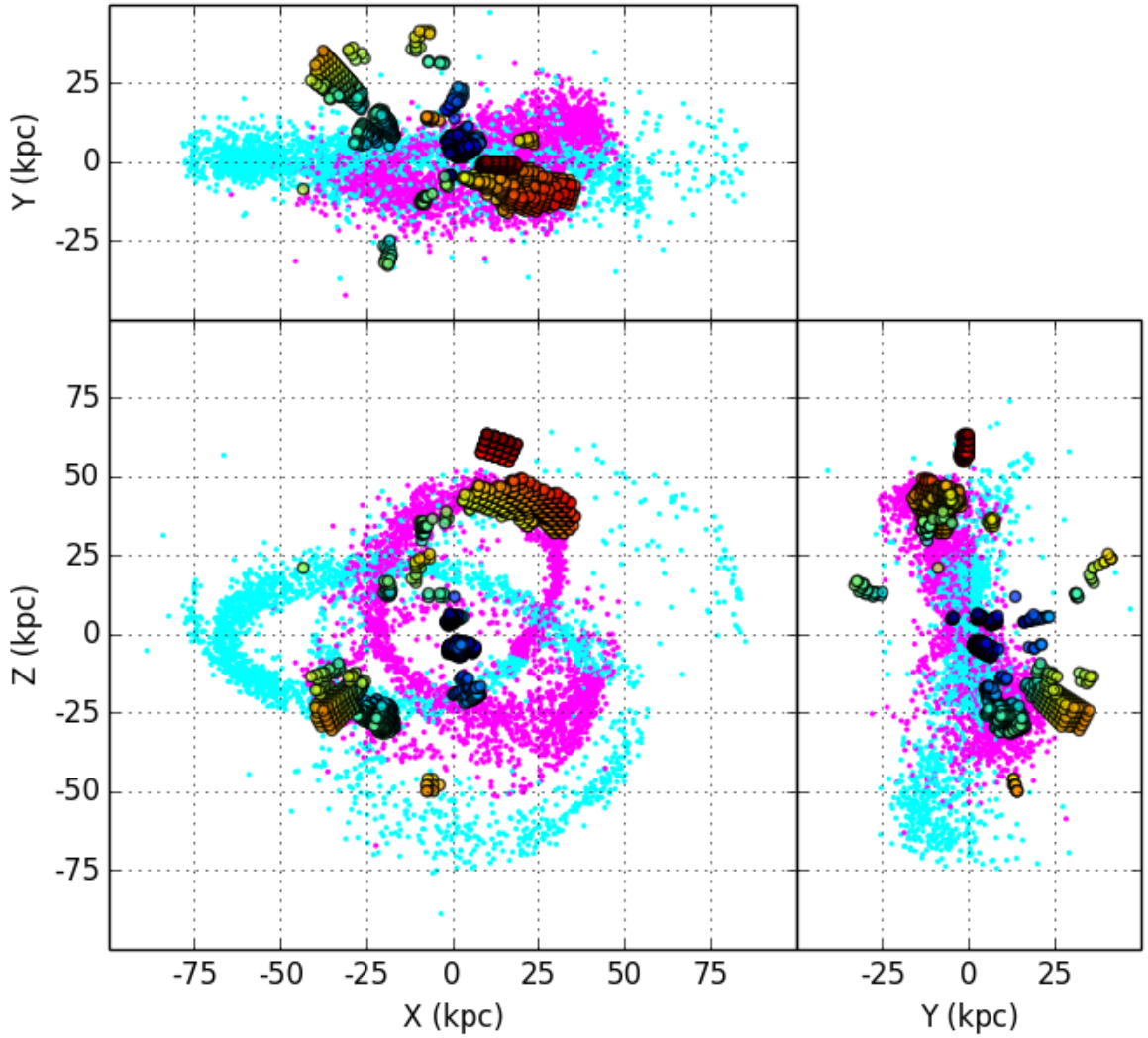


FIGURE 4.9: Galactocentric XYZ plots of the data shown in Figure 4.8. The color coding of the circles is identical to that in the prior figure to aid in cross-referencing. Shown in points are the leading [pink] and trailing [cyan] arms of the Sagittarius dwarf galaxy as modeled by Law & Majewski (2010). Of particular interest is the detection at $Z$=-50, this is a poorly constrained portion of the Sagittarius tidal stream.

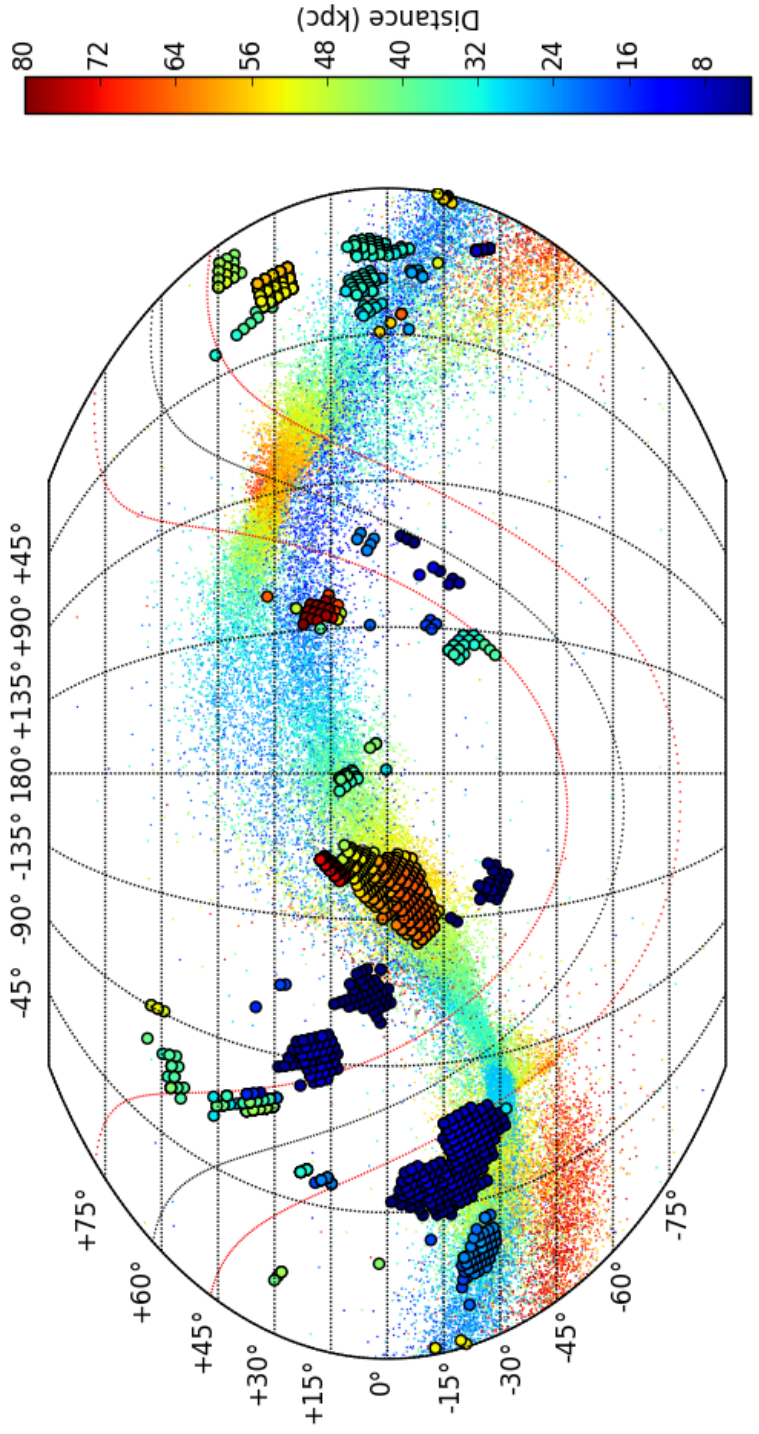


FIGURE 4.10: Identical to Figure 4.8 except the color selection used for these stars is much looser than the one used to select BHB stars in that figure. The stars used here are roughly 71% complete and 55% pure, as opposed to the prior figure which used stars that were 57% complete and 75% pure.

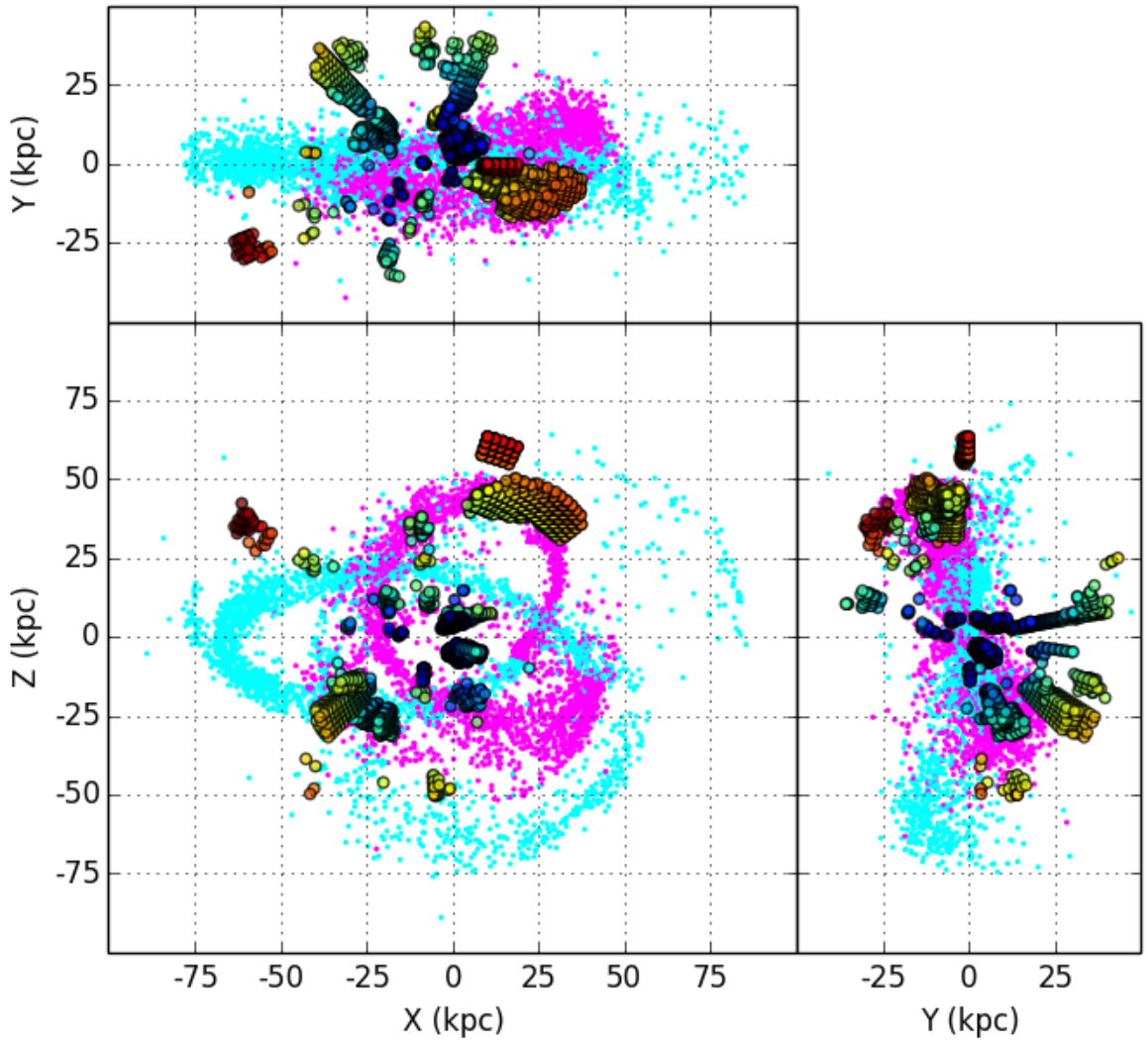


FIGURE 4.11: Identical to Figure 4.9 but with a looser, more complete BHB selection. This figure is paired with 4.10.

# Chapter 5

# Discussion for Part I

The study of the Galactic halo is an ongoing project. It has been studied using many types of stellar tracers such as main sequence stars (Newberg et al., 2002), blue horizontal branch stars (Xue et al., 2008) and carbon stars (Huxor & Grebel 2014, submitted); and it has been studied using various methods such as deep 'pencil-beam' surveys (Robin et al., 2000) or wide-field large area surveys (Deason et al., 2011).

The Pan-STARRS survey has the possibility to enhance and expand on all of these studies. Its narrow band filter set allows for high purity selections of stars based on their colors [F-Turnoff and blue horizontal branch stars being just two examples]; it's observing cadence allows, for the first time, wide area studies of variable objects such as RR Lyrae, long period giant variables, and supernovae, to name a few; and the survey structure of a $3\pi$ survey in conjunction with the ten so-called medium-deep fields [which are evenly spaced around the sky] allows for both wide area and deep pencil beam studies. The only missing link is the proper identification of said stars within the survey.

In light of this, we here develop a technique for identifying BHB stars in the Pan-STARRS data set.

In Section 3.1 we find, in agreement with Bell et al. (2010) and Sirko et al. (2004), that $u_{SDSS}$ based color cuts may photometrically select out samples of BHB stars which are $\sim$74% pure and $\sim$57% complete. We also show that the unexplored $z$ band is capable of selecting out samples of BHB stars with similar accuracies [for structural studies, purity is more valuable than completeness], having achieved an estimated purity of $\sim$77% based on spectroscopic data and globular cluster analysis. However, since the A-star separation by gravity is weaker in the $z_{SDSS}$ band than in the $u_{SDSS}$ band [as noted by Lenz et al. 1998], we obtained a lower completeness of $\sim$51%, in Section 3.2.

In Section 3.3 we show that this color cut allows structure mapping in the Milky Way to large distances. Structures such as the northern Galactic portion of the Sagittarius tidal stream, which are on the very edge of F-turnoff detectability, are easily discerned in their radial completeness. Thus this method may be used for large-scale structural analysis in addition to high efficiency spectroscopic targeting. In Section 3.4 we show the spectroscopic reasoning for the $z_{SDSS}$ band magnitude differences in BHB and MSA stars– namely that Stark pressure broadening causes the continua of these stars to exist at fundamentally different levels. In short, we suggest that this selection is an excellent addition to existing photometric selection methods for structure characterization via BHB stars.

In Section 4.1 we have recalculated a color cut for BHB stars using native Pan-STARRS photometry and devise a selection that is 75% pure and 57% complete.

We have also presented an automated technique for substructure search in Section 4.2. The technique is in its early stages and could use significant refinements. Firstly, we would suggest using a Galactocentric coordinate system: such a coordinate system would hopefully alleviate the false overdensities found in the direction of the Galactic center [and subsequent undersensitivity in the low latitude search bins]; however, this would be hampered by the fact that adopting a non-observational center to a coordinate system would result in significant photometric error asymmetry, a non-trivial problem. Perhaps a better approach would be to use simulated Milky Way stellar population models, such as the Besançon Galaxy Model of Robin et al. (2003) – or even empirical blue horizontal branch density models – to subtract the spheroid from the observed substructure. However, this is a difficult thing to implement given the inherent patchiness and roughness of the sky coverage. To truly implement this paradigm, one would need detailed information of each individual Pan-STARRS pointing contributing to the data set [i.e. subtracting a galaxy model density from a search cell will immediately invalidate any cell which has observational voids – this is the primary reason for choosing a ratio based strategy].

We believe that automation of search techniques is a valuable endeavor for many reasons. The first of which is the exponential growth of survey data set sizes: while the total SDSS catalogue occupies about 4 TB, the LSST in the 2020s will produce that amount of data *each night*. This is far too much data to plot and investigate by hand, so machine learning algorithms must be developed to automatically trawl the data and recognize patterns on their own.

A logical next step to this work would be to create a new observational 'mask' which includes all of the substantial substructure we find. By ignoring those sections of the Milky Way, we should be looking at just the smooth component of the Milky Way halo. The density profile of this smooth component is an ongoing investigation that would greatly benefit from the angular coverage and the depth of Pan-STARRS data.

# Part II

# A Fresh Look at Runaway Stars

*Alice sighed wearily. "I think you might do something better with the time," she said, "than waste it in asking riddles that have no answers."*
*"If you knew Time as well as I do," said the Hatter, "you wouldn't talk about wasting it. It's him."*
*"I don't know what you mean," said Alice.*
*"Of course you don't!" the Hatter said, tossing his head contemptuously. "I dare say you never even spoke to Time!"*

- Lewis Carroll, *Alice in Wonderland*

# Chapter 6

# Introduction to Part II

In this Part, we indirectly probe the structure of the Milky Way halo by looking at a specific side effect of the structure: stars that are dynamically ejected into unnatural phase spaces. We know that when stars come too close to galactic structures, the stellar density in that area rises, which leads to increased chances for dynamical ejections. This is useful for attempting to map the spiral arms of the Milky Way without actually observing the spiral arms, for example. Another common perturber is black holes; a specific type of star known as a Hills star is launched into highly eccentric and possibly unbound orbit by close interaction with the supermassive black hole believed to reside at the core of the Milky Way. By investigating stars flying out of the center of the Galaxy, we can draw inferences as to the stellar structure in the Galactic nucleus, despite it being observationally opaque to us.

In the introduction, we outlined a variety of possible scenarios that could lead to the creation of a so-called 'runaway' star. Usually these are thought of as phenomenological objects, and since they need to be spectroscopically observed, they have traditionally been studied in small numbers and only in high mass stars. However, the ejection scenarios will eject any type of star and will produce ejecta at a gradient of velocities. We examine this facet of the runaway star problem by considering large databases with six dimensional information of low mass stars.

Up until very recently, studies of these ejected objects have been limited to high mass early type stars. This is because it is much easier to find high probability candidates for follow up. Looking at faint magnitudes and high latitudes, one composes a sample of short lifetime objects based on their colors; the faintness ensures a great distance for these intrinsically bright objects, and the high latitude ensures a Galactic halo location [where no high mass stars should naturally reside]. Follow up spectroscopy is then needed to confirm the spectral type and to find the velocity and distance with high precision.

Now however, with large spectroscopic surveys such as SDSS, RAVE, and LAMOST, tremendous amounts of spectra are being collected over vast areas of the sky. When combined with long baseline astrometric measurements from the USNO catalog, proper motions may be calculated. All that is left is to estimate distances to objects using photometric distance estimations [such as isochrone fitting, see Figure 7.1] and six dimensional phase space information for hundreds of thousands of objects can be estimated.

It is only recently that studies have begun to investigate low mass stars which may have been ejected from their neighborhoods of birth, see for example Palladino et al. (2014). Using a previously unexploited sample of red stars [typically F-to-M type], we assign them likelihoods based on their phase

[0]This work was submitted to the Astronomical Journal as "Vickers, Smith & Grebel, 'Red Runaways: Hypervelocity Stars, Hills Ejecta and Other Outliers in the F-to-M Star Regime"' and is currently under review.

space coordinates and use these likelihoods to characterize them as a function of their probability of being runaways.

Owing to contradictory usage of terms in the literature, we would now like to declare the nomenclature used for the rest of this Part. When we use the term *hypervelocity*, we mean that the star is traveling fast enough to escape the potential of the Milky Way. The term *Hills star* will be used to denote a star which may have interacted with the central supermassive black hole. We will refer to stars which have kinematics similar with their neighbors as *natural* and stars with unlikely kinematics will be referred to as *outliers*.

In Section 7.1.1 we outline the data used in this study and characterize the reliability of the proper motion measurements. In Section 7.1.2 we explain the methods used to calculate object phase space information and orbital parameters. Section 7.2.1 explains the methodology we use to fit phase-space profiles to the data; and Section 7.2.2 details the usage of these fits to generate a likelihood value for every star based on its six dimensional position. Section 7.3.1 analyzes the relationship between this assigned likelihood and the characteristics of the stars: in Sections 7.3.2 and 7.3.3 we present possible hypervelocity stars and possible Hills stars. We conclude at the end.

# Chapter 7

# Runaway Stars in the SDSS

## 7.1 Data

### 7.1.1 Pipeline Products

For our object sample, we utilize SDSS Data Release 10 (Ahn et al., 2014) objects with high quality spectroscopic parameters. To date, the SDSS has collected over a million science quality spectra, of which over 500,000 are point sources, the majority of these being stellar objects. These objects – with proper motions, radial velocities, distance estimates [not from the SDSS pipeline products, but rather a separate method outlined below] and high-precision astrometry – possess full six dimensional phase space information. This large set of phase-space data forms the basis of our analysis.

The SDSS offers a selection of stellar atmospheric parameters in its SSPP. In this work we limit our sample to spectra with signal to noise ratios of ten or higher – this corresponds to atmospheric parameter estimate errors of about: $\Delta T_{eff} \sim 103.9$ K, $\Delta log(g) \sim .282$ dex and $\Delta[Fe/H] \sim 0.213$ dex [for the pipeline adopted values; see Table 6 of Lee et al. 2008]. We also use the radial velocity outputs from the SSPP. Radial velocities are generally found via ELODIE template matching and have accuracies from 4 to 15 km $s^{-1}$ [depending on the quality of the spectra, see Table 2 of Yanny et al. 2009]. As a quality control measure, we reject any object which is critically flagged by the pipeline [see table 7 of Lee et al. 2008 for a list of pipeline flags], while cautionary flags are allowed to pass.

In this chapter we wish to focus on disk-origin objects which have non-disk kinematics. To weed out the halo, we investigate only objects with SSPP metallicities greater than -0.8 dex. An object with such a high metallicity, which is found to be inconsistent in its kinematics with its neighboring high metallicity stars, is a candidate runaway star.

For our distance estimates, we use a main sequence color-magnitude relation described by Ivezić et al. (2008); for this relation to be valid, the objects investigated must fall in the main sequence color range $[0.3 < (g\text{-}i)_{SDSS,0} < 4.0$ and have dwarf-like surface gravities $[log(g) > 3.0]$. In essence these cuts select luminosity class V objects from early F to late M type. As a final quality cut, we also cull all data which have error measurements on any parameter which is more than $3\sigma$ greater than the average error measurement of the data for that parameter [i.e. we cut off the long tails of the error distributions]. A summary of the selection criteria for our final sample is outlined in Table 7.1.

We note that proper motion measurements are probably the least reliable portion of this analysis. We have devoted Part III to discussing this.

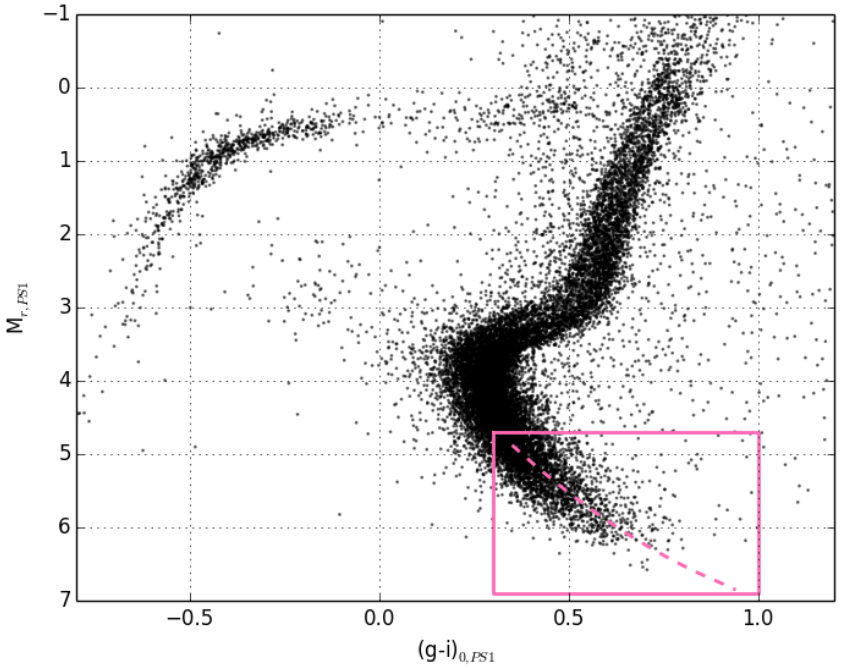


FIGURE 7.1: Color Magnitude Diagram with the main sequence region boxed in pink. The dashed line roughly indicates the relationship we use to estimate the absolute magnitudes of stars based on their colors and metallicities.

| | Lower Bound | Upper Bound |
|---|---|---|
| $u_{SDSS}$ | 12.0 | 22.0 |
| $g_{SDSS}$ | 14.1 | 22.2 |
| $r_{SDSS}$ | 14.1 | 22.2 |
| $i_{SDSS}$ | 13.8 | 21.3 |
| $z_{SDSS}$ | 12.3 | 20.5 |
| $(g\text{-}i)_{SDSS,0}$ | 0.3 | 4.0 |
| SSPP SNR | 10. | - |
| Fe/H | -0.8 (dex) | - |
| Fe/H Error | - | 0.14 (dex) |
| log(g) | 3.0 (dex) | - |
| log(g) Error | - | 0.32 (dex) |
| Radial Velocity Error | - | 3941.18 (km $s^{-1}$) |
| Proper Motion $\alpha$ Error | - | 11.15 (mas $yr^{-1}$) |
| Proper Motion $\delta$ Error | - | 11.15 (mas $yr^{-1}$) |

TABLE 7.1: Note that once all cuts are applied, the maximal radial velocity error is actually 53.98 km $s^{-1}$. The apparent magnitude limits are chosen by the 95% limiting magnitudes of the SDSS survey from the SDSS website and the saturation limits of the camera from Table 4 of Gunn et al. (1998).

### 7.1.2 Calculated Distances, Velocities and Orbits

Assigning distances to the objects is accomplished by a photometric estimate of the absolute magnitude of main sequence stars based on their $(g\text{-}i)_{SDSS,0}$ colors. This estimate is given in parametric form in Appendix A of Ivezić et al. (2008). Their estimate is obtained: by fitting globular cluster photometry in combination with their distances as tabulated in the catalog of Harris (1996) in the SDSS footprint for the bluest objects; with a combination of literature photometric distance estimate fits in the middle color regime; with Hipparcos M-dwarfs where possible more redward; and with ground based parallaxes for the reddest objects [see Ivezić et al. 2008 and Jurić et al. 2008 for more details]. This estimate accounts for metallicity by applying a polynomial correction to the estimated magnitude which is determined by comparing offsets of the estimated and true relations of a set of globular clusters as a function of the Harris Catalog metallicity estimates. These magnitudes are estimated to have a scatter of $\sim 0.1$ to 0.2 – this is accounted for later. We assign distances to our data by applying this photometric estimate and adding in the metallicity correction using SSPP spectroscopic metallicities.

It is notable that the color-magnitude relation outlined above [which is based on five clusters with metallicities below -1.27 dex] may be inaccurate at high metallicities. This inaccuracy will be pronounced in the vicinity of the turnoff since globular cluster turnoff colors and magnitudes are functions of the age and metallicity of the cluster. To rectify this, Dartmouth isochrones (Dotter et al., 2008) of varying metallicities are compared to the empirical relation of Ivezić et al. (2008) by Smith et al. (2009) and an additional correction is presented in their paper.

For assigning Galactic Cartesian X, Y, and Z coordinates to objects, we assume that the sun has a position of -8.0 kpc and that the system is right handed [with X increasing toward the Galactic Center and Z increasing toward the Northern Galactic Pole].

Assigning velocities to the objects is straightforward. We initially assign Cartesian U,V,W velocities [= dX/dt, dY/dt, dZ/dt] to the objects, in a manner similar to Johnson & Soderblom (1987)[1] using the prior outlined proper motions and radial velocities.

The cylindrical rotational [$v_\phi$], radial [$v_R$] and vertical velocities [$v_Z$] are then calculated in the standard fashion. The direction of $v_\phi$ is chosen to be right handed [i.e. the Solar rotation speed is -220 km s$^{-1}$].

In short, all systems used are right handed with Galactocentric origins.

We calculate the orbital paths for each star in the data set by integrating their positions and velocities through the potential presented in Dehnen & Binney (1998). Of the 35 available potentials, we use 2b. This potential was chosen by rough comparison of the Galactic parameters in Tables 3 and 4 of Dehnen & Binney (1998) with Tables 2 and 3 of the more recent study by McMillan (2011).

In this model, the disk is composed of 3 exponential density constituents: an interstellar medium component, and the thin and thick stellar disks. The bulge and halo density profiles are each described by spheroidal functions. Then the total gravitational potential is made to satisfy Poisson's equation and is brought into agreement with observational constraints such as the Milky Way's rotation curve and peak velocities of the interstellar medium. For full details, please refer to the paper of Dehnen & Binney (1998); the code is made available as part of the NEMO Stellar Dynamics Toolbox[2].

The orbits are calculated for every star in our data set by reversing their U,V,W velocities and running them through the potential for 14 Gyr at a 1 Myr resolution. The choice of a 14 Gyr integration time is to ensure we find crossings where possible. This does not account for a changing Milky Way potential,

[1] see *http://idlastro.gsfc.nasa.gov/ftp/pro/astro/gal_uvw.pro* for example IDL code

[2] http://carma.astro.umd.edu/nemo/

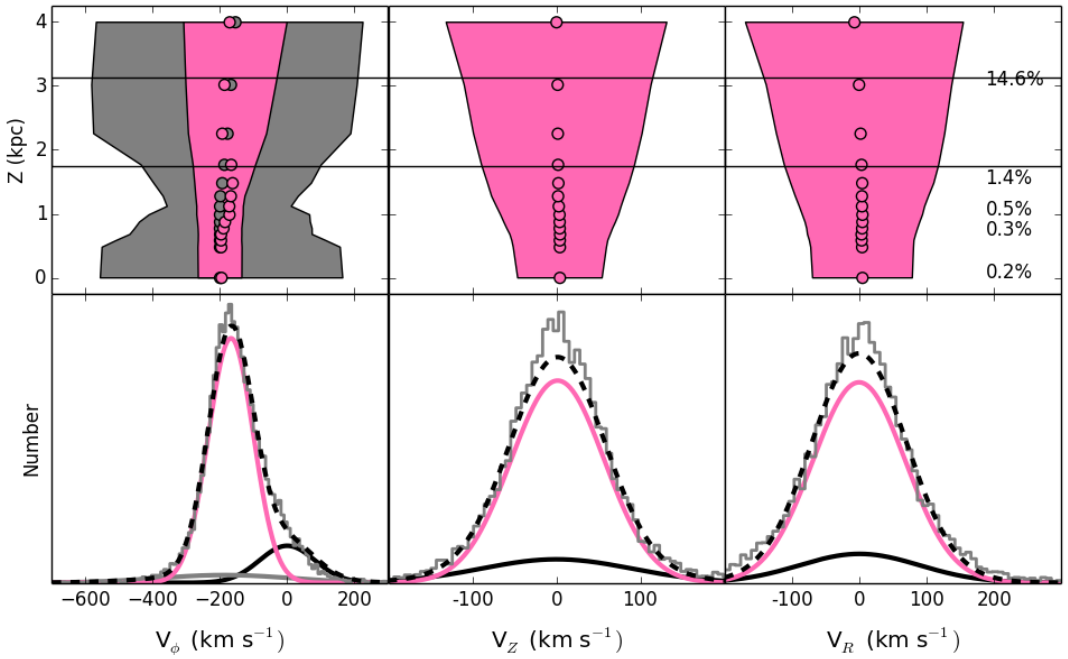


FIGURE 7.2: *Upper Panels*: The global fits to the velocity distributions of high metallicity stars at various distances from the Galactic plane. The shaded regions enclose the $2\sigma$ ranges about the means [circles] for the fit Gaussians [pink]. In the case of $v_\phi$, an additional Gaussian component [gray] is fit to the data to account for the heavy-tailed nature of that profile.
*Lower Panels*: The fits for the data slice at Z$\sim$2.2 kpc [horizontal lines at 1.74 kpc and 3.13 kpc]. The solid Gaussians correspond by color to the shaded regions described above [with an additional black Gaussian representing the halo]. The data are shown with a gray histogram and the global fit is shown as a dashed line.
*Annotations in the Top Right Panel:* Indicates the percentage of fits at various $Z$ values which is devoted to the halo. This percentage is determined by doubling the counter-rotating population.

but since the average lookback time to the previous crossing is $\sim$39 Myr, we do not consider this to be an issue. When a planar crossing is detected, a linear interpolation between the calculation steps before and after the crossing is used to find the exact coordinates and velocities of the crossing point.

## 7.2 Fitting and Likelihoods

### 7.2.1 Fitting Kinematic Profiles to the Data

To find outlying objects, we must first define the expected distribution of stars in phase space. To do this, we fit the kinematic properties of the objects [$v_R$, $v_Z$ and $v_\phi$] at different distances from the plane of the Galaxy to Gaussian mixture profiles. By interpolating between these fits, we can infer the expected velocity profile of an object at any distance from the plane.

Fitting is performed by cutting the data set into $Z$ slices with 20,000 members per slice [after the data quality checks, we have about 135,000 objects] and the fits are boxcar smoothed with a step

size of 10,000 [so the data are cut into 14 slices each of which have 10,000 members in common with the previous slice, and 10,000 in common with the next slice]. This dynamic binning offers a similar robustness of fit for each slice [excepting the most distant slice], but suffers from a differential resolution of the fits, with the more distant bins growing wider and wider apart due to less complete sampling [notice that very close bins are also wider apart due to the bright limit of the SDSS survey]. The median bin size is about 0.32 kpc. A mixture of Gaussians is then fit to the members of each slice in each cylindrical velocity component.

$v_\phi$ is the most complex profile to fit. The distribution of rotation speeds in the disk is known to be non-Gaussian, with a heavy tail extending to slower rotation velocities [due to asymmetric drift – the effect where $v_\phi$ is inversely correlated to the random motion of a star; see Section 10.3.1 of Binney & Merrifield 1998 pp. 624-629]. This can be described using physically motivated models, such as the one presented in Schönrich & Binney (2012), or simply by fitting two Gaussians to the disk population in $v_\phi$ [which is the approach we take]. As the $Z$ value of the fitting slice increases, a counter rotating population becomes increasingly evident. Despite the high metallicity cut, some halo population appears to be leaking into our sample. To rectify this, a halo population is added into the fit. The halo population's membership is defined to be twice that of the counter rotating population [the equivalent of assuming the halo population is non-rotating and that the entire counter rotating population has halo membership]. Moreover, the halo population is assumed to have a dispersion invariant with respect to $Z$ and no net motion.

The $v_R$ and $v_Z$ distributions of the disk are much more symmetric, so they are each fit to single Gaussians. An additional halo component is also added to these fits, with the normalization of this component again being determined by the counter rotating population; again we assume no net motion and a constant dispersion of velocities at all heights from the plane.

The fitting is done via a maximum likelihood method using the Markov Chain Monte Carlo technique, carried out on each $Z$ slice in turn. Each velocity component in the slice is fit with the following probability density function:

$$P(v_k) = \sum_{j=1}^{N} A_j \frac{1}{\sigma_j \sqrt{2\pi}} e^{\frac{-(v_k-\mu_j)^2}{2\sigma_j^2}}, \tag{7.1}$$

where k corresponds to the velocity component [i.e. $v_R$, $v_\phi$, $v_Z$], N is the number of Gaussian components in the fit [i.e. N = 2 for $v_R$ and $v_Z$, N = 3 for $v_\phi$], and $A_j$ is the normalization of each Gaussian. The halo Gaussian is mostly fixed, with $\mu_R = \mu_\Phi = \mu_Z = 0$ km s$^{-1}$ and $\sigma_R = 138.2$ km s$^{-1}$, $\sigma_\Phi = 82.4$ km s$^{-1}$ and $\sigma_Z = 89.3$ km s$^{-1}$ (Smith et al., 2009). The normalization of the halo is determined from the fit to $v_\phi$ [see above].

The parameters for the above fits are determined by carrying out a maximum likelihood calculation, with the likelihood for each velocity component k given by:

$$\mathcal{L} = \prod_{i=1}^{N_{star}} P(v_k^i), \tag{7.2}$$

where the product is carried out over the total number of stars in the slice [i.e. $N_{star} = 20{,}000$].

The global fits are depicted in 7.2 [the means of the fitted Gaussians are plotted as points, and the standard deviations are depicted by filled areas as a function of distance from the plane].

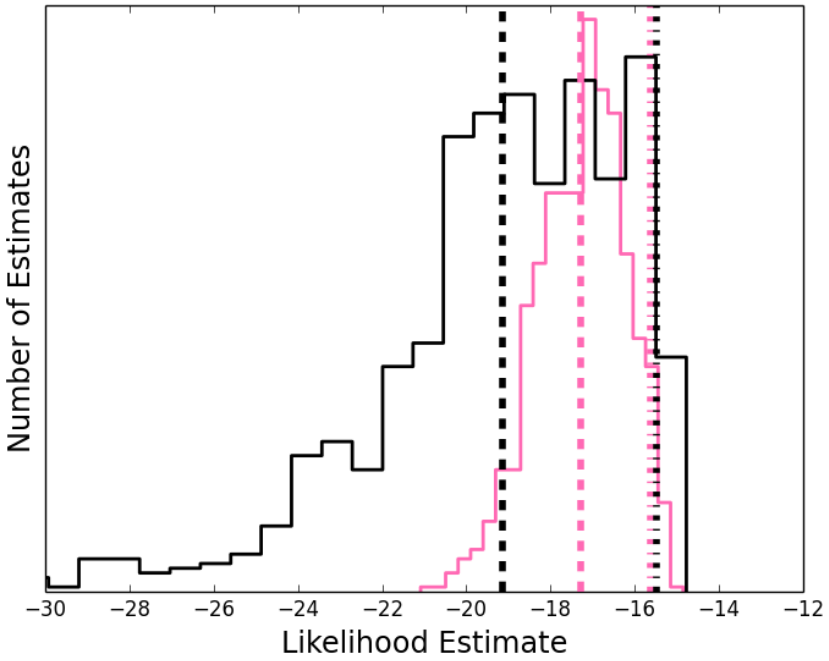


FIGURE 7.3: Example of how we assign likelihoods to stars. In this figure we show two Monte Carlo expansions of the same object. The pink histogram represents the likelihood distribution of 1000 realizations of the star and the dashed and dotted pink lines represent the average likelihood and 95% highest likelihood of these expansions [respectively]. The black histogram, dashed and dotted lines are the same except the errors on the base star's measurements have been inflated threefold. We see that the object with large errors would have a much lower average likelihood than the object with small errors, despite being from the same underlying observations. However both expansions have very similar 95% likelihoods. We use the 95% likelihood instead of the average likelihood in order to ensure that our outlier stars are true and not classified as outliers merely because of large errors.

It should be noted that these fits are not intended to provide any physical insights into the disk. These fits are just probability density functions of high metallicity stars and are used to find kinematic outliers within this high metallicity population. For more proper analyses of disk population kinematics, we direct the reader to Smith et al. (2012), Schönrich & Binney (2012), and the review of Rix & Bovy (2013).

### 7.2.2 Assigning Likelihoods to Stars Based on the Kinematic Profiles

To find outliers, we use the Gaussian fits from the previous section as probability density functions. These probability density functions, which vary as a function of height from the plane, fit the overall distributions of our high metallicity stars. Outliers in these fits are likely also outliers of the underlying population.

In order to quantify the likelihood that the $i^{th}$ star is consistent with the underlying distribution, we calculate the product of the probabilities for each velocity component:

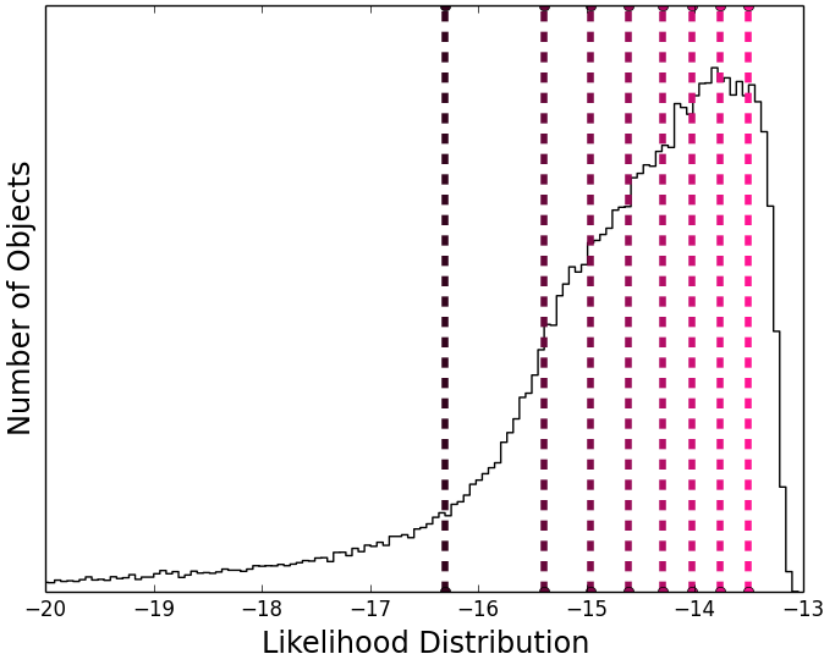


FIGURE 7.4: The likelihood distribution for all objects in our sample. Objects with higher likelihoods exhibit disk like motions. Objects with low likelihoods have incongruous phase space values compared to the rest of the objects in their vicinity [for example they may be counter-rotating or have high W velocities]. The vertical lines indicate divisions between 9 equally populated likelihood bins for the stars. These data are compared in Figures 7.5 and 7.6, and the division colors here roughly correspond to the color gradients in those figures.

$$P_i = P(v_R^i)P(v_\phi^i)P(v_Z^i). \tag{7.3}$$

Here the probabilities for each velocity component are calculated using Equation 7.1, taking the best-fit parameters determined for the relevant slice in $Z$. Clearly velocity outliers, such as stars ejected from the disc, will have low values of $P_i$.

We now incorporate the errors on the observational measurements which have, until this point, been neglected. For each individual star we create a sample of 500 error-incorporated realizations by Monte Carlo sampling the relevant measurements [$g_{SDSS,0}$, $r_{SDSS,0}$, $i_{SDSS,0}$, [Fe/H] for the distances; radial velocity, and proper motions for the kinematics]. An additional 7% error is factored into the distance estimates to account for the uncertainty in the color-magnitude relation (Ivezić et al., 2008). Each realization is assigned a likelihood using Equation 7.3 and in such a manner a distribution of likelihoods for each star is constructed.

One of the largest concerns of our analysis is the presence of large uncertainties in the observational measurements; for example, a star with a large uncertainty in its proper motion could be reported to have a very large spatial velocity, even though the large uncertainty means that it could be consistent with a more moderate velocity. By using this Monte Carlo approach to obtain a distribution for $P_i$, rather than an individual value, means that we can weed out stars with large uncertainties. This is important because the non-linearity of the velocity calculation means that the Monte-Carlo likelihood distributions could be very asymmetric, with large tails to low probabilities. This will have greatest

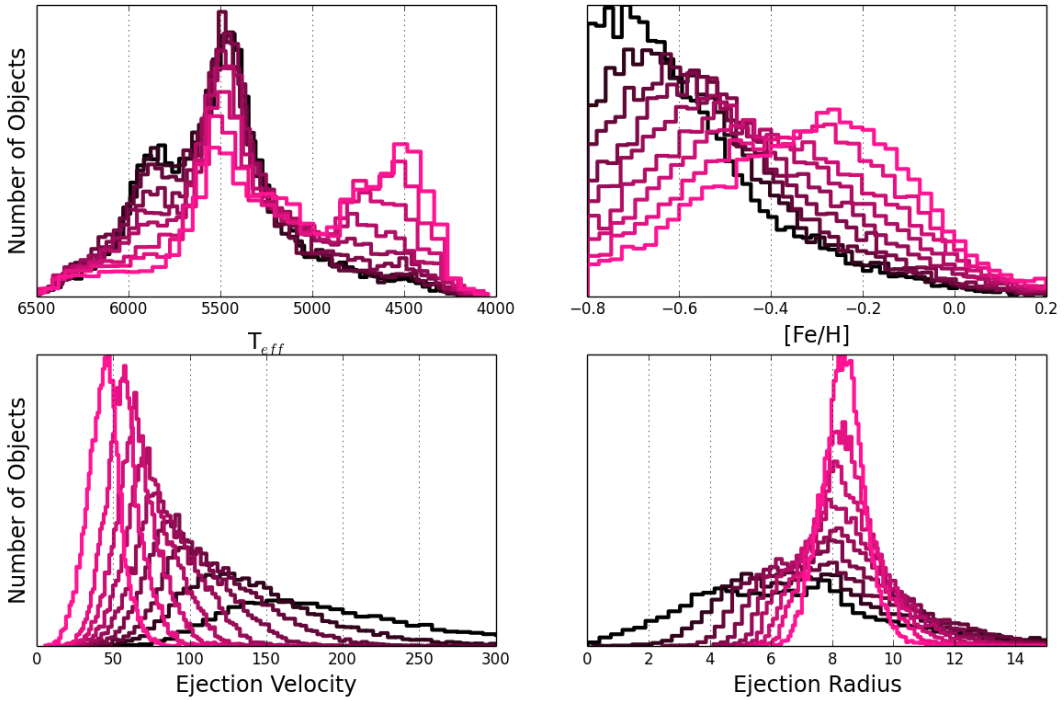


FIGURE 7.5: Trends in fundamental properties [$T_{eff}$, [Fe/H]] and orbital crossing properties [crossing velocity and Galactic radius] of the stars as a function of their likelihood [see Figure 7.4]. We see that outliers [black] are: hotter, more metal deficient, have faster crossing speeds, and more probably crossed last at smaller radii than the natural stars [pink].

impact on the stars in the high-velocity tails of the velocity distributions, which are the very stars we are most interested in.

To overcome this problem, for each star we adopt as its likelihood the 95% highest likelihood from the Monte Carlo resamples. For objects with small uncertainties, this adopted likelihood will be close to the average likelihood of the distribution. For objects with large uncertainties, the adopted likelihood will be much higher than the average. This helps to clean our final sample of low likelihood stars, removing objects which have low likelihoods merely by virtue of their large uncertainties. This is illustrated in Figure 7.3.

Figure 7.4 depicts the distribution of 95% likelihoods for all of the stars we investigate.

## 7.3 Analysis

### 7.3.1 General Characteristics

Having assigned likelihoods to all of the objects based on their phase space information, we now wish to investigate the attributes of the outliers in relation to the natural stars. To do so, we split the data into 9 equally populated partitions based on their calculated probability [see Figure 7.4].

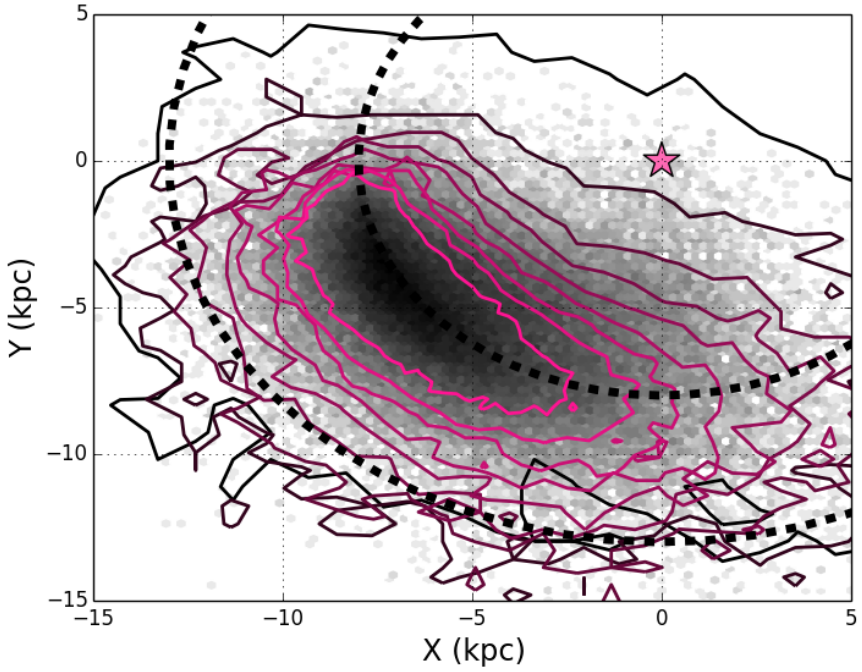


FIGURE 7.6: The last point of Galactic plane crossing for our objects. The grayscale density is a logarithmically weighted hexbin of all of the objects' crossing points. The objects that we observe seem most densely concentrated on an orbit similar to that of the Sun. Notice that there is a surplus of objects observed coming from the Galactic center as opposed to traveling inward. The inner dashed line indicates an 8 kpc radius circle about the Galactic center [the star]. The outer dashed line traces a circle with a 13 kpc radius, where the density of the disk begins to drop dramatically in early type stars according to Sale et al. (2010). The contours follow the color scheme of the prior two plots: natural stars are indicated in pink, and outliers are black. The contours show the $2\sigma$ limits for the crossing areas of the objects. The natural stars follow the local rotation, while the outliers show a preference to originate from more Galactocentric regions.

We also investigate the crossing velocities and crossing radii of these objects. By integrating their orbits back in time, we can calculate approximately where they last crossed the Galactic plane and their velocity at this point. We refer to the radius of their last crossing point [with respect to the center of the Galaxy] as the 'ejection radius' and to the velocity with which they crossed the plane as the 'ejection velocity.' We correct the ejection velocity by accounting for the rotation curve of the Galaxy presented in Clemens (1985) [so the ejection velocity indicates the crossing velocity with respect to the local standard of rest [LSR] at the crossing distance; note that we scaled the fit in that paper to have a solar position of 8 kpc instead of 8.5 kpc, to maintain the internal consistency of this Chapter].

Note that we assume here that the last crossing time was the point where the object was ejected, if it was ejected. The outliers are our main candidates for objects being involved in possible ejection events and form the basis for our analysis of ejection mechanisms acting on main sequence stars. There is no clean cut between outliers and natural stars – instead it is a smooth transition and only general properties can be investigated.

In Figure 7.5, we histogram the characteristics [ejection radius, ejection velocity, metallicity, and temperature] of all of the objects we investigated in nine equally populated, color coded bins [the cuts again

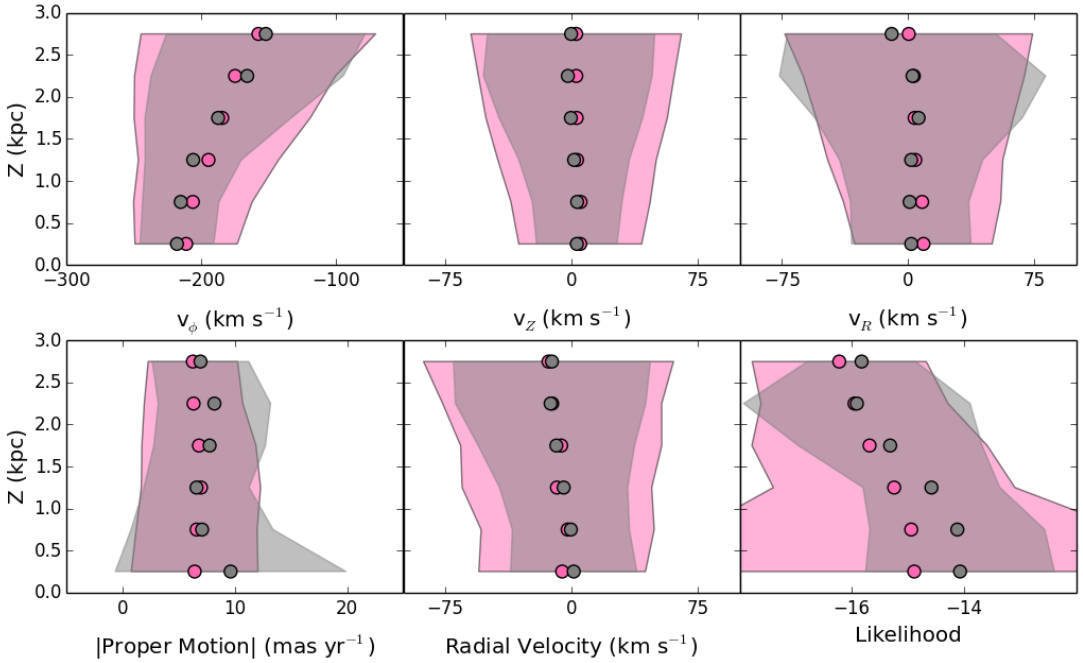


FIGURE 7.7: *Upper Panels*: Cylindrical velocities as a function of distance from the Galactic plane. The average cylindrical velocity [points] and dispersions [shaded areas] are shown for early type [$T_{eff} > 5700$ K] and late type [$T_{eff} < 5000$ K] stars [pink and gray, respectively]. We see that the rotational velocities of the two populations are consistent, which implies that the distance estimates are unbiased. We also see that the kinematics of early type stars are usually more dispersed [especially in $v_\phi$ and $v_Z$] which would explain their generally lower likelihoods.
*Lower Panels*: The measured proper motion magnitudes [left] and radial velocity magnitudes [middle]. We see that the early type stars are more dispersed in radial velocities than the late type objects, while having similar proper motion measurements. Since the radial velocities are much more reliable than the proper motions, this implies that the early type stars are actually kinematically hotter than the late type stars. On the right we have the likelihood calculation as a function of $Z$. We see that the early type stars are less likely than the late type stars at all distances from the plane– this is consistent with a dynamically hotter population.

being shown in Figure 7.4]. From these figures, we note four trends:

1) The natural stars are generally of later stellar types than the outliers. The population of G dwarfs is primarily orbiting more or less normally, while the population of early F dwarfs is more anomalous in its kinematics.

2) In general, the higher the metallicity, the more normal the rotation.

3) As expected, objects exiting the disk with large velocities compared to the LSR are less likely than objects rotating along with the LSR.

4) The natural stars, probably in orbits very similar to that of the Sun, have last crossed the disk at radii close to that of the Sun's orbit. The outliers have more varied crossing positions, but tend to come from closer to the Galactic center.

So, the natural objects are low temperature, metal rich, slow, and on orbits coincident with that of the Sun. The outliers are of earlier stellar types, metal poor, fast, and have a greater variance in crossing positions [with a tendency to be traveling outward from the more central regions]. While the metal poor end of our data may suffer some halo contamination, the anisotropic velocities [i.e. the skewed distribution of ejection radius] suggest that they are predominantly disk or bulge stars being expelled from the central regions.

In Figure 7.6 we show the relationship between the last crossing position of objects and their likelihoods. The grayscale density is a logarithmically weighted density plot of the last crossing positions of all the stars in our sample. The colored contours show the $2\sigma$ areas of crossing for the objects as a function of their likelihood. The color scheme of these contours is the same as in Figures 7.4 and 7.5 [natural stars are pink, outliers are black]. From this figure we can see how the outliers tend to be traveling outward from the central regions of the Galaxy; while natural stars tend to be traveling along the local rotation vector.

#### 7.3.1.1 A Case Against a Temperature Based Systematic Bias

The trend for likelihoods to differ with temperature could be an indication of an underlying bias in some of our calculations. More specifically, there is a worry that our distance estimates are systematically too high or too low for certain spectral types. To investigate this, in Figure 7.7 we plot calculated cylindrical velocities, proper motions, radial velocities and calculated likelihoods as a function of distance from the Galactic plane. The data are split into two groups: stars with temperatures below 5000 K, and stars with temperatures above 5700 K.

We find that at all distances from the plane, the rotational velocity, $v_\phi$, is consistent between the two populations with the early type stars having slightly larger spreads in their velocities. This implies that neither stellar group is being over or under estimated in distance with respect to the other. Further, we find that at all distances from the plane, the proper motions are similar in magnitude and dispersion; but the radial velocity estimates for the early type stars are more dispersed. This means that the calculated dispersions in the velocities are an effect of the precise radial velocity measurements and not due to some problem with the proper motion measurements. This radial velocity dispersion difference is manifest in the $v_Z$ measurements, where the early type stars are more dispersed than the late type stars [considering that our survey area consists of two cones directed out of the plane].

It is unexpected that the earlier type stars would have intrinsically larger velocity spreads than later types. Looking at the radial velocity error distributions of the early type and late type stars, we notice that the early type stars have generally larger errors than late type stars [2.4 km $s^{-1}$ as opposed to 1.4 km $s^{-1}$]. This is perturbing as it suggests that the trends in Figures 7.5 and 7.6 may merely be a side effect of erroneous measurements. We investigate this further by performing Monte Carlo error expansions on several randomly selected stars, varying the magnitude of the radial velocity uncertainties. It turns out that larger radial velocity errors end up increasing a star's 95% likelihood; so the lower likelihood of the earlier type stars is most likely an intrinsic property rather than a side effect of the measurement errors. We discuss possible causes of this trend in the Discussion.

### 7.3.2 Hypervelocity Stars

We identify hypervelocity stars as stars whose current kinetic energy is greater than the gravitational potential [described in Section 7.1.2] at their position. This selection allows for a changing selection

threshold as a function of Galactic position and thus is more inclusive and correct than a constant velocity cut.

We construct a catalog of objects which satisfy this criterion and present a subset of them in Table 7.2. This subset is the group of escape velocity objects which also meet the following criteria:

1) their SDSS proper motions differ from PPMXL (Roeser et al., 2010) proper motions by less than 12 mas $yr^{-1}$,

2) their absolute SDSS proper motions are less than 30 mas $yr^{-1}$,

3) their nearest observational [in projection] neighbor is more than 10 arcseconds away,

4) their SDSS proper motion errors are less than 5 mas $yr^{-1}$.

This choice of criteria is explained in the Part III. Seven stars pass all of these quality cuts and 35 fail just one of these tests. The full sample of objects collected is presented in the Appendix along with how many flags each object raised. In the Appendix table, we rediscover seven of the thirteen candidates of Palladino et al. (2014); five of their candidates are too metal poor to be included in our study, and one has large proper motion errors which exclude it from our data set [see Table 7.1].

As an alternate test of the validity of our candidates, we refer to some fascinating work done by Silva & Napiwotzki (2013). They effectively traced the positions of the Milky Way's spiral arm structures by tracing O and B type hypervelocity star orbits backwards in time. This takes advantage of the fact that both the binary and dynamical ejection mechanisms will occur more frequently within the crowded spiral arm structures. In Figure 7.8 we present a similar analysis with our sample of objects.

Figure 7.8 is a map of the bar [shown as a 3.1 kpc long feature inclined at 32° from the sun, as in Vallée 2008] and spiral arm structure of the Milky Way. The logarithmic spiral arms are described by the equations:

$$X = -Rsin(\theta),\ Y = Rcos(\theta),\ R = R_0 e^{k\psi}, \tag{7.4}$$

$$k = tan(p),\ \psi = \theta - [0°, -90°, -180°, -270°] + \phi, \tag{7.5}$$

where $p$ is the pitch angle of the arms, $\phi$ is the phase angle offset of the arms and $R_0$ is a characteristic radius. The four possible angles for the value of $\psi$ correspond to the four spiral arms of the Milky Way. In our case: $p = 12.8°$, $\phi = -53.1°$ and $R_0 = 2.1$ kpc. These values were originally derived by Vallée (2008) for a Solar radius of 7.6 kpc, but Silva & Napiwotzki (2013) corrected them for a Solar radius of 8 kpc and presented them in their paper.

However, this is not the full picture. The spiral arm structure is rotating in time as well with a characteristic pattern speed $\Omega = 20.3$ km $s^{-1}$ $kpc^{-1}$. So when we see an object which has traveled for some time, its intersection point will be shifted with respect to Galactic structure. To rectify this, we rotate all the intersection points forward by the pattern speed multiplied by the time in travel. The intersection points with respect to the spiral structure at the time of ejection are shown with the cyan stars and connected to their actual intersection points by the pink vectors.

Two of our objects appear consistent with possible spiral arm ejections [considering errors], one intersects the Galactic plane so far away that it is doubtful it interacted with any major Galactic structures, and one intersects between spiral arms. The average ejection velocity of the three Galactic objects,

with the Galactic rotation considered, is 669.5 km $s^{-1}$. This is on the high end of the scale of predicted ejection velocities from the dynamic and binary ejection mechanisms, but is not unheard of; see, for example, Gvaramadze (2009). It's also worth noting that simulations of stars ejected via these methods predict maximal velocities of $\sim$ 500 km $s^{-1}$, but these simulations consider only O and B type stars, which are three or more times as massive as our heaviest objects; the simulations show that the average, and maximal achievable velocities are inversely correlated with the mass of the ejected star.

We also wish to investigate the stars which did not cross the Galactic plane in their orbit integrations. These are perhaps the most mysterious stars because of the high metallicities of our sample; these high metallicities make it unlikely that these objects are merely halo contamination. Tracing their orbits back in time could provide insight into other systems capable of producing hypervelocity stars and constrain high velocity ejection mechanisms. In Figure 7.9 we show Monte Carlo orbit realizations for these stars along with nearby globular clusters from the catalog of Harris (1996), 2010 revision.

While we do not have full phase velocity for all of these globular clusters, we can estimate errors on their spatial positions relative to the Monte Carlo orbit expansions. To do so we collect proper motions for a sample of globular clusters [five from Dinescu et al. (1997), ten from Dinescu et al. (1999), seven from Dinescu et al. (2003), six from Casetti-Dinescu et al. (2007), nine from Casetti-Dinescu et al. (2010), three from Casetti-Dinescu et al. (2013), and 19 from the literature compilation of Dinescu et al. (1999)] and find their total space velocity by comparison with radial velocities presented in the catalog of Harris (1996) [2010 revision]. For this sample of 59 clusters, we find an average estimated phase space velocity of 120 km $s^{-1}$. Then, considering that the average flight time until 'intersection' with the clusters in Figure 7.9 is about 17 Myr, we can say that these clusters will have, on average, moved 2.1 kpc. This is the basis of the error bars in Figure 7.9.

One object, J024605.10+312254.29, has several orbit realizations consistent with origin in NGC 1904, although it is unlikely that an object with a metallicity of -0.27 dex would originate in a cluster with a metallicity of -1.6 dex. These unbound, infalling, high metallicity objects are some of the most perplexing findings in this study and warrant further investigation.

TABLE 7.2: Hypervelocity Candidates

| IAU Name | $\Delta$ P.M. mas yr$^{-1}$ | Nearest Neighbor arcseconds | Total P.M mas yr$^{-1}$ | $\sigma$ P.M. mas yr$^{-1}$ | [Fe/H] dex | $V_{Total}$ km s$^{-1}$ | $V_{esc}$ km s$^{-1}$ | Infalling |
|---|---|---|---|---|---|---|---|---|
| J082015.88+362223.26 | 9.05 | 24.2 | 24.27 | 4.7 | -0.73 | 612.13 | 523.83 | X |
| J160707.30+372350.97 | 9.13 | 19.8 | 15.83 | 4.36 | -0.11 | 580.49 | 548.79 | |
| J131238.82+393312.13 | 8.57 | 11.13 | 22.96 | 4.75 | -0.63 | 577.19 | 531.07 | |
| J175010.68+262448.38 | 4.72 | 13.32 | 20.9 | 4.47 | -0.52 | 606.88 | 577.02 | |
| J075516.37+662909.15 | 9.25 | 16.57 | 8.95 | 4.94 | -0.72 | 565.12 | 506.21 | X |
| J024605.10+312254.29 | 4.04 | 16.22 | 11.0 | 4.94 | -0.27 | 546.29 | 518.32 | X |
| J093103.04+134728.81 | 5.63 | 12.95 | 9.1 | 4.55 | -0.51 | 531.91 | 509.41 | |

TABLE 7.3: Objects whose kinetic energy is greater than the gravitational potential at their given position. This table is truncated to retain only the candidates that pass our strict proper motion quality cuts – the full table [including objects which fail the criteria presented in the text] is available in the Appendix. Note that three of our candidates appear to be of extragalactic origin.

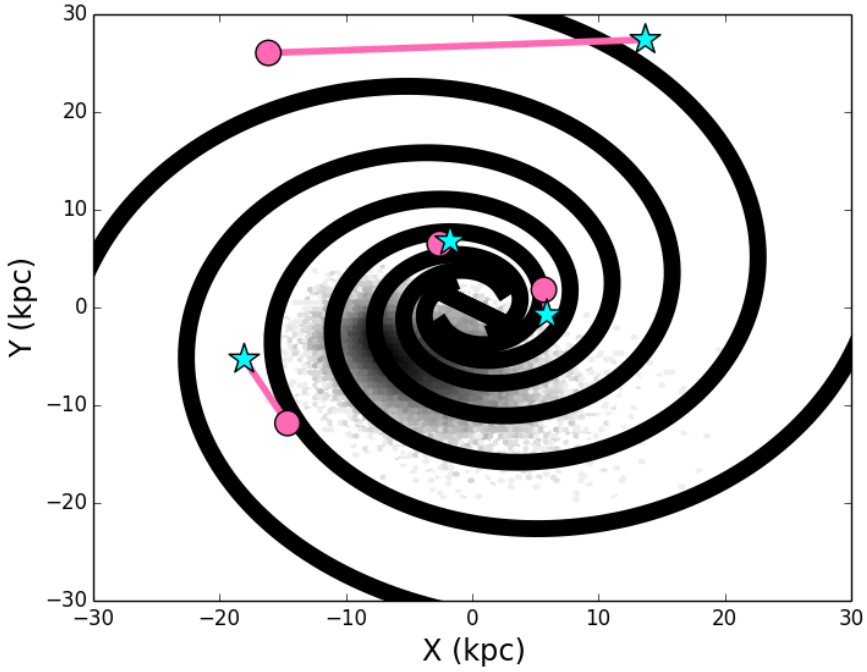


FIGURE 7.8: The positions of last intersection with the Galactic plane for our hypervelocity candidates which intersect the Galactic plane. The grayscale density indicates the locations of last crossing for our entire data set. The current positions of the central bar and the spiral arms of the Milky Way are shown in black with a thickness about equal to 2 kpc. The pink circles are the intersection points of the hypervelocity candidates; they are linked via pink vectors to their intersection points with respect to the spiral arm structure at the time of ejection [cyan stars]. Two of these objects are consistent with having been ejected from the spiral arm features of the Milky Way.

### 7.3.3 Hills Stars

Finally we investigate objects which may have been ejected by interactions with the central supermassive black hole [SMBH; Hills 1988]. There are many exciting questions that can be answered by investigating possible Hills stars.

One is the postulation that the central supermassive black hole may in fact be a binary system – if one is able to observationally locate an ejected, undisrupted stellar binary system, it would be a "smoking gun" indication that there are two black holes orbiting each other in the center of our Galaxy (Lu et al., 2007), and is one of the best indications of such a phenomenon without gravitational wave experiments.

Another is the interesting discovery that hypervelocity stars have a non-isotropic distribution (Brown et al., 2012). It has been suggested by Lu et al. (2010) that the locations of these ejected stars are related to the planar structures that they existed in before ejection and, as a consequence, they should not be distributed isotropically.

In the Galactic center, it has been shown by Paumard et al. (2006) that some disks of material falling to the supermassive black hole host star formation [specifically a ClockWise System and a CounterClockWise System; (CWS, CCWS)] and that these disks are rich in a top-heavy stellar population. Stars from these systems are ejected preferentially in paths parallel with their birth planes. Other systems,

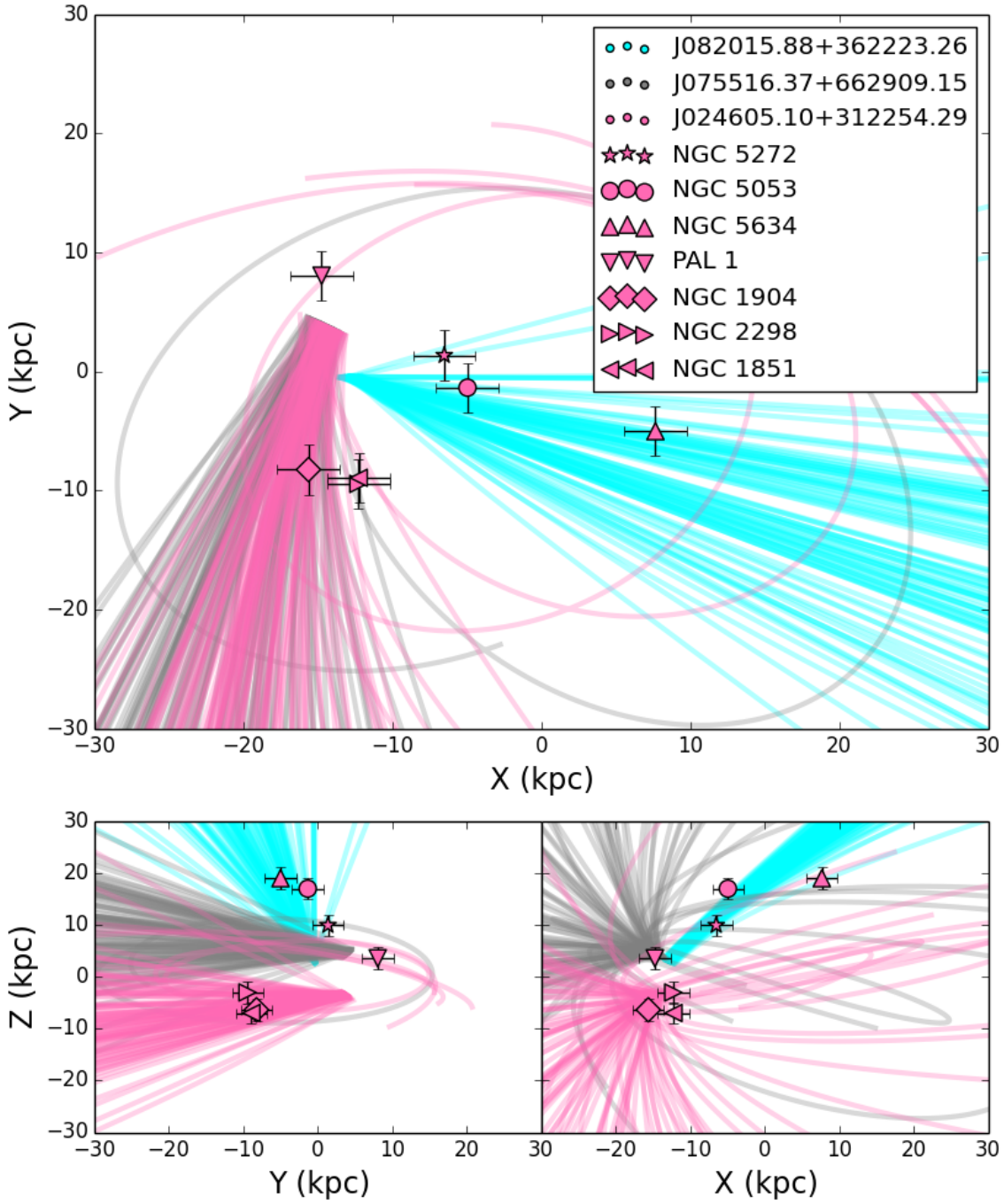


FIGURE 7.9: Monte Carlo orbit expansions of three unbound, infalling, high metallicity stars. Also plotted are globular clusters which have positions within 5 kpc of the nominal orbits of the objects. The object J024605.10+312254.29 [pink] has an orbit coincident with the position of the globular cluster NGC 1904; however the star and the cluster differ in metallicity by 1.33 dex which is mysterious. The other objects are not strongly associated with any known globular clusters. The error bars indicate the average movement range of a globular cluster in the flight timescales considered here [17 Myr].

such as the Northern Arm and Bar of the minispiral and the CircumNuclear Disk [NArm, Bar, CND] also exist and star formation in these features could also eject young stars in planar distributions.

Previously studied O and B Hills stars, which are necessarily young objects, are most likely to be found in planar orientations since they were probably born in these infalling structures shortly before ejection. Older populations in the Galactic center probably fall into the nuclear region along random vectors owing to the chaotic nature of the surrounding bulge. And some stars born in the above mentioned structures may also be scattered into random orbits if they survive long enough. This is observationally confirmed by Figer et al. (2003).

The general picture of the nuclear regions is then a highly ordered and coherently rotating young stellar population and an isotropically distributed old population. If we see objects being ejected from the Galactic center, we would expect them to be a mixture of planar orientation and random distribution since our F-to-M type stars can cover a wide spread of ages.

In Table 7.4 we present our collection of objects leaving the central 0.25 kpc [radius] of the Galaxy at high velocities [more than 500 km $s^{-1}$] and their properties. The ejection radius and velocity are determined by integrating the orbits of all our stars back in time and analyzing their first disk crossing; to account for uncertainties in the orbit calculations, we look at objects going through the central 0.25 kpc rather than only investigating stars intersecting the very center. The ejection velocity is then corrected for the rotation curve of the Milky Way to find the intrinsic properties of the ejection event.

In Figure 7.10, we compare the object locations with the planes presented in Paumard et al. (2006). This plot is a Galactocentric longitude and latitude plot with the sun located at 180° in longitude: this choice of coordinate system makes spatial orientation correlations with Galactocentric features more obvious than they would be in a heliocentric system. In this figure, we also plot the spatial locations of the hypervelocity stars presented in Brown et al. (2012) as well as the recently discovered hypervelocity star of Zheng et al. (2014). As has been noticed before, the O and B type hypervelocity stars in general lie near to the planes occupied by the CWS, NArm and CCWS. Unfortunately we cannot comment on the existence of our objects along these planes as our survey footprint [shown in black in the figure] is too shallow to effectively sample them. However, we can see overdensities of our main sequence objects along the planes of the CND and Bar structures. About half of our objects lie directly on these planes, which is perfectly consistent with the idea that our objects should arise from both planar ejections [for the young ones] and isotropically distributed ejections [for the old ones]. This is further supported by the temperature distributions of the stars: the hottest objects are clustered about the plane of the bar of the minispiral.

Follow up observations of these objects, combined with existing observations of the known Hills stars, could lead to valuable insight into the shrouded populations of the innermost regions of the Galaxy. High resolution spectroscopic observations of the stars considered in tandem with existing samples of O and B type Hills stars could also potentially provide insights into the chemical abundances of the various nuclear structures. Furthermore, as mentioned above, if we could discover an ejected, coherent binary system this would provide groundbreaking evidence for the existence of a binary black hole at the center of the Milky Way (Lu et al., 2007).

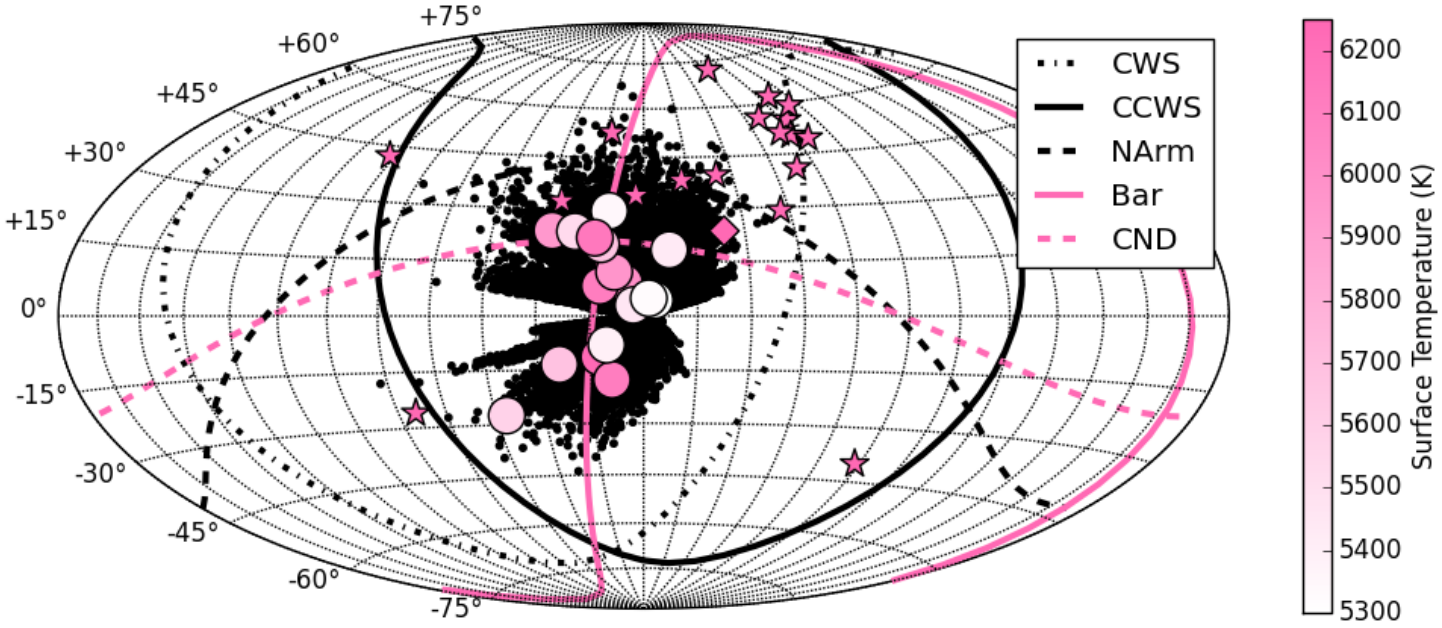


FIGURE 7.10: Galactocentric Hammer projection of Hills stars with the Sun at 180°. The pink stars are Hills stars presented in Brown et al. (2012) and the pink diamond is the Hills star recently discovered by Zheng et al. (2014)– these objects are all O and B type Hills stars, and thus are most likely associated with the star forming planes of matter in the Galactic center. The circles are our discovered Hills candidates superimposed on our study's footprint in black. Their colors indicate their atmospheric temperatures. The color range is truncated to improve contrast, one star at [183,4] has a temperature of 4300 K. The lines indicate the orientation of various planes of matter in the Galactic Nucleus as described in Paumard et al. (2006). It is expected that young Hills stars will be formed and ejected along these planes while old Hills stars will be ejected in a more isotropic fashion. The black curves indicate planes previously associated with Hills stars. The pink curves are planes we tentatively associate with our candidates.

TABLE 7.4: Hills Candidates

| Item | IAU Name | $\Delta$ P.M. mas yr$^{-1}$ | Nearest Neighbor arcseconds | Total P.M. mas yr$^{-1}$ | $\sigma$ P.M. mas yr$^{-1}$ | [Fe/H] dex | Ejection Velocity km s$^{-1}$ | Ejection Radius kpc |
|---|---|---|---|---|---|---|---|---|
| 1 | J135855.65+552538.19 | 4.42 | 13.33 | 60.24 | 3.78 | -0.78 | 665.32 | 0.12 |
| 2 | J165150.71+242750.95 | 3.26 | 7.33 | 56.55 | 3.76 | -0.64 | 504.31 | 0.25 |
| 3 | J113946.33-033651.63 | 1.61 | 12.62 | 68.38 | 3.62 | -0.5 | 533.82 | 0.1 |
| 4 | J231445.85+135233.36 | 1.12 | >30.0 | 11.62 | 3.8 | -0.77 | 527.57 | 0.21 |
| 5 | J000212.11-033306.82 | 3.62 | 17.05 | 13.6 | 3.57 | -0.71 | 544.34 | 0.11 |
| 6 | J072614.12+321948.36 | 7.52 | 9.23 | 20.77 | 4.36 | -0.71 | 526.29 | 0.22 |
| 7 | J172757.94+433922.89 | 1.47 | 22.09 | 9.59 | 3.45 | -0.76 | 504.31 | 0.15 |
| 8 | J165055.60+342437.61 | 5.47 | 11.07 | 9.23 | 4.61 | -0.75 | 508.26 | 0.19 |
| 9 | J000216.44+251544.66 | 4.72 | 7.39 | 9.18 | 3.96 | -0.78 | 506.64 | 0.19 |
| 10 | J142648.59+563316.32 | 8.85 | 13.98 | 19.82 | 3.9 | -0.61 | 554.42 | 0.1 |
| 11 | J160529.79+033633.63 | 7.72 | 16.75 | 14.15 | 5.16 | -0.62 | 500.96 | 0.16 |
| 12 | J144327.11+484517.71 | 7.34 | 10.43 | 9.89 | 4.43 | -0.52 | 508.14 | 0.15 |
| 13 | J160837.58+380935.80 | 6.14 | 10.39 | 6.99 | 4.48 | -0.69 | 551.08 | 0.08 |
| 14 | J152600.56+395522.46 | 4.88 | 22.34 | 10.03 | 3.98 | -0.59 | 503.59 | 0.12 |
| 15 | J204157.65-053051.05 | 4.76 | 10.05 | 3.84 | 4.9 | -0.44 | 515.07 | 0.2 |
| 16 | J131251.01-004654.75 | 4.24 | 6.53 | 19.69 | 4.91 | -0.75 | 512.95 | 0.2 |
| 17 | J001557.27+341047.79 | 3.52 | 13.28 | 7.09 | 5.09 | -0.39 | 552.45 | 0.16 |

TABLE 7.5: Our collection of objects leaving the central quarter kpc of the Galaxy [radius] at more than 500 km s$^{-1}$. The columns $\Delta$ P.M. [the difference in the SDSS and PPMXL proper motion estimates], distance to the nearest neighbor [in projection], total proper motion and proper motion error are provided to gauge the reliability of the measurements [see Chapter 10]. The last two columns are the velocity of ejection and the distance from the Galactic center.

# Chapter 8

# Discussion for Part II

We have collected a sample of high metallicity [> -0.8 dex] main sequence F-to-M type stars. Using six dimensional phase space information for these objects we constructed probability density functions describing the bulk motion as a function of height from the Galactic plane. These probability density functions were then used to identify kinematic outliers.

We found that outliers are generally faster moving, more metal-poor and of earlier stellar type than natural stars. Outliers also tend to show a preference for originating closer to the Galactic center than the natural stars. This implies that the outlier stars are poorly described by a halo population, since halo contamination would be spatially isotropic. Of our 5% least likely objects, for example, 58% have positive radial velocities with respect to the Galactic center [and 61% of our 1% least likely]. Our metallicity cut should also minimize the contribution of halo stars to our sample. This is consistent with findings of Ness et al. (2013), who find that the bulge component with a metallicity of -1.0 < Fe/H < -0.5 is kinematically hotter than the higher metallicity components.

It is interesting that the earlier type stars are kinematically hotter than the later type stars. One explanation for these trends could be that the binary fraction is higher for earlier type stars. Kouwenhoven et al. (2009) notes from a literature compilation that F to G type dwarfs have multiplicities of 55%-60% while M dwarfs have multiplicities of 30%-40% and late M types and brown dwarf binary fractions can be as low as 10%-30%. This higher binary fraction enables more dynamic ejections, as the ejected star usually originates in a binary system. A higher existent binary fraction could also explain the generally more dispersed velocity components seen in Figure 7.7, as the binary orbit velocity components would add to the system's velocity components.

We have also collected a sample of hypervelocity stars calculated to be traveling faster than their local escape velocity. After imposing stringent cuts designed to reduce proper motion measurement errors, we integrate their orbits back in time to find their origins. Of our seven strong candidates, two of the four which intersect the Galactic plane are found to intersect the Galactic plane at positions coincident with spiral arm structure [one intersects between spiral arms and one crosses the Galactic plane too distantly to be associated with any known structure]. It is well known that runaway star production is higher in the spiral arms (Silva & Napiwotzki, 2013) due to the greater stellar density. The remaining three hypervelocity stars have orbits that indicate the objects are actually infalling, rather than being ejected from the disk. We perform Monte Carlo error expansions on their orbits to try and uncover possible origins: one object has an orbit which intersects NGC 1904, but the metallicity difference between the star and the globular cluster pose a mystery. Such infalling hypervelocity stars have been noticed recently by Palladino et al. (2014) as well.

Finally we examined a sample of stars leaving the central 250 pc at 500 km $s^{-1}$ or greater. These stars may have interacted with the central supermassive black hole and received large kicks from that interaction (Hills, 1988). Hills stars may come to encounter the central supermassive black hole via two paths: younger stars may be formed on gaseous disks in the nuclear region; and older stars may fall in from outside the nuclear region isotropically. We cannot confirm that our Hills stars are consistent with the planes previously associated with O and B type Hills stars as our footprint does not reach those planes. However, we find that approximately half of our candidates fall on the planes of the bar of the minispiral and the circumnuclear disk, while the other half have a more isotropic distribution. Interestingly, the hottest stars are aligned with the plane of the bar of the minispiral, while the cooler stars are more homogeneously distributed. This would be consistent with a mixed origin theory. It is also possible that some of these objects are accelerated to high speeds via binary or dynamic interaction mechanisms – this is especially true if, as some people postulate, there is a large population of solar mass black holes in the nuclear regions (Miralda-Escudé & Gould, 2000).

In the future, we would like to revisit a few aspects of this Part. The most obvious opportunity for improvement is to redo the analysis presented in Section 7.3.3 without the high metallicity cut we imposed on our entire data set. This metallicity cut is irrelevant to those findings, but it was maintained for consistency with the other sections. We could also redo section 7.3.2 without the metallicity cut, but then we would need to take extreme care to consider possible halo contaminants.

Other possibilities include applying the same analysis to different surveys. The RAVE database for example comes with radial velocities and distance estimates for all of its objects; by combining these data with an appropriate proper motion database, essentially the same analysis could be performed. Another possibility is to use Pan-STARRS photometry and proper motions in combination with LAMOST spectra. This would open up an entirely new area of the sky as well, since LAMOST is focussing its survey on the anticenter features and Pan-STARRS observes that area as well – while the SDSS observes the area only sparingly.

This area of research has a lot of potential and seems to be little explored. Exploring structures through their after-affects instead of via direct observation is a tricky, yet intriguing idea.

# Part III

# An Examination of Proper Motions

*"But I don't want to go among mad people," Alice remarked.*
*"Oh, you can't help that," said the Cat: "we're all mad here. I'm mad. You're mad."*
*"How do you know I'm mad?" said Alice.*
*"You must be," said the Cat, "or you wouldn't have come here."*

- Lewis Carroll, *Alice in Wonderland*

# Chapter 9

# Introduction to Part III

When studying structures and dynamical systems, it's important to consider not only the data, but the meta-data as well. After all, structures and trends can easily turn out to be byproducts of something completely unexpected, like systematic errors in your data. Thus it is important to always look at the data as a whole and to understand the errors contributing to your data.

In Part II it was alluded to that the proper motion measurements were the least precise portion of our data and that special care needed to be taken to use them correctly. Errors in the proper motion measurements are the most likely cause of misidentified hypervelocity stars and Hills ejecta. While the typical SDSS radial velocity errors are less than 15 km $s^{-1}$ for all of our objects (Yanny et al., 2009), a proper motion error of 3 mas $yr^{-1}$ is about 15 km $s^{-1}$ $kpc^{-1}$. Therefore it is crucial that we understand the accuracy and reliability of various proper motion catalogs.

This Part is split into two main Chapters. In Chapter 10, we investigate the accuracy of the proper motions we used in Part II by comparing several different proper motion surveys and we come up with some quality flags which were mentioned in Section 7.3.2 that may be used to separate out likely erroneous proper motions. During this exercise, it was noted that the PPMXL proper motion catalog has a systematic offset from the SDSS proper motion catalog, we discuss this is Chapter 11.

# Chapter 10

# Accuracy Check of SDSS Proper Motions

In Part II, we mentioned a set of cuts which we used to separate 'good' and 'bad' proper motion measurements by. Here we briefly go over how we decided on such metrics and how reliable you can expect the proper motion measurements to be in the SDSS.

As mentioned, the proper motion accuracies are one of the most crucial aspects of any six dimensional phase space study. Thus we wish to devote an amount of time to analyzing the accuracy of the proper motions of the SDSS proper motion catalog. In stripe 82 we have four overlapping proper motion studies [Munn et al. (2004), Roeser et al. (2010), Bramich et al. (2008), Koposov et al. (2013)]. To review: the catalog of Munn et al. (2004) is created by comparing USNO-B plate reductions and SDSS photometry; the catalog of Roeser et al. (2010) is created by comparing USNO-B and 2MASS astrometry; and the catalogs of Bramich et al. (2008) and Koposov et al. (2013) are created by looking only at SDSS data which has been reobserved several times in stripe 82. In the full SDSS footprint we have four observable metrics which may be used as proxies for the accuracy of the proper motions.

Here, we compare the proper motion estimates of the four proper motion catalogs in a crossmatched data set with the following 'four metrics:'

- The total difference between the SDSS proper motions of Munn et al. (2004) and the PPMXL proper motions of Roeser et al. (2010): $\Delta$ (Munn, Roeser),
- The total pipeline proper motions of the SDSS: |P.M. (Munn)|,
- The distance on the sky to the nearest SDSS detection: Nearest Neighbor (”),
- The pipeline reported error on the proper motions of the Munn et al. (2004) catalog: |P.M. Error (Munn)|.

We use these metrics to define a series of quality cuts which may be used to isolate only the most accurate of the measurements.

Our first test of accuracy is the 'clustering' of the four measurements:

$$c = \sqrt{\sigma(P.M._{\alpha})^2 + \sigma(P.M._{\delta})^2}.$$

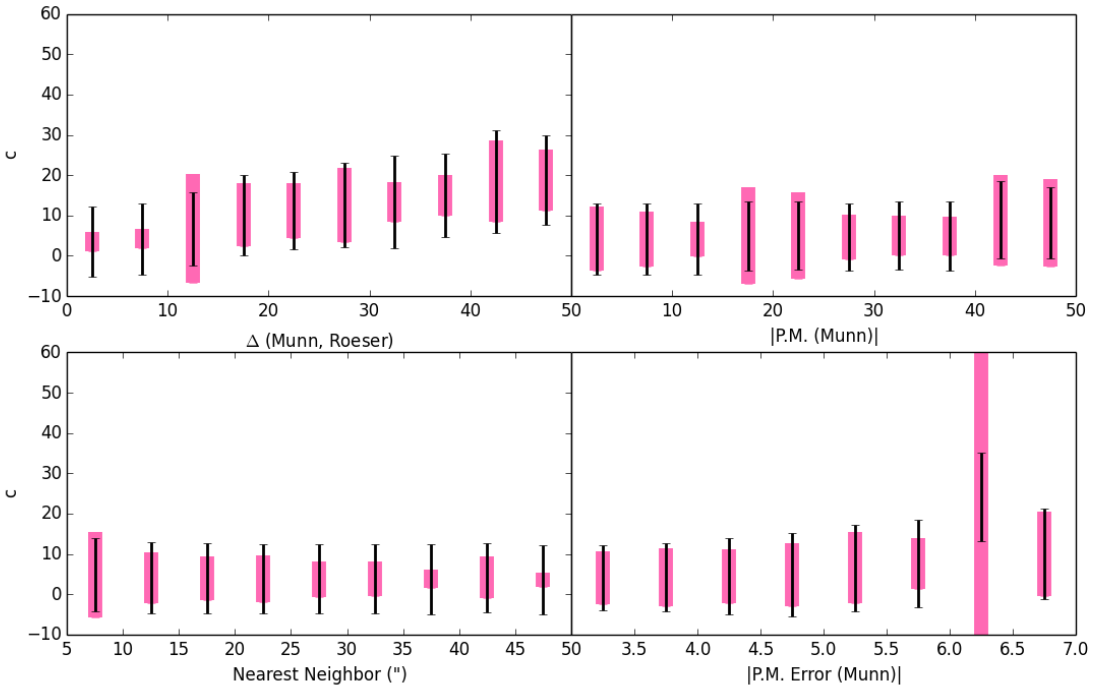


FIGURE 10.1: Average clustering as a function of the four 'quality metrics.' In pink we show the one sigma dispersion in c [the 'clustering' of proper motion measurements in different surveys, described in the text; small c indicates good agreement between various proper motion studies]. In black, we show additional error bars centered on the average value of the clustering, c. These error bars' extents are the average value of the catalogs' errors [added in quadrature] for each bin. We see that the clustering grows gradually worse as the disagreement between the catalogs of Munn et al. (2004) and Roeser et al. (2010) increases. No significant trend is apparent as a function of total proper motion, although larger reported errors do indicate larger spreads in the clustering. As expected, there is better agreement for all of the proper motion catalogs in less crowded areas.

In Figure 10.1 we plot the clustering c as a function of the four 'quality metrics'. We find that the four proper motions are in best agreement when the PPMXL and SDSS proper motions are similar, when the reported errors are small, and the field is relatively uncrowded.

As another test, in Figure 10.2 we check the difference between the highly precise catalog of Koposov et al. (2013) and the SDSS pipeline catalog. The catalog of Koposov et al. (2013) is a wholly internal catalog, using only SDSS photometry, so it avoids systematic mismatching biases caused by crossmatching catalogs. Many proper motion catalogs, such as those of Munn et al. (2004) and Roeser et al. (2010), are matched to photographic plate surveys to achieve long time baselines, at the cost of possible source mismatching. This two catalog check will lessen the possibility of 'clustering inflation' caused by intrinsic catalog mismatches in the prior test. Again we see that large proper motion errors indicate noisier agreement, and that the best agreement is in uncrowded fields.

In light of Figure 10.1 and Figure 10.2, we suggest the constraints presented in Table 10.1 for the selection of high quality proper motion measurements. We use these cuts to select candidate hypervelocity stars in Section 7.3.2.

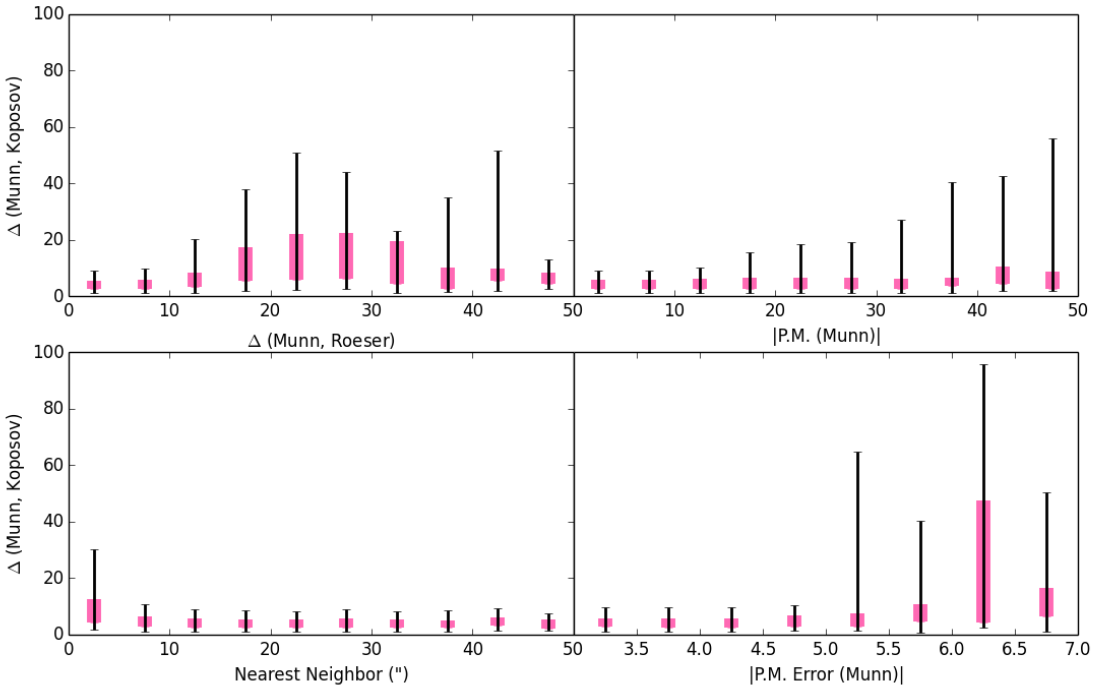


FIGURE 10.2: Difference in proper motions for objects in the proper motion catalogs of Koposov et al. (2013) and Munn et al. (2004). The pink and black bars indicate the interquartile and 95% confidence ranges, respectively. Visible in this figure is a definite trend for agreement to become more erratic as a function of Roeser et al. (2010) and Munn et al. (2004) catalog disagreement and the total proper motion reported by Munn et al. (2004). There is also good agreement for measurements in uncrowded fields and in measurements with low reported errors.

Having investigated the accuracy of the proper motions, we now investigate the accuracy of the proper motion errors. This is a critical aspect as it heavily affects the outcomes of our Monte Carlo expansions. To do this we again compare the catalogs of Koposov et al. (2013) and Munn et al. (2004). In Figure 10.3 we plot the observed difference in stellar proper motions along with the expected differences from the reported errors of both catalogs. As a secondary test, also in Figure 10.3, we plot the motions of spectroscopically identified quasars in the catalog of Munn et al. (2004) along with their expected motions as a result of the errors on their proper motion estimates.

For the quasars, we see that the proper motions predicted by the formal proper motion uncertainties are marginally larger than the observed ones, implying that Munn's errors may be slightly overestimated. In the comparison of proper motions between the two catalogs we see, in general, a reasonably good agreement between the observed and predicted distributions. The observed difference is slightly larger than the formal uncertainties would suggest, but this is not a strong effect. The small tail in this plot is likely an effect of mismatching the objects between the catalogs and, in conclusion, we believe that the errors reported in the Munn et al. (2004) catalog are reliable.

| Constraint | Δ (Munn, Koposov) mas yr$^{-1}$ | c mas yr$^{-1}$ |
|---|---|---|
| \|SDSS P.M. - PPMXL P.M.\| < 12 | 4.5 | 4.0 |
| \|SDSS P.M. - PPMXL P.M.\| > 12 | 14.6 | 21.5 |
| \| SDSS P.M. \| < 30 | 4.7 | 4.5 |
| \| SDSS P.M. \| > 30 | 18.8 | 11.7 |
| Nearest Neighbor > 10" | 4.3 | 4.1 |
| Nearest Neighbor < 10" | 6.6 | 5.9 |
| SDSS P.M Error < 5 | 4.7 | 4.5 |
| SDSS P.M Error > 5 | 16.4 | 13.1 |

TABLE 10.1: The average difference between the proper motion estimates of Koposov et al. (2013) and the SDSS pipeline for cuts on certain constraints. The average clustering, c [described in the text], is also shown. The cuts here are chosen by inspection of Figures 10.1 and 10.2.

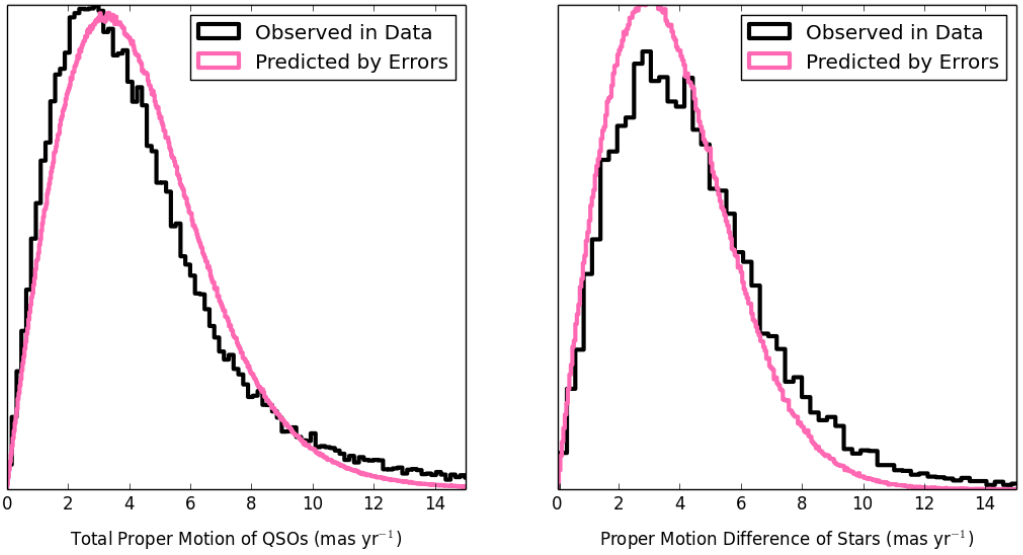


FIGURE 10.3: Left: comparison of the observed proper motions of quasars in the proper motion catalog of Munn et al. (2004) [black] and the proper motions predicted by errors [pink]. Since QSOs should be essentially stationary on the sky, their measured motion is solely due to observational uncertainties. We note that the predicted motion from errors is in general larger than the observed motion, which implies that the errors are being accurately reported or even overestimated.
Right: A comparison of the difference of proper motions in the Koposov et al. (2013) and Munn et al. (2004) catalogs [black] along the proper motion differences predicted by the errors of the two catalogs [pink]. In general there is good agreement; there is a slightly heavy tail in the observed differences, this is most likely an effect of mismatching between the two catalogs.

# Chapter 11

# Proper Motions in PPMXL

## 11.1 Introduction

During the course of the analysis of proper motions presented in Chapter 10 a disturbing trend was noticed in the relationship between the SDSS and PPMXL proper motions. Namely that there was a systematic offset between the proper motion estimates for all the stars in our study. This is shown in Figure 11.1.

The PPMXL proper motion catalog (Roeser et al., 2010) is a database of ∼900 million proper motion estimates calibrated to the ICRS. The catalog was created by combining USNO-B1.0 catalog astrometry with 2MASS astrometry and bringing that relative astrometry into the ICRS by comparison with the *Hipparcos* catalog, which is the primary ICRS reference catalog.

In this Chapter, we construct a post-processing corrective script which can be used to correct for this offset in small data sets. We also add two additional columns to the PPMXL database which have been post processed by our method. In Section 11.2, we select a sample of extragalactic objects across the whole sky using a combination of WISE photometry and 2MASS photometry. In Section 11.3, we fit spherical surfaces to the PPMXL proper motions of these objects to find local proper motion offsets from zero; and we then create a corrective volume from these surface fits. In Section 11.4, we subtract this corrective volume from the proper motions of our own extragalactic sample as well as from a set of fundamental ICRS radio sources to examine the residual proper motions of extragalactic objects as a goodness-of-correction metric.

## 11.2 Data

To correct the PPMXL proper motion catalogue, we require a sample of extragalactic objects [which should have intrinsic proper motions of nearly 0 mas $\mathrm{yr}^{-1}$]. We can use the estimated proper motions of this intrinsically stationary sample to estimate underlying biases in the PPMXL catalog. Ideally the sample we use will cover the whole sky [so the entire PPMXL catalog can be corrected] and have as many items as possible [to maximize the robustness of the fit].

At this point we refer to an interesting color selection noted independently by Kovács & Szapudi (2013) and Pradhan et al. (2014). Both groups find that extragalactic and galactic objects separate from each

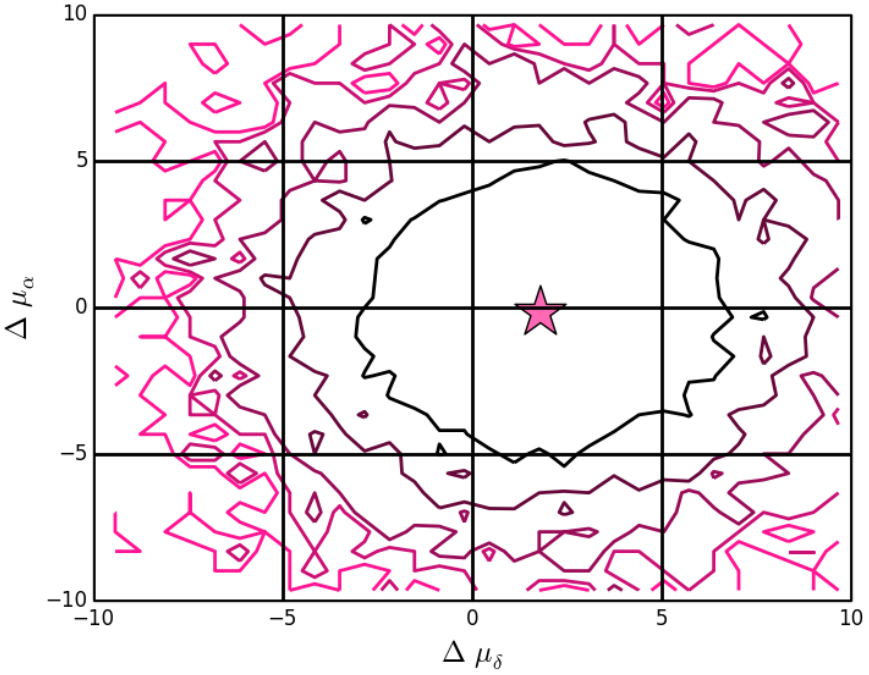


FIGURE 11.1: Difference in the reported proper motions for stars in the SDSS and PPMXL catalogs. The pink star indicates the average difference [about 1.8 for $\mu_\delta$ and 0.2 for $\mu_\alpha$] in the proper motions and the contours represent to one-to-three $\sigma$ distributions. It is obvious that the proper motions of stars are systematically offset in this figure.

other in WISE W1 and 2MASS J color. This is optimal for our purposes as both WISE and 2MASS are all-sky surveys and they probe similar magnitudes.

To investigate how galactic and extragalactic origin relate to J-W1 color, we initially collect a sample of SDSS spectroscopically observed objects. The SDSS has a much sharper photometric resolution [FWHM $r$ ∼1.3"] than WISE [FWHM W1∼6.1"] or 2MASS [FWHM J∼2.9"], so it is ideal for identifying galaxies based on their photometric profiles. The medium resolution spectroscopy [R∼1800] is necessary for separating quasars from stellar objects. This spectroscopic data can thus be split into two groups: galactic [objects with point spread function photometry *and* star-like spectra]; and extragalactic [objects with non-point spread photometry *or* quasar-like spectra] objects.

We then crossmatch these data with the WISE all sky catalog to obtain W1 and 2MASS J colors [2MASS photometry is included in the WISE database.]

In Figure 11.2 we histogram these two groups in J-W1 space– redward of the vertical line at J-W1 = 2.0, is a sample of objects which are ∼99% extragalactic, and blueward of the line at J-W1 = 0.5 is a sample of objects which are ∼99% stellar. For the rest of this chapter, we will use this color cut as a selector for extragalactic objects. The spatial distribution for a subset of these objects is shown in Figure 11.3.

We query the WISE database for data in that color range in seven, 0.1 magnitude wide, 0.5 magnitude separated, J band slices [iee. J = 14.0-14.1, 14.5-14.6 ... 17.0-17.1]. These data are crossmatched with the PPMXL proper motion database as a function of position and J magnitude to collect the proper motion data for these objects.

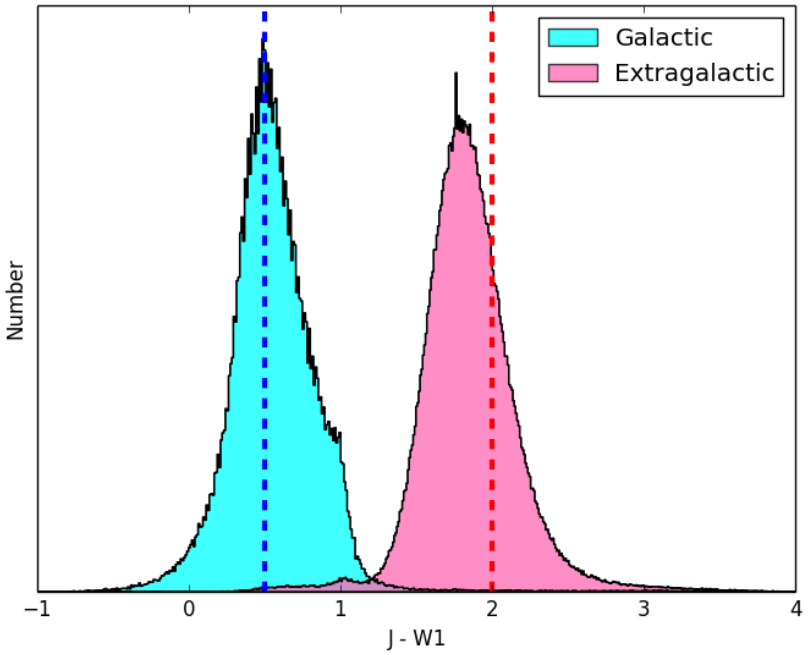


FIGURE 11.2: A color selection for galactic [cyan] vs extragalactic [pink] objects [verified by SDSS spectroscopy] using WISE and 2MASS data. The vertical line at J-W1 = 2.0 indicates the color cut we use to select extragalactic objects; redward of this line, ∼99% of the data are extragalactic sources. The vertical line at J-W1=0.5 is the color cut we use to select stellar objects; blueward of this line, ∼99% of the data are stars. Data selected via these color cuts are plotted spatially in Figure 11.3.

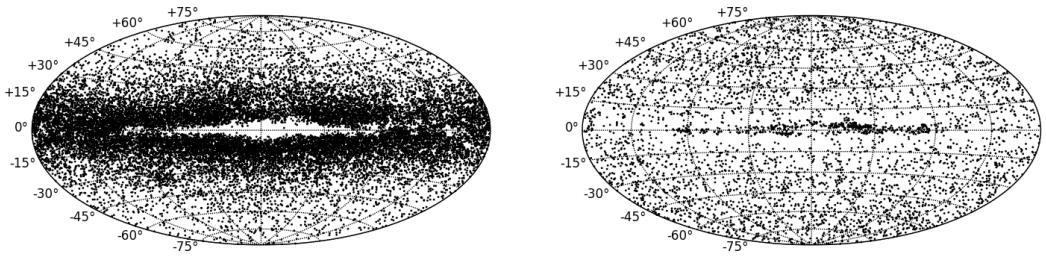

FIGURE 11.3: The distribution of stars [left] and extragalactic objects [right] as selected by the color cut in Figure 11.2. The uniform distribution of the extragalactic objects across the sky as compared to the disk-like distribution of the stars is indicative that the color selection is effective for most of the sky. Extreme reddening at absolute latitudes below 10°, however, is problematic. Note that these figures show a randomly selected one-one-hundredth of the data used in the proper motion fitting shown in Figures 11.4 and 11.5.

This extragalactic data set will be used to construct an all-sky, magnitude dependent correction for the proper motions.

## 11.3 Fitting

Our seven data slices should be almost entirely composed of extragalactic sources – if this is true, then the sources should have zero proper motion in any direction [or rather, the proper motions should be so small that they are indistinguishable from zero]. This is not the case, we find that these objects have a net movement of 0.26 mas $yr^{-1}$ in $\alpha$ and -2.9 mas $yr^{-1}$ in $\delta$.

We wish to fit these proper motions to a combination of spherical harmonics in each data slice. The fit harmonics may then be subtracted from the data to produce a new, recentered PPMXL proper motion catalog.

In each magnitude bin, the first 10 degrees of spherical harmonics are fit to the proper motions of the data [one fit for the proper motion in $\alpha$ and one fit for the proper motion in $\delta$]. So in total we perform 14 fits and each fit has 121 variables [we do not fit inverse harmonics]. Note that, for this fit, we remove spurious proper motion measurements by making a 2 $\sigma$ cut on the proper motions about the mean proper motions in each direction before fitting the spherical harmonics.

The results of this fitting are shown in Figure 11.4 – these surfaces show areas of high and low proper motions in the data. By subtracting this surface from the data, we should essentially re-center these objects on zero proper motion around the celestial sphere. We also fit the motion of stars in a similar manner in Figure 11.5, comparison shows that the detected motions of the extragalactic objects are not side effects of erroneously identified stars since their spatial features are different.

We turn these surfaces into a corrective volume by linearly interpolating between the surfaces. In this way we may correct proper motions for objects which do not lie in the data slices we fit.

## 11.4 Testing the Fits

### 11.4.1 Internal Consistency

We first investigate the success of our methodology in correcting the proper motions of our fitting data set by subtracting the constructed correction volume from the proper motion measurements used to derive it.

Figure 11.6 shows the bulk motions of the data used to construct the correction volume before and after the volume is subtracted from the proper motions. Several trends are noticeable from Figure 11.6.

1. The Galactic plane and center are recognizable in their dispersion signatures – this implies that our color selection is imperfect in these areas.
2. South of $\delta$ $\sim$-45° the bulk proper motions appear more random – this is an artifact of the sources used to calibrate the ICRS catalog which change at this latitude [the observational epoch differences are smaller in this area of the sky].
3. After subtracting the surfaces, bulk motions are smaller and less coherent.

### 11.4.2 Consistency with the ICRS

We further test the correction volume by considering two data sets which are fundamental to the ICRS. The ICRS is defined by a set of compact radio sources which are observed by a set of Very Long Baseline Array [VLBA] observations. In the northern hemisphere [down to a $\delta$ ∼-45°] ∼2200 of these observations are astrometric as well as geodetic; these are the VLBA Calibrator Surveys [VCS]. An additional ∼1200 astrometric only [Non-VCS] sources cover the entire celestial sphere.

We collect these sources and their PPMXL proper motions and perform the same correction as in Section 11.4.1. The average proper motions before and after the correction for our WISE, VCS and non-VCS corrections are shown in Table 11.1. For reference we also show the same values for the SDSS pipeline proper motions for the set of extragalactic objects described in Section 2 and shown in Figure 11.2.

Our correction shows good recentering of the proper motion in $\alpha$ for the WISE data, but little to no improvement for the VCS and non-VCS data. The most noticeable improvement is in the proper motion in $\delta$ – a definite trend toward negative values is recentered to ∼0 mas yr$^{-1}$. In all cases the magnitudes of the total proper motions are lessened.

After this correction, the proper motions of extragalactic sources in PPMXL are similar in magnitude to those of the SDSS proper motion data products.

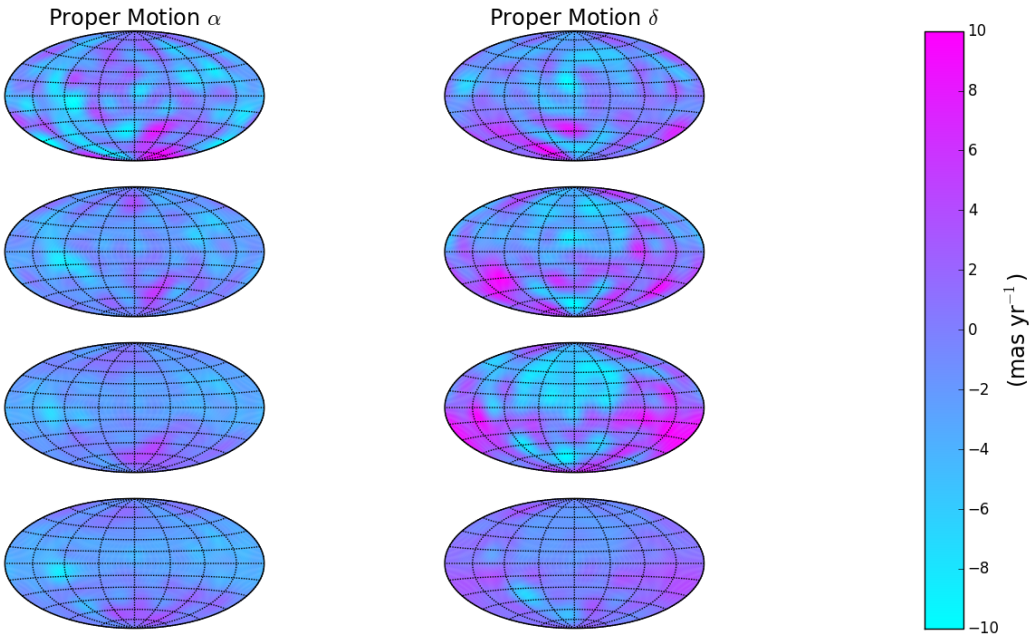


FIGURE 11.4: Spherical harmonic fits for our data in the magnitude bins described in Section 11.3 [the three bins at the half-magnitudes are omitted to save space]. There are clear areas of high proper motion [for example proper motion in $\alpha$ is high around [($\alpha$, $\delta$) = (140, -60)] and we can see that the fits show some variation with the magnitude slice investigated. Proper motions of our extragalactic data set once this corrective volume has been subtracted are shown in Figure 11.6.

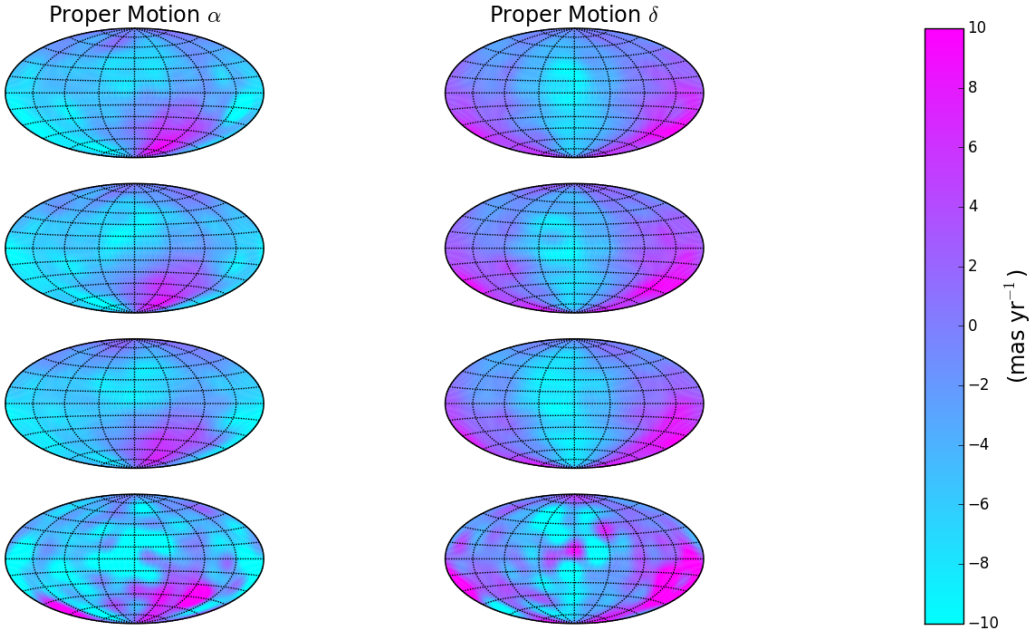


FIGURE 11.5: Similar to Figure 11.4 but instead fit to selected stellar objects. The proper motion profiles of the selected extragalactic objects are different from the proper motions of the stars; further evidence that their movement profiles arise from biases in the PPMXL catalog.

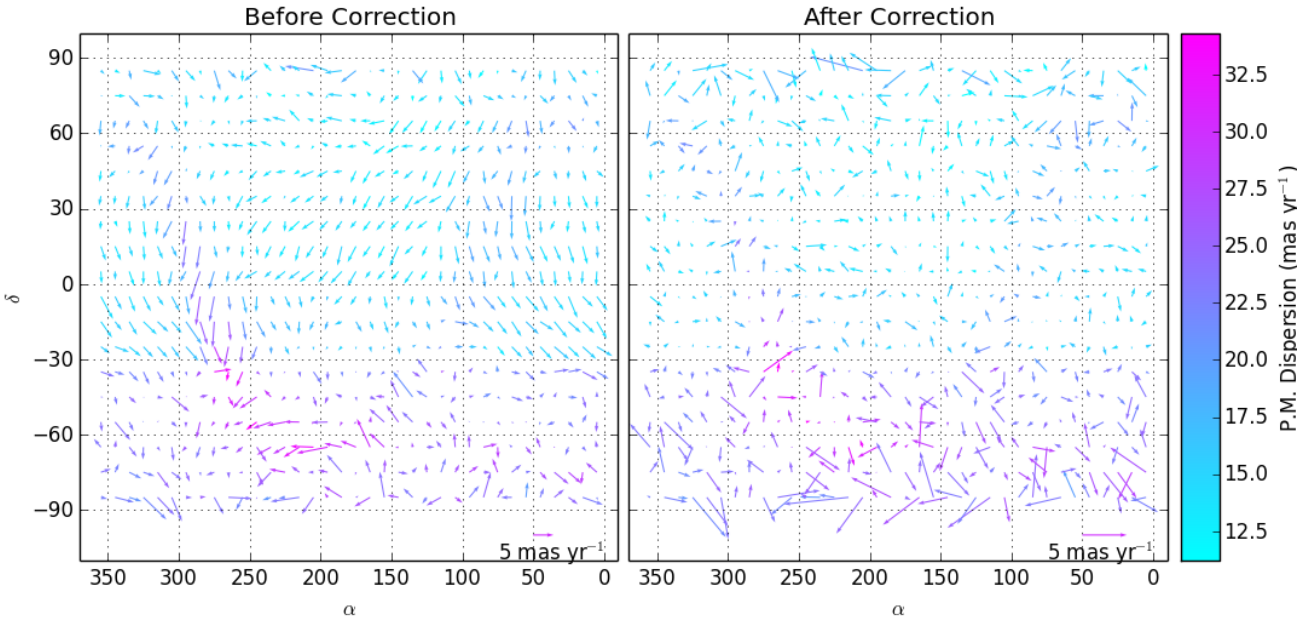


FIGURE 11.6: Bulk proper motions [each arrow indicates a 10°x10° bin] of our extragalactic sources before [left] and after [right] subtracting the surfaces shown in Figure 11.4. The arrows show the on-sky direction of the bulk proper motions with the length of the arrows indicating the average magnitude of the proper motion [in the bottom right of each panel is a scale-arrow showing the length of a 5 mas yr$^{-1}$ arrow] and the color of the arrows indicating how dispersed the measurements are within that particular bin. Note that the dispersion appears correlated with the Galactic plane and center – this indicates imperfect identification of extragalactic sources in these areas.

TABLE 11.1: Efficacy of Recentering

| | Average P.M. $\alpha$ | | Average P.M. $\delta$ | | Average P.M. Total | |
|---|---|---|---|---|---|---|
| | Before | After | Before | After | Before | After |
| WISE | -0.06 ± 13.73 | 0.02 ± 13.62 | -2.28 ± 12.51 | 0.12 ± 12.39 | 14.82 ± 11.43 | 14.43 ± 11.44 |
| ICRF VCS | -0.13 ± 7.93 | 0.25 ± 7.85 | -2.18 ± 7.29 | 0.11 ± 7.24 | 8.66 ± 6.77 | 8.16 ± 6.89 |
| ICRF Non-VCS | 0.44 ± 9.75 | 0.78 ± 9.57 | -2.14 ± 6.77 | -0.11 ± 6.84 | 8.85 ± 8.21 | 8.51 ± 8.16 |
| SDSS | | -0.37 ± 4.05 | | 0.46 ± 3.57 | | 4.53 ± 3.01 |

TABLE 11.2: Proper motions of a variety of extragalactic sources before and after we correct their PPMXL proper motions using the method described in the text. The SDSS pipeline proper motions are provided for reference.

# Chapter 12

# Discussion for Part III

In this Part we examined the information behind the data we used in our other analyses. First we examine the accuracy and precision of the proper motions presented in the SDSS data catalog. We find a number of observational characteristics, or metrics, that can be used to indirectly screen proper motion estimates that could be erroneous. While studying this proper motion catalog, we noticed that another catalog, the PPMXL catalog, seemed to have a serious offset from the SDSS proper motions.

To investigate this, in Chapter 11, we collected a sample of extragalactic objects using WISE and 2MASS colors as a discriminator. The PPMXL proper motions for these objects are then fitted to combinations of spherical harmonics in seven different magnitude slices. Considering that the intrinsic proper motions of these objects is negligible, we assume that the proper motions of objects in these slices indicates an offset from zero in the PPMXL proper motion catalog.

Interpolating between these slices generates a corrective volume which may be subtracted from any given point in the PPMXL database [which has a J magnitude measurement] to produce a new, corrected proper motion estimate. Note that this correction may be erroneous when considering extreme reddening regions such as the galactic plane, we would suggest using this correction only at absolute latitudes higher than 10 degrees.

With the launch of the European Space Agency keystone mission, Gaia, the scientific community eagerly awaits the promised data products of the 'billion star surveyor.' One of the most anticipated products is the Gaia proper motion catalog, which promises precisions of 20-200 $\mu$as yr$^{-1}$, a factor of 10-100 better than current proper motion catalogs.

However, it's important to remember that catalogs are never perfect and may contain non-obvious biases. Something as simple as the choice zero-point of the catalog could lead to large mismatches between catalogs [as we see in between the ICRS based PPMXL catalog and the galaxy based SDSS catalog]. Sometimes it can be valuable to consider errors introduced into the system by non-obvious metrics, such as crowded fields, or even just the magnitude of the proper motions. And some known problems in the system [such as stray-light and frame-flexion] could add noise into the data which may just be random noise, or which could be a systematic and correctable bias.

It will always be important to compare data catalogs, no matter how precise they are, with other catalogs. After all, high precision does not always imply high accuracy.

# Chapter 13

# Discussion

## 13.1 Review

This Dissertation centers on the exploration of the Milky Way specifically using stars. We use two types of stars [bright, old, blue horizontal branch stars and dim main sequence stars] to study the structure of the Milky Way in what we see [as for the structures in the halo of the Milky Way] and in side effects of what we don't see [as for stars kicked out of dense regions of the Milky Way spiral arms and nucleus].

In Part I we studied the Galactic halo using BHB stars. While this has been done before, we are the first to do it in the new Pan-STARRS data set. The Pan-STARRS data set is similar to that of SDSS but different enough that a whole new technique needed to be devised in Chapter 3 to identify BHB stars in the Pan-STARRS filters. In Chapter 4, we used this new technique to identify BHB stars and then performed an automated search through the Pan-STARRS footprint to identify substructure and we had a few interesting detections which bear further investigation.

Firstly there is the detection of 'group 6' identified by Starkenburg et al. (2009) in the Spaghetti Survey. We find this group in BHB stars, while Huxor & Grebel (2014, submitted) find it in carbon stars. This spread in tracer ages [with BHB stars being ancient objects and pulsating massive variables like carbon giants being intermediate age tracers] makes it a particularly intriguing candidate for follow up observations. We also identify some features in the area of Triangulum Andromeda, but our distance estimates contradict those in the literature; we need to reinvestigate this area of the sky more carefully to find out what is causing this disagreement. We also find a detection in the southern celestial hemisphere which could constitute a new detection of the Sagittarius trailing tidal tail in BHB stars. It lies in an area outside the SDSS footprint, so it has not yet been studied thoroughly the way the SDSS data set has.

In Part II, we took the intriguing phenomenon of 'runaway' stars, previously only studied in the O and B regime, and investigated it in the F-M regime and we learned a lot of interesting things about F-M type runaway stars. First and foremost, they exist. This topic has not been studied in depth before because it was just not possible before. When finding the velocity of an object meant you had to observe it yourself, it made sense to only pick the most likely candidates [i.e. massive stars in the halo], so no one bothered looking at unlikely candidates [i.e. dwarf stars in the disk]. But now with million-plus item spectroscopic surveys becoming more and more abundant [SDSS, RAVE, LAMOST, Gaia to an extent] and available it is possible to look for these types of outliers by trawling the databases. Some of the behavior we see is to be expected: for example the hottest F-M Hills stars seem to be associated with planar structures in the center of the Milky Way, while the cooler ones are more isotropic – this

is consistent with young stars being born in said planes and older stars being scattered out of those planes. But some behavior we see is also unexpected: for example the fact that almost half of our identified, high-probability, hypervelocity stars have orbits that never cross the disk or intersect any known structure – how is this possible, this has only been noted in F-M hypervelocity stars [see also Palladino et al. 2014], this is very strange and must be addressed.

We also inferred some conclusions about the structure of the Milky Way using these stars. We found that some stars may indeed have been kicked out of spiral arms, and some may indeed have interacted with a super massive black hole at the center of the Milky Way. The most interesting finding though is the tenative evidence for main sequence stars being kicked out of the nucleus to be of mixed origin, with some [presumably young objects] appearing to originate in the accreting planes of matter near the super massive black hole, and with some [presumably the older ones] originating in a more isotropic region about the center after sinking into the region or being scattered out of the accretion planes. This dual origin is something that can only be studied with long lived, low mass stars. B type runaway stars can likely only originate in the accreting planes of matter shortly before being ejected, whereas main sequence stars may live long enough to slowly accrete isotropically from the bulge and onto the central regions.

Out of concern for possible systematics and mis-reporting of errors on the proper motions we used in Part II, we more closely investigated the proper motions from the SDSS and PPMXL catalogs in Part III. To select only the best proper motion measurements from the SDSS, we constructed some metrics we could look at and found cutoffs in those metrics that seemed to imply accurate proper motions and used those as quality flags in Part II. However,during this, it was noticed that there was a large bit of mismatch between the SDSS proper motions, which are based on background galaxies as a reference frame, and PPMXL proper motions, which are based on the ICRS and Hipparcos. When we examined proper motions of galaxies and quasars in the PPMXL catalog, we found that they actually had non-zero average proper motions. So we fit the proper motions of these objects to spherical surfaces and then used these fits to recenter the PPMXL catalog.

## 13.2 Thoughts

Galactic exploration is a tremendous topic that has been studied since the beginning of humanity and will likely continue a few years more. In this Dissertation we looked at uncovering the structure of the Milky Way in a rather traditional way, by looking at the positions of tracers, and in a fairly novel way, by looking at the positions and velocities of certain tracers and inferring how they obtained that phase space coordinate. These are a few main thoughts I'd like to review from this Dissertation, along with some ideas for future works.

One recurring theme, and topic I personally find to be critical in future science, is the automation of search techniques. In Chapter 3, rather than choosing color cuts by eye to select BHB stars, we used a knn algorithm [a classification algorithm which classifies data in parameter space by its closest neighbors with a known classification in that parameter space] to find our selection box for us, this enforces an explainable and reproducible justification for the selection. In Chapter 4 we used a different method to produce our color cut, but this was mostly to examine the intrinsic trade offs between purity and completeness in any color based selection.

In Chapter 4 we also devised an automated search algorithm that would locate overdense areas in our observational footprint. Today the standard way to discover substructure is to plot spatial data of a known population [be they BHB stars, F-turnoff stars, or matched-filter color magnitude diagram cutouts] and to look by eye for dense areas. The method we used is subjective only in the choice of

search bin sizes and degree of overdensity cutoff that we wish to examine. Again, there is no subjectivity in this approach.

In Chapter II the issue of selecting the velocity cutoff for a star to be a 'hypervelocity' star comes to mind. Frequently in the literature, an arbitrary value will be chosen, say 550 km $s^{-1}$ and then the same velocity will be assumed for every position. The process of calculating individual escape speeds for individual stars is a minor, but critical aspect which again takes subjectivity out of the equation.

However, it is important to not blindly put faith in algorithmic constructs. For example, if we trust our methodology, the Galactic bulge would be a newly discovered substructure of the Milky Way BHBs [although this can be countered by improving our background subtraction method]. And also it is important to critically look at your data to make sure it makes sense; for example, the proper motions of extragalactic objects in the PPMXL catalog are non-zero.

There are several opportunities for this work to be expanded on and enhanced as well.

The least polished work is the study of the Milky Way halo in Pan-STARRS. This work could be much improved by using a better background subtraction for the smooth portion of the Milky Way halo; this could come from simulated models, or from empirical studies of the density of BHB stars in the Milky Way. This could also be an iterative project to discover the density profile of BHB stars in the Milky Way halo by looking at the positions of substructure in the data and ignoring them. Ideally one could fit both the smooth halo profile and the lumpy substructure profiles at the same time.

As we mentioned, the work with runaway stars could be improved in several ways. Firstly, we could expand our study to look at all metallicities of main sequence stars; this would likely lead to greater halo contamination, but would also increase our candidate pool. Secondly, this study would be easily transferrable to LAMOST and RAVE data – similar results could be found with identical techniques – this would also greatly increase our candidate pool. It would also be interesting to get high resolution spectra for some of our most promising objects in order to look at the chemical profiles of these objects with more depth.

The study of Galactic substructure is also notably improved by spectroscopic follow up. Spectroscopy offers two basic pieces of information about stars which are invaluable to substructure studies: radial velocity and chemical composition. With these two pieces of information, overdensities may be interpretted as related [having similar chemical compisition and velocity profiles as the neighboring stars] or coincidental [being more random in chemical fingerprint and phase space coordinates]. Detailed chemical abundances, such as alpha abundances can even help trace related populations within substructures and gradients in age across structures. All of this information is invaluable for modelers, who attempt to recreate these trends as well as spatial trends in density.

Finally, major improvement to all of the studies mentioned here should arrive with the Gaia data releases. Gaia will provide proper motions of unprecedented precision, which will be useful for comparing to other surveys, using other techniques to estimate proper motions, to try and figure out the true proper motions. Gaia will also provide parallax information and radial velocities for a tremendous number of objects all around the sky; this information will prove instrumental in the study of local bulk dynamics and will be a treasure trove for outlying objects. And of course, the Gaia mission will improve the accuracy of some of the lowest rungs of the cosmic distance ladder, which will ripple in turn to all studies of structure, Galactic and extragalactic.

# Bibliography


Abazajian, K. N., Adelman-McCarthy, J. K., Agüeros, M. A., et al. 2009, ApJS, 182, 543

Abbas, M. A., Grebel, E. K., Martin, N. F., et al. 2014, MNRAS, 441, 1230

Ahn, C. P., Alexandroff, R., Allende Prieto, C., et al. 2014, ApJS, 211, 17

Aihara, H., Allende Prieto, C., An, D., et al. 2011, ApJS, 193, 29

An, D., Johnson, J. A., Clem, J. L., et al. 2008, ApJS, 179, 326

Bell, E. F., Xue, X. X., Rix, H.-W., Ruhland, C., & Hogg, D. W. 2010, AJ, 140, 1850

Belokurov, V., Zucker, D. B., Evans, N. W., et al. 2006, ApJ, 642, L137

Belokurov, V., Evans, N. W., Bell, E. F., et al. 2007, ApJ, 657, L89

Belokurov, V., Koposov, S. E., Evans, N. W., et al. 2014, MNRAS, 437, 116

Bensby, T., Feltzing, S., & Lundström, I. 2004, A&A, 421, 969

Binney, J., & Merrifield, M. 1998, Galactic Astronomy (Princeton, NJ: Princeton Univ. Press)

Blaauw, A. 1961, Bull. Astron. Inst. Netherlands, 15, 265

Bramich, D. M., Vidrih, S., Wyrzykowski, L., et al. 2008, MNRAS, 386, 887

Brown, W. R., Geller, M. J., Kenyon, S. J., & Kurtz, M. J. 2005, ApJ, 622, L33

Brown, W. R., Geller, M. J., & Kenyon, S. J. 2012, ApJ, 751, 55

Casetti-Dinescu, D. I., Girard, T. M., Herrera, D., et al. 2007, AJ, 134, 195

Casetti-Dinescu, D. I., Girard, T. M., Korchagin, V. I., van Altena, W. F., & López, C. E. 2010, AJ, 140, 1282

Casetti-Dinescu, D. I., Girard, T. M., Jílková, L., et al. 2013, AJ, 146, 33

Clemens, D. P. 1985, ApJ, 295, 422

Clewley, L., Warren, S. J., Hewett, P. C., et al. 2002, MNRAS, 337, 87

Clewley, L., Warren, S. J., Hewett, P. C., et al. 2005, MNRAS, 362, 349

Clewley, L., & Jarvis, M. J. 2006, MNRAS, 368, 310

Cui, X.-Q., Zhao, Y.-H., Chu, Y.-Q., et al. 2012, Research in Astronomy and Astrophysics, 12, 1197

Deason, A. J., Belokurov, V., & Evans, N. W. 2011, MNRAS, 416, 2903

Dehnen, W., & Binney, J. 1998, MNRAS, 294, 429

Dinescu, D. I., Girard, T. M., van Altena, W. F., Mendez, R. A., & Lopez, C. E. 1997, AJ, 114, 1014

Dinescu, D. I., van Altena, W. F., Girard, T. M., & López, C. E. 1999, AJ, 117, 277

Dinescu, D. I., Girard, T. M., & van Altena, W. F. 1999, AJ, 117, 1792

Dinescu, D. I., Girard, T. M., van Altena, W. F., & López, C. E. 2003, AJ, 125, 1373

Doi, M., Tanaka, M., Fukugita, M., et al. 2010, AJ, 139, 1628

Dotter, A., Chaboyer, B., Jevremović, D., et al. 2008, ApJS, 178, 89

Dotter, A., Sarajedini, A., Anderson, J., et al. 2010, ApJ, 708, 698

Drake, A. J., Catelan, M., Djorgovski, S. G., et al. 2013, ApJ, 765, 154

ESA 1997, VizieR Online Data Catalog, 1239, 0

Fey, A.L., Gordon, D., Jacobs, C.S. (eds.), 2009 IERS Technical Note; No. 35; Bundesamt für Kartographie und Geodäsie, Frankfurt am Main

Figer, D. F., Gilmore, D., Kim, S. S., et al. 2003, ApJ, 599, 1139

Fremat, Y., Houziaux, L., & Andrillat, Y. 1996, MNRAS, 279, 25

Frieman, J. A., Bassett, B., Becker, A., et al. 2008, AJ, 135, 338

Fukugita, M., Ichikawa, T., Gunn, J. E., et al. 1996, AJ, 111, 1748

Gunn, J. E., Carr, M., Rockosi, C., et al. 1998, AJ, 116, 3040

Gvaramadze, V. V., Gualandris, A., & Portegies Zwart, S. 2009, MNRAS, 396, 570

Gvaramadze, V. V. 2009, MNRAS, 395, L85

Hambly, N. C., MacGillivray, H. T., Read, M. A., et al. 2001, MNRAS, 326, 1279

Harris, W. E. 1996, AJ, 112, 1487

Hills, J. G. 1988, Nature, 331, 687

Huxor, Avon P., Grebel, Eva K. 2014, MNRAS, submitted

Ibata, R. A., Gilmore, G., & Irwin, M. J. 1994, Nature, 370, 194

Ivezić, Ž., Sesar, B., Jurić, M., et al. 2008, ApJ, 684, 287

Ivezic, Z., Tyson, J. A., Acosta, E., et al. 2008, arXiv:0805.2366

Johnson, D. R. H., & Soderblom, D. R. 1987, AJ, 93, 864

Jordi, K., & Grebel, E. K. 2010, A&A, 522, A71

Jurić, M., Ivezić, Ž., Brooks, A., et al. 2008, ApJ, 673, 864

Kaiser, N., Burgett, W., Chambers, K., et al. 2010, Proc. SPIE, 7733,

Kirkpatrick, J. D., Cushing, M. C., Gelino, C. R., et al. 2011, ApJS, 197, 19

Koposov, S. E., Belokurov, V., & Wyn Evans, N. 2013, ApJ, 766, 79

Kouwenhoven, M. B. N., Brown, A. G. A., Goodwin, S. P., Portegies Zwart, S. F., & Kaper, L. 2009, A&A, 493, 979

Kovács, A., & Szapudi, I. 2013, arXiv:1401.0156

Law, D. R., & Majewski, S. R. 2010, ApJ, 714, 229

Lee, Y. S., Beers, T. C., Sivarani, T., et al. 2008, AJ, 136, 2022

Lenz, D. D., Newberg, J., Rosner, R., Richards, G. T., & Stoughton, C. 1998, ApJS, 119, 121

Leonard, P. J. T., & Duncan, M. J. 1990, AJ, 99, 608

Lu, Y., Yu, Q., & Lin, D. N. C. 2007, ApJ, 666, L89

Lu, Y., Zhang, F., & Yu, Q. 2010, ApJ, 709, 1356

Majewski, S. R., Skrutskie, M. F., Weinberg, M. D., & Ostheimer, J. C. 2003, ApJ, 599, 1082

Manukian, H., Guillochon, J., Ramirez-Ruiz, E., & O'Leary, R. M. 2013, ApJ, 771, L28

McMillan, P. J. 2011, MNRAS, 414, 2446

Miralda-Escudé, J., & Gould, A. 2000, ApJ, 545, 847

Monet, D. G., Levine, S. E., Canzian, B., et al. 2003, AJ, 125, 984

Morrison, H. L., Mateo, M., Olszewski, E. W., et al. 2000, AJ, 119, 2254

Moultaka, J., Ilovaisky, S. A., Prugniel, P., & Soubiran, C. 2004, PASP, 116, 693

Munn, J. A., Monet, D. G., Levine, S. E., et al. 2004, AJ, 127, 3034

Ness, M., Freeman, K., Athanassoula, E., et al. 2013, MNRAS, 432, 2092

Newberg, H. J., Yanny, B., Rockosi, C., et al. 2002, ApJ, 569, 245

Newberg, H. J., Yanny, B., Grebel, E. K., et al. 2003, ApJ, 596, L191

Palladino, L. E.,Schlesinger, K. J., Holley-Bockelmann, K., et al. 2014, ApJ, 780, 7

Paumard, T., Genzel, R., Martins, F., et al. 2006, ApJ, 643, 1011

Pier, J. R. 1983, ApJS, 53, 791

Poveda, A., Ruiz, J., & Allen, C. 1967, Boletin de los Observatorios Tonantzintla y Tacubaya, 4, 86

Pradhan, A. C., Ojha, D. K., Robin, A. C., Ghosh, S. K., & Vickers, J. J. 2014, A&A, 565, A33

Richards, G. T., Myers, A. D., Gray, A. G., et al. 2009, ApJS, 180, 67

Rix, H.-W., & Bovy, J. 2013, A&A Rev., 21, 61

Robin, A. C., Reylé, C., & Crézé, M. 2000, A&A, 359, 103

Robin, A. C., Reylé, C., Derrière, S., & Picaud, S. 2003, A&A, 409, 523

Roeser, S., Demleitner, M., & Schilbach, E. 2010, AJ, 139, 2440

Ruhland, C., Bell, E. F., Rix, H.-W., & Xue, X.-X. 2011, ApJ, 731, 119

Sale, S. E., Drew, J. E., Knigge, C., et al. 2010, MNRAS, 402, 713

Scheck, L., Kifonidis, K., Janka, H.-T., Müller, E. 2006, A&A, 457, 963

Schlafly, E. F., Finkbeiner, D. P., Jurić, M., et al. 2012, ApJ, 756, 158

Schlafly, E. F., Green, G., Finkbeiner, D. P., et al. 2014, ApJ, 789, 15

Schlegel, D. J., Finkbeiner, D. P., & Davis, M. 1998, ApJ, 500, 525

Schönrich, R., & Binney, J. 2012, MNRAS, 419, 1546

Slater, C. T., Bell, E. F., Schlafly, E. F., et al. 2013, ApJ, 762, 6

Sesar, B., Ivezić, Ž., Lupton, R. H., et al. 2007, AJ, 134, 2236

Sesar, B., Ivezić, Ž., Grammer, S. H., et al. 2010, ApJ, 708, 717

Sheffield, A., Johnston, K., Majewski, S., et al. 2014, arXiv:1407.4463

Silva, M. D. V., & Napiwotzki, R. 2013, MNRAS, 431, 502

Simion, I. T., Belokurov, V., Irwin, M., & Koposov, S. E. 2014, MNRAS, 440, 161

Sirko, E., Goodman, J., Knapp, G. R., et al. 2004, AJ, 127, 899

Skrutskie, M. F., Cutri, R. M., Stiening, R., et al. 2006, AJ, 131, 1163

Smith, M. C., Evans, N. W., Belokurov, V., et al. 2009, MNRAS, 399, 1223

Smith, M. C., Whiteoak, S. H., & Evans, N. W. 2012, ApJ, 746, 181

Starkenburg, E., Helmi, A., Morrison, H. L., et al. 2009, ApJ, 698, 567

Steinmetz, M., Zwitter, T., Siebert, A., et al. 2006, AJ, 132, 1645

Stoughton, C., Lupton, R. H., Bernardi, M., et al. 2002, AJ, 123, 485

Stubbs, C. W., Doherty, P., Cramer, C., et al. 2010, ApJS, 191, 376

Tody, D. 1986, Proc. SPIE, 627, 733

Vallée, J. P. 2008, AJ, 135, 1301

VanderPlas, J., Connolly, A. J., Ivezic, Z., & Gray, A. 2012, in Proc. Conf. on Intelligent Data Understanding (CIDU), ed. K. Das, N. V. Chawla & A. N. Srivastava (Boulder, Colorado: NCAR), 47

Vickers, J. J., Grebel, E. K., & Huxor, A. P. 2012, AJ, 143, 86

Vickers, John J., Smith, Martin C., Grebel, Eva K. 2014, AJ, submitted

Vivas, A. K., Zinn, R., Andrews, P., et al. 2001, ApJ, 554, L33

Wilhelm, R., Beers, T. C., Sommer-Larsen, J., et al. 1999, AJ, 117, 2329

Wright, E. L., Eisenhardt, P. R. M., Mainzer, A. K., et al. 2010, AJ, 140, 1868

Wu, Z.-Y., Ma, J., & Zhou, X. 2011, PASP, 123, 1313

Xue, X. X., Rix, H. W., Zhao, G., et al. 2008, ApJ, 684, 1143

Yanny, B., Newberg, H. J., Kent, S., et al. 2000, ApJ, 540, 825

Yanny, B., Rockosi, C., Newberg, H. J., et al. 2009, AJ, 137, 4377

York, D. G., Adelman, J., Anderson, J. E., Jr., et al. 2000, AJ, 120, 1579

Zacharias, N., Urban, S. E., Zacharias, M. I., et al. 2000, AJ, 120, 2131

Zheng, Z., Carlin, J. L., Beers, T. C., et al. 2014, ApJ, 785, L23

| IAU Name | $\Delta$ P.M. mas yr$^{-1}$ | Nearest Neighbor arcseconds | Total P.M mas yr$^{-1}$ | $\sigma$ P.M. mas yr$^{-1}$ | [Fe/H] dex | $V_{Total}$ km s$^{-1}$ | $V_{esc}$ km s$^{-1}$ | Infalling |
|---|---|---|---|---|---|---|---|---|
| J082015.88+362223.26 | 9.05 | 24.2 | 24.27 | 4.7 | -0.73 | 612.13 | 523.83 | X |
| J160707.30+372350.97 | 9.13 | 19.8 | 15.83 | 4.36 | -0.11 | 580.49 | 548.79 | |
| J131238.82+393312.13 | 8.57 | 11.13 | 22.96 | 4.75 | -0.63 | 577.19 | 531.07 | |
| J175010.68+262448.38 | 4.72 | 13.32 | 20.9 | 4.47 | -0.52 | 606.88 | 577.02 | |
| J075516.37+662909.15 | 9.25 | 16.57 | 8.95 | 4.94 | -0.72 | 565.12 | 506.21 | X |
| J024605.10+312254.29 | 4.04 | 16.22 | 11.0 | 4.94 | -0.27 | 546.29 | 518.32 | X |
| J093103.04+134728.81 | 5.63 | 12.95 | 9.1 | 4.55 | -0.51 | 531.91 | 509.41 | |

TABLE 1: Hypervelocity candidates with 0 flags. These objects have kinetic energies greater than the gravitational potential at their given position. Starred objects are candidates from Palladino et al. (2014). The table is split into five separate tables based on the number of quality metrics, or flags, that the observation raises. These flags are outlined in Chapter 10, an object with 0 flags is a high quality observation, while four flags is not very reliable.

TABLE 2: Hypervelocity Candidates with 1 Flag

| IAU Name | Δ P.M. mas yr$^{-1}$ | Nearest Neighbor arcseconds | Total P.M mas yr$^{-1}$ | $\sigma$ P.M. mas yr$^{-1}$ | [Fe/H] dex | $V_{Total}$ km s$^{-1}$ | $V_{esc}$ km s$^{-1}$ | Infalling |
|---|---|---|---|---|---|---|---|---|
| J145132.12+003258.02* | 9.76 | 11.09 | 16.46 | 8.26 | -0.59 | 589.0 | 578.8 | X |
| J003607.75+141425.65 | 2.93 | 10.55 | 15.58 | 5.61 | -0.8 | 591.52 | 535.56 | X |
| J082552.41-000847.20 | 5.79 | 11.17 | 9.21 | 5.82 | -0.71 | 615.65 | 498.04 | |
| J075101.46+375539.93 | 8.76 | 22.41 | 22.58 | 6.56 | -0.24 | 1026.01 | 495.47 | X |
| J075243.74+355306.45 | 8.11 | 13.89 | 9.74 | 5.32 | -0.54 | 544.54 | 496.35 | X |
| J104558.18-004855.54 | 5.33 | 11.44 | 14.3 | 5.72 | 0.41 | 530.04 | 523.01 | |
| J075238.30+290658.84 | 19.43 | 16.73 | 18.91 | 4.76 | -0.71 | 687.52 | 520.7 | X |
| J090810.59+393808.36 | 9.76 | 10.02 | 14.02 | 5.44 | -0.6 | 532.94 | 526.2 | |
| J093342.56+443657.82 | 7.41 | 2.24 | 12.15 | 4.55 | -0.1 | 739.92 | 495.46 | X |
| J082225.17+334430.61 | 1.52 | 9.47 | 22.61 | 4.32 | -0.43 | 597.47 | 529.14 | |
| J093644.57+381635.72 | 4.19 | 10.97 | 5.0 | 5.12 | -0.04 | 505.7 | 490.55 | |
| J160720.20+372933.41 | 15.41 | 15.2 | 17.29 | 4.29 | -0.53 | 779.85 | 546.87 | |
| J032048.82+411455.22 | 6.16 | 6.05 | 17.31 | 4.92 | -0.53 | 637.81 | 523.99 | X |
| J000613.04+291353.34 | 5.54 | 10.28 | 14.21 | 5.05 | -0.37 | 533.74 | 532.15 | |
| J183155.19+205839.07 | 6.02 | 6.3 | 6.84 | 3.55 | -0.21 | 1096.17 | 580.4 | |
| J183402.98+215017.57 | 5.56 | 7.38 | 4.93 | 3.57 | -0.19 | 967.03 | 583.23 | |
| J071351.68+392946.37 | 8.21 | 7.27 | 15.81 | 4.89 | -0.62 | 616.36 | 516.92 | X |
| J072427.09+403554.18 | 13.55 | 11.19 | 7.5 | 4.82 | -0.65 | 508.55 | 504.55 | X |
| J072125.29+385314.67 | 10.17 | 19.57 | 9.63 | 5.03 | -0.78 | 570.75 | 507.11 | |
| J092613.30+201253.07 | 11.76 | 4.13 | 12.01 | 4.31 | -0.52 | 536.88 | 525.23 | |
| J092625.59+200758.80 | 25.78 | 15.36 | 20.07 | 4.15 | -0.58 | 696.97 | 529.59 | |
| J080531.08+191443.69 | 11.55 | 4.32 | 13.58 | 3.69 | -0.55 | 635.03 | 514.77 | |
| J082648.83+362414.55 | 4.67 | 6.64 | 24.87 | 3.4 | -0.49 | 665.38 | 535.01 | X |
| J161837.44+321436.03 | 4.54 | 7.99 | 26.45 | 3.89 | -0.7 | 581.14 | 572.5 | X |
| J073542.36+164941.47 | 10.43 | 6.64 | 28.75 | 3.97 | -0.23 | 737.46 | 533.48 | |
| J070716.03+125729.15 | 7.83 | 4.53 | 9.4 | 4.25 | -0.68 | 643.78 | 494.56 | |
| J080132.31+095111.59 | 2.89 | 4.74 | 7.87 | 4.89 | -0.77 | 569.12 | 488.19 | |
| J064531.12+275042.42 | 6.35 | 9.47 | 20.81 | 4.32 | -0.51 | 543.83 | 537.96 | X |
| J063254.61+272941.86 | 6.99 | 7.12 | 29.44 | 4.85 | -0.39 | 560.29 | 541.36 | X |
| J085000.71+113234.74 | 10.53 | 5.09 | 9.51 | 4.86 | -0.54 | 545.13 | 506.51 | |
| J070432.74+284331.30 | 3.36 | 8.37 | 18.25 | 4.3 | -0.75 | 657.14 | 508.09 | |

*Continued on next page*

Table 2 – *Continued from previous page*

| IAU Name | Δ P.M. mas yr$^{-1}$ | Nearest Neighbor arcseconds | Total P.M mas yr$^{-1}$ | $\sigma$ P.M. mas yr$^{-1}$ | [Fe/H] dex | $V_{Total}$ km s$^{-1}$ | $V_{esc}$ km s$^{-1}$ | Infalling |
|---|---|---|---|---|---|---|---|---|
| J065412.40+292304.90 | 2.59 | 6.93 | 27.37 | 3.74 | -0.29 | 648.36 | 538.29 | X |
| J070025.61+300628.50 | 3.44 | 8.13 | 20.07 | 3.85 | -0.31 | 586.81 | 533.65 | X |
| J065827.16+291313.17 | 6.96 | 5.98 | 17.96 | 4.01 | -0.7 | 536.18 | 528.28 | |
| J045025.80-041616.68 | 16.81 | 19.63 | 19.09 | 4.07 | -0.76 | 667.36 | 526.28 | |

TABLE 3: Hypervelocity Candidates with 2 Flags

| IAU Name | Δ P.M. mas yr$^{-1}$ | Nearest Neighbor arcseconds | Total P.M mas yr$^{-1}$ | $\sigma$ P.M. mas yr$^{-1}$ | [Fe/H] dex | $V_{Total}$ km s$^{-1}$ | $V_{esc}$ km s$^{-1}$ | Infalling |
|---|---|---|---|---|---|---|---|---|
| J112714.55-005301.33 | 7.95 | 8.17 | 21.06 | 7.2 | -0.01 | 594.93 | 538.58 | |
| J100054.80+004357.35 | 13.98 | 12.49 | 19.07 | 8.21 | -0.53 | 803.97 | 517.69 | X |
| J104613.69-002513.53 | 14.97 | 11.42 | 18.83 | 5.81 | -0.66 | 730.58 | 516.21 | X |
| J081932.03+001947.36 | 23.69 | 1.16 | 20.1 | 4.49 | -0.69 | 654.98 | 521.47 | X |
| J112847.51+653746.44 | 7.22 | 7.07 | 11.23 | 5.17 | -0.33 | 581.62 | 522.95 | X |
| J081210.06+001211.10 | 7.63 | 8.93 | 8.76 | 5.85 | -0.57 | 597.33 | 498.0 | |
| J095803.54-001725.30* | 7.01 | 14.35 | 61.57 | 7.26 | -0.64 | 1249.66 | 543.6 | X |
| J204056.87-062124.09 | 23.92 | 5.41 | 25.51 | 4.64 | -0.67 | 667.38 | 591.39 | X |
| J082756.04+011028.70 | 11.99 | 4.44 | 17.85 | 8.12 | -0.64 | 809.5 | 490.94 | X |
| J085508.04+031505.41 | 3.44 | 8.34 | 6.97 | 5.85 | -0.79 | 575.28 | 482.67 | X |
| J085545.13+021458.07 | 8.66 | 4.97 | 61.73 | 4.05 | -0.56 | 740.44 | 547.25 | |
| J072836.28+343351.93 | 18.75 | 2.03 | 16.45 | 4.93 | -0.66 | 793.57 | 505.37 | X |
| J082249.67+461416.29 | 13.09 | 6.26 | 15.31 | 4.64 | -0.67 | 778.42 | 505.2 | X |
| J203608.68-060057.17 | 3.57 | 4.88 | 20.53 | 7.17 | -0.52 | 596.07 | 591.69 | X |
| J003450.19+160433.26 | 16.73 | 6.98 | 21.02 | 4.11 | -0.48 | 569.94 | 547.04 | X |
| J110404.21+021650.31 | 8.54 | 3.41 | 11.42 | 5.34 | 0.27 | 533.31 | 526.24 | |
| J074811.00+282130.39 | 16.66 | 7.99 | 13.56 | 4.61 | -0.71 | 590.53 | 515.09 | X |
| J212043.19+103111.32 | 22.19 | 3.08 | 27.26 | 3.99 | -0.56 | 604.33 | 576.75 | X |
| J212128.12+103730.26 | 3.76 | 4.49 | 66.52 | 3.69 | -0.56 | 995.09 | 577.37 | X |
| J075627.42+274144.58 | 3.43 | 4.0 | 12.86 | 5.71 | -0.68 | 603.34 | 512.58 | |
| J074722.67+283724.79 | 25.3 | 5.6 | 24.57 | 4.59 | -0.34 | 636.03 | 533.51 | |
| J075209.71+273214.34 | 0.7 | 5.62 | 20.08 | 5.14 | -0.7 | 1055.3 | 499.44 | |
| J074256.46+275946.95 | 3.22 | 5.9 | 5.28 | 5.6 | -0.75 | 514.88 | 484.54 | |
| J095629.99+454906.20 | 6.03 | 12.43 | 66.85 | 11.68 | -0.51 | 1795.57 | 529.52 | X |
| J090534.10+405537.78 | 22.48 | 1.81 | 18.66 | 3.94 | -0.46 | 550.96 | 538.26 | |
| J141834.05+501941.07 | 6.79 | 22.58 | 46.92 | 6.14 | -0.75 | 572.88 | 562.43 | |
| J032254.29+414358.54 | 5.58 | 9.02 | 20.78 | 5.47 | -0.48 | 541.49 | 526.12 | |
| J082456.26+323805.79 | 21.62 | 3.43 | 21.24 | 4.2 | -0.75 | 686.41 | 520.31 | X |
| J010922.05+454520.81 | 15.68 | 2.38 | 16.4 | 4.33 | -0.65 | 547.44 | 534.73 | X |
| J011011.24+473038.04 | 14.59 | 3.06 | 26.5 | 4.11 | -0.34 | 659.17 | 530.44 | X |
| J082410.12+301833.52 | 20.49 | 8.81 | 22.81 | 4.58 | -0.68 | 820.13 | 517.53 | |

*Continued on next page*

Table 3 – *Continued from previous page*

| IAU Name | Δ P.M. mas yr$^{-1}$ | Nearest Neighbor arcseconds | Total P.M mas yr$^{-1}$ | $\sigma$ P.M. mas yr$^{-1}$ | [Fe/H] dex | $V_{Total}$ km s$^{-1}$ | $V_{esc}$ km s$^{-1}$ | Infalling |
|---|---|---|---|---|---|---|---|---|
| J010757.52+464259.66 | 3.71 | 4.27 | 19.76 | 7.51 | -0.68 | 700.52 | 526.14 | X |
| J011226.04+472051.64 | 20.79 | 4.41 | 19.29 | 4.42 | -0.46 | 630.79 | 530.2 | |
| J093913.73+382905.11 | 19.14 | 4.53 | 18.9 | 4.05 | -0.59 | 579.33 | 535.8 | |
| J103026.65+080707.69 | 3.35 | 6.06 | 15.12 | 5.48 | -0.57 | 567.41 | 536.54 | |
| J073554.05+221533.98 | 31.65 | 8.87 | 27.64 | 4.56 | -0.33 | 731.37 | 532.84 | |
| J092619.98+092919.75 | 15.97 | 14.5 | 14.46 | 5.36 | -0.46 | 652.55 | 514.41 | X |
| J084210.86+052305.58 | 26.44 | 7.15 | 21.01 | 4.2 | -0.7 | 591.77 | 525.95 | |
| J074232.64+211017.80 | 3.57 | 4.18 | 13.92 | 5.19 | 0.39 | 911.9 | 463.76 | |
| J074317.75+191459.14* | 9.43 | 8.04 | 18.74 | 5.34 | -0.61 | 572.85 | 518.14 | X |
| J212101.55+000256.18 | 1.26 | 3.73 | 48.79 | 4.21 | -0.57 | 947.57 | 580.4 | X |
| J212702.61+002702.38 | 5.1 | 4.63 | 69.64 | 4.01 | -0.74 | 838.71 | 579.09 | X |
| J000727.58+260741.33 | 2.01 | 4.19 | 73.75 | 4.38 | -0.73 | 1007.65 | 554.11 | |
| J232545.03-011344.09 | 4.18 | 6.62 | 104.67 | 4.69 | -0.79 | 1023.61 | 565.47 | |
| J084115.30+062000.96 | 30.32 | 12.42 | 31.98 | 3.78 | -0.49 | 784.58 | 537.86 | |
| J215946.78+004400.23 | 12.0 | 4.46 | 53.77 | 3.97 | -0.46 | 591.87 | 575.04 | |
| J160419.74+365623.57 | 3.62 | 10.74 | 57.5 | 7.27 | -0.36 | 788.18 | 572.75 | |
| J204527.99-010125.19 | 20.62 | 1.51 | 20.61 | 3.69 | -0.33 | 652.4 | 584.27 | X |
| J233759.54+451444.91 | 0.82 | 16.95 | 65.19 | 9.59 | -0.4 | 1049.74 | 554.62 | X |
| J080201.62+200637.31 | 2.3 | 5.65 | 21.29 | 6.6 | -0.75 | 841.43 | 513.22 | |
| J234446.22+462721.49* | 22.54 | 5.21 | 26.5 | 4.47 | -0.44 | 673.83 | 545.4 | X |
| J232939.29+493558.21 | 8.97 | 3.93 | 58.37 | 3.86 | -0.69 | 1074.73 | 551.89 | X |
| J145021.46+105714.46 | 14.16 | 7.89 | 10.38 | 4.88 | -0.42 | 629.12 | 550.65 | X |
| J072331.00+374628.22 | 21.08 | 10.36 | 23.96 | 8.43 | -0.22 | 1382.05 | 487.88 | X |
| J012306.01+403951.23 | 8.57 | 4.03 | 45.26 | 3.59 | -0.13 | 803.15 | 546.99 | X |
| J005833.75+003508.71 | 25.29 | 4.99 | 20.98 | 3.67 | -0.49 | 573.36 | 547.9 | X |
| J090243.81+272032.84 | 23.22 | 2.43 | 23.16 | 3.74 | -0.16 | 566.11 | 542.48 | |
| J011933.46+384913.06 | 3.8 | 4.43 | 65.46 | 4.07 | -0.67 | 949.7 | 545.39 | |
| J004641.51+245831.75 | 7.58 | 4.85 | 62.19 | 3.77 | -0.77 | 856.92 | 551.19 | X |
| J071539.69+391306.21 | 16.75 | 7.2 | 27.04 | 3.85 | -0.47 | 623.61 | 534.76 | X |
| J092843.92+220642.44 | 3.25 | 4.91 | 68.53 | 4.95 | -0.67 | 1304.5 | 538.3 | X |
| J072334.82+403014.50 | 26.25 | 6.22 | 25.16 | 4.66 | -0.59 | 1198.75 | 502.59 | X |
| J102707.26+281435.48 | 20.1 | 4.33 | 24.3 | 3.82 | -0.67 | 614.09 | 543.49 | |

*Continued on next page*

Table 3 – *Continued from previous page*

| IAU Name | Δ P.M. mas yr$^{-1}$ | Nearest Neighbor arcseconds | Total P.M mas yr$^{-1}$ | $\sigma$ P.M. mas yr$^{-1}$ | [Fe/H] dex | $V_{Total}$ km s$^{-1}$ | $V_{esc}$ km s$^{-1}$ | Infalling |
|---|---|---|---|---|---|---|---|---|
| J082324.46+160507.22 | 28.24 | 5.06 | 10.77 | 4.48 | -0.56 | 560.66 | 514.96 | |
| J182630.57+215302.70 | 15.94 | 4.68 | 20.61 | 4.11 | -0.54 | 594.56 | 590.25 | |
| J173604.78+324805.39 | 35.1 | 6.13 | 20.61 | 4.82 | -0.6 | 610.93 | 576.17 | X |
| J173620.31+322415.89 | 24.51 | 9.17 | 21.95 | 4.52 | -0.23 | 607.98 | 576.9 | X |
| J173712.93+321518.17 | 21.38 | 6.56 | 22.33 | 4.62 | -0.33 | 647.61 | 576.25 | X |
| J023849.85+281023.60 | 9.24 | 8.75 | 15.07 | 7.22 | -0.37 | 645.02 | 506.43 | |
| J205144.77+160355.64 | 8.21 | 4.29 | 64.1 | 3.83 | -0.39 | 890.83 | 579.6 | |
| J203608.79+151728.35 | 35.18 | 4.49 | 29.27 | 3.85 | -0.37 | 647.71 | 582.42 | X |
| J202021.64+140742.90 | 24.18 | 3.48 | 23.59 | 3.91 | -0.37 | 623.87 | 585.89 | |
| J044830.91-002830.10 | 25.78 | 3.88 | 16.74 | 4.55 | -0.61 | 628.43 | 505.26 | |
| J192541.52+375541.93 | 8.81 | 4.97 | 52.26 | 4.83 | -0.24 | 645.13 | 576.49 | |
| J082622.27+132728.33 | 25.87 | 7.02 | 23.5 | 3.82 | -0.51 | 889.16 | 516.78 | |
| J172630.61+075544.10 | 3.92 | 3.84 | 59.71 | 4.06 | -0.67 | 901.67 | 598.74 | X |
| J033730.09+002025.04 | 19.05 | 10.2 | 23.85 | 6.25 | -0.66 | 671.29 | 526.97 | |
| J173453.83+075628.50 | 11.36 | 4.43 | 75.06 | 3.69 | -0.79 | 745.97 | 585.43 | |
| J173241.12+090358.50 | 21.16 | 3.93 | 22.98 | 4.82 | -0.73 | 731.23 | 603.49 | X |
| J090003.97+111858.98 | 5.55 | 4.09 | 23.64 | 6.64 | -0.43 | 599.4 | 518.4 | X |
| J124313.57+151414.82 | 2.07 | 2.48 | 11.89 | 5.03 | -0.35 | 690.61 | 528.47 | |
| J225912.13+074356.53 | 9.65 | 17.57 | 44.9 | 5.58 | -0.56 | 842.17 | 556.45 | |
| J071409.76+305127.87 | 25.74 | 1.83 | 21.61 | 4.33 | -0.52 | 1249.22 | 491.96 | |
| J023000.98+255656.41 | 10.06 | 5.64 | 30.86 | 3.72 | -0.71 | 579.19 | 544.97 | X |
| J064257.02+371604.28 | 5.13 | 4.57 | 49.09 | 3.6 | -0.33 | 592.94 | 551.83 | |
| J204132.64+152708.00 | 34.96 | 5.67 | 17.88 | 4.41 | -0.43 | 1131.05 | 538.74 | X |
| J060306.77+825829.20 | 3.38 | 5.62 | 56.08 | 3.72 | -0.06 | 696.93 | 545.7 | |
| J065128.81+830620.38 | 6.86 | 8.92 | 50.57 | 3.98 | 0.08 | 1817.93 | 519.63 | X |
| J202223.58+143533.38 | 3.68 | 4.17 | 62.21 | 4.05 | -0.43 | 958.98 | 585.23 | |
| J053055.16+624225.68 | 16.93 | 4.7 | 20.53 | 4.17 | -0.11 | 616.54 | 531.34 | X |
| J051955.34+622136.19 | 2.94 | 3.87 | 90.93 | 4.83 | -0.39 | 840.52 | 557.25 | |
| J113237.93-072241.78 | 13.26 | 12.62 | 15.65 | 5.85 | -0.65 | 564.86 | 532.66 | |
| J064751.76+280407.08 | 3.83 | 4.81 | 68.27 | 3.38 | -0.29 | 646.71 | 545.02 | |
| J065319.11+291712.28 | 6.27 | 6.6 | 62.01 | 3.39 | -0.34 | 935.47 | 544.69 | X |
| J074546.28+172248.30 | 22.5 | 1.36 | 18.69 | 3.7 | -0.33 | 580.88 | 526.47 | X |

*Continued on next page*

Table 3 – *Continued from previous page*

| IAU Name | Δ P.M. mas yr$^{-1}$ | Nearest Neighbor arcseconds | Total P.M mas yr$^{-1}$ | $\sigma$ P.M. mas yr$^{-1}$ | [Fe/H] dex | $V_{Total}$ km s$^{-1}$ | $V_{esc}$ km s$^{-1}$ | Infalling |
|---|---|---|---|---|---|---|---|---|
| J074920.08+175147.75 | 21.18 | 14.21 | 17.39 | 6.6 | -0.59 | 673.88 | 521.67 | |
| J073123.11+161628.13 | 23.85 | 4.31 | 21.49 | 4.1 | -0.66 | 561.57 | 538.25 | |
| J220204.45+454351.67 | 10.33 | 4.03 | 63.33 | 3.54 | -0.06 | 855.31 | 563.49 | |
| J215855.40+445204.60 | 2.16 | 4.4 | 63.72 | 4.42 | -0.14 | 707.73 | 565.88 | |
| J074344.91+182640.94 | 11.14 | 11.3 | 49.7 | 6.38 | -0.6 | 2345.94 | 489.28 | X |
| J192601.70+383506.80 | 23.42 | 4.36 | 25.56 | 3.78 | -0.27 | 623.94 | 572.41 | X |
| J070442.41+122720.32 | 3.16 | 3.89 | 36.36 | 3.57 | -0.23 | 669.74 | 544.49 | |
| J070500.87+124738.14 | 3.23 | 2.6 | 45.47 | 4.45 | -0.43 | 946.17 | 529.47 | |
| J070537.17+132309.48 | 17.94 | 6.98 | 17.36 | 4.36 | -0.65 | 573.31 | 506.01 | |
| J070657.47+122724.97 | 8.56 | 4.1 | 34.99 | 4.67 | -0.7 | 645.77 | 540.93 | X |
| J044827.52+221051.07 | 29.2 | 5.53 | 28.22 | 4.39 | -0.38 | 580.39 | 543.05 | X |
| J070132.92+124539.10 | 22.25 | 2.26 | 20.1 | 3.88 | -0.33 | 693.63 | 519.97 | |
| J070327.47+120225.34 | 24.77 | 3.15 | 20.62 | 3.62 | -0.42 | 616.11 | 530.37 | |
| J044753.84-050857.18 | 15.6 | 4.91 | 22.66 | 3.83 | -0.72 | 582.05 | 538.35 | |
| J070555.14+133525.75 | 14.86 | 5.05 | 21.74 | 3.6 | -0.56 | 693.75 | 518.45 | X |
| J082813.98-052143.88 | 20.16 | 1.77 | 13.18 | 3.79 | -0.51 | 596.3 | 518.12 | |
| J070102.98+123754.14 | 16.95 | 4.12 | 18.04 | 3.77 | -0.53 | 556.09 | 532.6 | X |
| J045357.17-045059.85 | 26.36 | 5.65 | 21.03 | 4.3 | -0.63 | 776.32 | 518.75 | X |
| J082716.24-050251.01 | 17.62 | 2.26 | 22.53 | 3.99 | -0.62 | 863.17 | 506.31 | X |
| J064542.77+365019.92 | 22.34 | 6.05 | 23.74 | 3.94 | -0.64 | 563.76 | 541.15 | X |
| J063533.05+264104.75 | 8.66 | 7.07 | 31.83 | 3.39 | -0.59 | 740.83 | 536.99 | |
| J065126.35+281237.57 | 10.68 | 4.14 | 44.86 | 4.28 | -0.46 | 1224.59 | 525.95 | |
| J063431.49+270651.41 | 2.52 | 5.85 | 17.52 | 9.1 | -0.78 | 591.45 | 528.58 | X |
| J045649.71-052107.43 | 17.33 | 3.55 | 19.23 | 3.47 | -0.5 | 599.25 | 532.5 | |
| J065258.59+292553.47 | 2.2 | 3.82 | 58.05 | 3.73 | -0.38 | 873.73 | 533.13 | X |
| J065353.13+291842.71 | 21.65 | 5.33 | 29.2 | 4.23 | -0.63 | 644.58 | 535.35 | X |
| J063344.83+274319.62 | 26.95 | 7.31 | 19.9 | 4.08 | -0.49 | 543.89 | 537.44 | X |
| J064337.13+291410.01 | 2.37 | 6.3 | 38.09 | 3.64 | -0.55 | 749.32 | 541.26 | X |
| J065919.68+122028.30 | 17.01 | 5.86 | 22.24 | 3.27 | -0.7 | 561.01 | 539.26 | X |
| J173132.55+352937.44 | 2.23 | 9.28 | 49.87 | 3.85 | -0.54 | 1035.42 | 572.8 | |
| J011326.87+263336.54 | 12.49 | 5.88 | 26.68 | 3.45 | -0.6 | 637.69 | 533.47 | X |
| J085149.94+181136.17 | 5.76 | 5.18 | 77.5 | 3.45 | -0.34 | 1191.74 | 539.41 | |

*Continued on next page*

Table 3 – *Continued from previous page*

| IAU Name | Δ P.M. mas yr$^{-1}$ | Nearest Neighbor arcseconds | Total P.M mas yr$^{-1}$ | $\sigma$ P.M. mas yr$^{-1}$ | [Fe/H] dex | $V_{Total}$ km s$^{-1}$ | $V_{esc}$ km s$^{-1}$ | Infalling |
|---|---|---|---|---|---|---|---|---|
| J025347.64+323620.59 | 23.17 | 7.44 | 19.42 | 4.54 | -0.44 | 757.77 | 520.07 | X |
| J030746.77+371352.88 | 9.53 | 3.9 | 14.57 | 7.36 | -0.17 | 542.86 | 526.76 | |
| J222514.87+392654.87 | 8.93 | 5.0 | 69.71 | 3.49 | -0.4 | 1229.43 | 557.4 | |
| J070533.27+393721.42 | 19.94 | 6.76 | 18.25 | 3.92 | -0.77 | 661.2 | 519.18 | |
| J101131.78+142840.00 | 17.59 | 9.87 | 28.75 | 4.09 | -0.59 | 630.85 | 546.2 | |
| J031208.74+423108.62 | 13.16 | 1.82 | 20.12 | 4.09 | -0.5 | 561.56 | 535.85 | |
| J070103.95+293953.96 | 16.0 | 7.08 | 29.76 | 3.46 | -0.48 | 709.17 | 537.05 | |
| J070126.09+294925.06 | 1.03 | 7.12 | 37.49 | 4.44 | -0.47 | 612.51 | 548.15 | |
| J070723.06+304340.66 | 6.09 | 7.44 | 30.11 | 3.42 | -0.48 | 584.68 | 541.29 | X |
| J074801.28+181904.32 | 7.64 | 11.61 | 31.22 | 5.13 | -0.57 | 872.99 | 512.84 | |
| J022949.86+005939.54 | 20.04 | 4.39 | 14.65 | 3.83 | -0.51 | 547.27 | 533.76 | |
| J001755.41+350541.26 | 28.87 | 5.2 | 25.3 | 3.76 | -0.6 | 756.01 | 537.12 | X |

TABLE 4: Hypervelocity Candidates with 3 Flags

| IAU Name | Δ P.M. mas yr$^{-1}$ | Nearest Neighbor arcseconds | Total P.M mas yr$^{-1}$ | $\sigma$ P.M. mas yr$^{-1}$ | [Fe/H] dex | $V_{Total}$ km s$^{-1}$ | $V_{esc}$ km s$^{-1}$ | Infalling |
|---|---|---|---|---|---|---|---|---|
| J131300.50+003337.45 | 32.28 | 3.7 | 21.42 | 5.32 | -0.53 | 639.51 | 561.11 | |
| J133729.27+665608.94 | 7.23 | 3.81 | 127.2 | 5.76 | -0.7 | 614.87 | 567.17 | X |
| J053553.16+004051.61 | 23.65 | 6.32 | 25.18 | 5.05 | -0.14 | 684.4 | 534.07 | X |
| J081928.51+003548.56 | 3.29 | 5.43 | 46.39 | 5.41 | -0.12 | 635.99 | 553.59 | |
| J080837.26-000715.91 | 14.91 | 3.17 | 9.41 | 5.54 | -0.63 | 572.35 | 499.38 | |
| J095549.51+004537.44 | 2.25 | 5.51 | 65.45 | 6.01 | -0.14 | 721.58 | 560.16 | |
| J074713.75+440557.56 | 9.46 | 3.99 | 67.08 | 6.16 | -0.75 | 1544.24 | 531.71 | X |
| J212821.84+102357.30 | 8.83 | 4.53 | 58.94 | 5.61 | -0.07 | 664.57 | 576.62 | X |
| J072523.53+350313.28 | 9.22 | 4.17 | 61.39 | 6.79 | -0.44 | 1189.23 | 536.24 | X |
| J072944.56+382459.95 | 5.52 | 4.37 | 93.72 | 8.57 | -0.24 | 1689.23 | 534.24 | |
| J015016.53+143259.09 | 31.18 | 3.07 | 16.53 | 6.44 | -0.53 | 668.7 | 527.02 | X |
| J003030.11+142549.36 | 21.85 | 6.56 | 33.73 | 4.48 | -0.51 | 722.97 | 546.9 | X |
| J003132.99+142700.94 | 1.83 | 7.29 | 177.22 | 5.2 | -0.53 | 2113.89 | 555.62 | |
| J142411.12+572228.35 | 17.99 | 7.17 | 31.9 | 4.58 | -0.66 | 583.87 | 552.73 | |
| J093750.49+520739.33 | 5.2 | 4.48 | 50.03 | 7.9 | -0.59 | 658.93 | 542.68 | |
| J220348.52-010128.84 | 6.85 | 5.01 | 70.98 | 5.03 | -0.63 | 662.46 | 574.95 | X |
| J212155.72-010921.43 | 12.97 | 3.57 | 43.42 | 4.3 | -0.24 | 806.52 | 580.54 | |
| J074931.54+264335.66 | 20.63 | 3.24 | 11.12 | 5.21 | -0.43 | 534.73 | 514.38 | X |
| J222249.23+003524.95 | 1.51 | 4.97 | 59.29 | 5.21 | 0.19 | 697.1 | 573.04 | X |
| J001706.67+340346.40 | 10.19 | 5.24 | 73.34 | 6.52 | -0.63 | 1106.07 | 553.74 | X |
| J092821.06+071041.31 | 5.51 | 4.32 | 74.93 | 7.1 | -0.71 | 1345.52 | 537.86 | X |
| J032055.61+412207.99 | 5.58 | 4.6 | 68.69 | 9.35 | -0.41 | 700.82 | 551.74 | |
| J074030.04+183712.50 | 15.62 | 7.48 | 11.81 | 5.25 | -0.38 | 553.2 | 518.17 | |
| J091524.87+310005.13 | 21.16 | 4.67 | 38.22 | 4.1 | -0.4 | 1108.41 | 529.2 | |
| J074335.68+220616.73 | 9.49 | 4.23 | 31.34 | 5.21 | 0.03 | 573.74 | 542.16 | |
| J212353.46-002124.55 | 8.4 | 4.58 | 76.93 | 5.02 | -0.41 | 1648.42 | 577.07 | |
| J215906.03+004044.58 | 5.4 | 3.26 | 97.31 | 6.01 | -0.39 | 1572.89 | 572.53 | |
| J234250.52+393436.02 | 27.54 | 3.18 | 27.28 | 6.25 | -0.6 | 622.69 | 549.81 | X |
| J234414.38+430403.72 | 14.68 | 3.24 | 48.51 | 4.27 | -0.68 | 762.53 | 550.86 | |
| J222147.99+001711.67 | 707.37 | 10.0 | 707.65 | 10.61 | -0.3 | 5261.98 | 573.44 | X |
| J235103.13+360020.55 | 3.03 | 4.49 | 68.91 | 5.35 | -0.22 | 614.7 | 564.36 | X |

*Continued on next page*

Table 4 – *Continued from previous page*

| IAU Name | Δ P.M. mas yr$^{-1}$ | Nearest Neighbor arcseconds | Total P.M mas yr$^{-1}$ | $\sigma$ P.M. mas yr$^{-1}$ | [Fe/H] dex | $V_{Total}$ km s$^{-1}$ | $V_{esc}$ km s$^{-1}$ | Infalling |
|---|---|---|---|---|---|---|---|---|
| J075408.99+191118.42* | 12.06 | 11.04 | 46.96 | 7.92 | -0.34 | 1590.37 | 515.18 | X |
| J012144.78+001143.23 | 12.03 | 9.63 | 139.47 | 3.67 | -0.65 | 2231.19 | 550.39 | X |
| J021739.93+000937.94 | 26.89 | 7.75 | 30.83 | 4.29 | -0.59 | 555.11 | 552.15 | |
| J073921.43+444537.50 | 44.86 | 2.55 | 30.82 | 3.5 | -0.42 | 557.47 | 547.6 | |
| J011935.66+010127.60 | 13.13 | 15.02 | 35.85 | 6.78 | -0.73 | 862.86 | 543.93 | |
| J233707.58+495357.71 | 17.27 | 3.02 | 39.47 | 4.11 | -0.17 | 638.82 | 553.56 | X |
| J005352.32-010539.37 | 43.49 | 15.46 | 42.0 | 9.07 | -0.71 | 995.66 | 534.15 | |
| J012419.02+383757.33 | 14.69 | 4.39 | 37.51 | 4.13 | -0.49 | 617.85 | 544.06 | X |
| J092426.67+230304.36 | 15.39 | 5.92 | 44.59 | 4.02 | -0.78 | 1282.17 | 529.17 | |
| J023208.00+000501.81 | 33.25 | 5.11 | 19.9 | 5.84 | -0.62 | 728.96 | 528.8 | X |
| J030012.05+061433.53 | 24.55 | 4.29 | 19.43 | 7.07 | -0.61 | 611.08 | 528.62 | X |
| J112723.06+265823.25 | 20.7 | 27.38 | 43.86 | 6.43 | -0.73 | 1227.0 | 525.65 | X |
| J102021.54+270203.37 | 18.48 | 3.8 | 48.57 | 4.64 | -0.62 | 1463.65 | 524.46 | X |
| J182833.45+203426.74 | 26.85 | 3.82 | 24.47 | 5.48 | -0.65 | 663.9 | 591.66 | |
| J180225.43+241605.65 | 23.23 | 4.14 | 50.01 | 3.73 | -0.58 | 853.93 | 585.73 | |
| J102830.90+231840.71 | 22.57 | 28.7 | 122.42 | 5.38 | -0.71 | 966.38 | 556.05 | X |
| J183614.43+214528.91 | 4.49 | 4.7 | 30.74 | 9.25 | -0.22 | 970.16 | 588.05 | X |
| J204114.63+154335.94 | 12.97 | 4.22 | 62.78 | 3.59 | -0.33 | 1256.88 | 581.19 | X |
| J202208.61-121331.04 | 4.83 | 4.92 | 57.7 | 5.15 | -0.72 | 885.96 | 597.4 | X |
| J192443.96+372850.01 | 12.09 | 4.34 | 81.25 | 3.95 | -0.38 | 1819.08 | 572.91 | |
| J201944.82-130424.20 | 10.56 | 4.85 | 44.46 | 5.12 | -0.52 | 913.52 | 596.01 | X |
| J173331.93+080006.44 | 21.22 | 1.85 | 37.53 | 4.24 | -0.46 | 885.71 | 602.02 | |
| J003650.58+065828.59 | 13.12 | 18.87 | 64.47 | 10.54 | -0.4 | 639.58 | 564.27 | X |
| J215836.61+010714.78 | 24.62 | 3.79 | 53.65 | 4.87 | -0.41 | 633.17 | 574.67 | X |
| J112559.91+160633.94 | 18.05 | 20.37 | 43.63 | 6.73 | -0.77 | 574.75 | 560.26 | |
| J030053.81+344528.81 | 14.01 | 8.05 | 75.04 | 3.74 | -0.25 | 2027.59 | 525.44 | |
| J025450.19+333158.47 | 15.39 | 3.86 | 42.79 | 3.93 | -0.7 | 694.1 | 543.29 | X |
| J075658.96+180737.83 | 2.27 | 4.25 | 79.67 | 5.98 | -0.49 | 674.6 | 552.08 | X |
| J012336.43+393656.01 | 29.11 | 5.03 | 33.78 | 4.94 | -0.31 | 577.1 | 541.33 | |
| J202225.45+140602.39 | 19.85 | 3.75 | 33.19 | 3.95 | -0.53 | 718.42 | 585.4 | X |
| J203453.67+151745.02 | 1412.37 | 4.24 | 17.64 | 15.47 | -0.58 | 603.85 | 578.2 | |
| J113125.40-082246.17 | 20.3 | 4.11 | 22.13 | 5.73 | -0.44 | 599.13 | 546.98 | |

*Continued on next page*

Table 4 – *Continued from previous page*

| IAU Name | Δ P.M. mas yr$^{-1}$ | Nearest Neighbor arcseconds | Total P.M mas yr$^{-1}$ | $\sigma$ P.M. mas yr$^{-1}$ | [Fe/H] dex | $V_{Total}$ km s$^{-1}$ | $V_{esc}$ km s$^{-1}$ | Infalling |
|---|---|---|---|---|---|---|---|---|
| J064716.52+284807.14 | 13.07 | 7.06 | 68.87 | 4.32 | -0.1 | 763.69 | 549.03 | |
| J215649.16+462033.38 | 21.86 | 5.81 | 31.86 | 3.94 | -0.13 | 698.33 | 554.79 | |
| J064618.68+282553.77 | 6.12 | 3.6 | 47.73 | 9.92 | -0.72 | 696.66 | 548.55 | X |
| J201903.50+605636.89 | 29.21 | 3.91 | 59.58 | 3.79 | -0.72 | 1168.15 | 554.33 | |
| J073643.79+315016.42 | 14.63 | 4.21 | 65.64 | 3.56 | -0.16 | 648.62 | 552.72 | |
| J172441.15+633905.66* | 15.0 | 6.52 | 68.36 | 4.46 | -0.38 | 917.37 | 563.3 | X |
| J215948.45+451816.99 | 32.73 | 4.43 | 31.74 | 4.12 | -0.72 | 693.73 | 555.79 | X |
| J080536.09-065908.68 | 13.65 | 4.11 | 59.82 | 4.98 | -0.26 | 1041.8 | 537.73 | X |
| J075105.68+101437.34 | 24.19 | 5.05 | 22.79 | 6.24 | -0.61 | 575.31 | 522.48 | |
| J083123.42-032924.01 | 13.32 | 7.04 | 52.85 | 3.69 | -0.45 | 1713.0 | 523.57 | |
| J065138.67+365934.81 | 4.44 | 4.98 | 164.49 | 6.64 | -0.65 | 3049.94 | 531.75 | X |
| J210720.57+010344.56 | 19.58 | 4.26 | 60.65 | 3.58 | -0.51 | 1167.43 | 582.49 | X |
| J062625.69+270008.36 | 16.11 | 9.69 | 43.05 | 3.89 | -0.42 | 947.73 | 535.75 | |
| J065351.69+274904.65 | 15.68 | 3.43 | 49.19 | 4.22 | -0.23 | 1215.37 | 522.13 | X |
| J063625.61+272450.83 | 12.86 | 4.47 | 17.99 | 5.3 | -0.36 | 572.6 | 529.66 | |
| J083829.91+175601.98 | 28.93 | 17.04 | 48.91 | 7.04 | -0.63 | 1130.19 | 527.08 | X |
| J085405.73+204300.13 | 10.09 | 3.48 | 55.3 | 6.0 | -0.37 | 579.86 | 556.16 | X |
| J011957.58+243941.89 | 13.81 | 3.73 | 27.08 | 6.89 | -0.62 | 616.71 | 532.27 | X |
| J030445.87+374854.17 | 34.55 | 4.23 | 64.39 | 3.92 | -0.55 | 1104.5 | 542.2 | X |
| J085031.60+112058.04 | 130.3 | 4.89 | 125.91 | 3.47 | -0.27 | 610.85 | 561.27 | |
| J071033.40+392823.81 | 62.08 | 6.04 | 20.49 | 12.84 | -0.67 | 536.8 | 535.36 | |
| J070157.88+304405.24 | 13.73 | 4.45 | 75.95 | 4.95 | -0.78 | 1844.72 | 518.44 | X |
| J074754.55+184731.02 | 25.66 | 4.91 | 47.43 | 4.77 | -0.54 | 1414.5 | 517.51 | X |

TABLE 5: Hypervelocity Candidates with 4 Flags

| IAU Name | Δ P.M. mas yr$^{-1}$ | Nearest Neighbor arcseconds | Total P.M mas yr$^{-1}$ | $\sigma$ P.M. mas yr$^{-1}$ | [Fe/H] dex | $V_{Total}$ km s$^{-1}$ | $V_{esc}$ km s$^{-1}$ | Infalling |
|---|---|---|---|---|---|---|---|---|
| J123436.68-000558.61 | 20.6 | 5.55 | 63.47 | 6.24 | -0.75 | 1843.03 | 553.39 | |
| J105017.84-000114.84 | 18.37 | 6.31 | 196.51 | 8.12 | -0.65 | 1052.01 | 566.52 | X |
| J105300.43-002548.41 | 54.26 | 4.84 | 344.81 | 6.1 | -0.8 | 7423.47 | 544.65 | X |
| J002439.00-093916.87 | 312.99 | 3.89 | 341.35 | 10.14 | -0.41 | 3041.23 | 564.69 | X |
| J004948.97+153108.51 | 19.78 | 5.77 | 299.61 | 7.93 | -0.13 | 886.96 | 567.42 | |
| J205316.53-010616.55 | 37.9 | 1.42 | 400.31 | 9.22 | -0.21 | 9342.34 | 585.19 | |
| J035429.27-061354.14* | 21.98 | 6.74 | 46.21 | 7.81 | -0.55 | 906.39 | 542.44 | |
| J012925.63-005902.43 | 13.46 | 3.61 | 69.71 | 5.11 | -0.53 | 1313.91 | 543.4 | |
| J160600.59+050742.39 | 15.61 | 4.59 | 49.12 | 6.33 | -0.52 | 796.31 | 588.02 | X |
| J001720.40+343634.12 | 25.63 | 6.34 | 31.25 | 8.12 | -0.58 | 799.09 | 542.95 | X |
| J100636.50+451652.40 | 13.49 | 4.93 | 44.45 | 7.89 | -0.78 | 804.41 | 539.87 | X |
| J143406.17+563047.24 | 433.3 | 9.42 | 437.58 | 7.0 | -0.5 | 3637.42 | 565.09 | X |
| J113931.63+472307.94 | 34.93 | 2.64 | 246.48 | 7.53 | -0.37 | 1531.55 | 562.68 | |
| J095529.80+415221.37 | 15.32 | 8.43 | 42.41 | 7.41 | -0.64 | 791.4 | 533.01 | X |
| J131425.40+415004.09 | 20.37 | 5.62 | 87.27 | 5.9 | -0.65 | 1526.26 | 549.87 | |
| J031230.47+415649.00 | 25.5 | 4.1 | 133.72 | 11.66 | -0.16 | 850.12 | 559.21 | X |
| J165032.70+303416.31 | 13.46 | 7.78 | 48.01 | 6.99 | -0.6 | 821.46 | 577.39 | |
| J213616.03+745923.91 | 369.35 | 5.96 | 369.8 | 11.0 | -0.12 | 1700.71 | 566.76 | X |
| J110316.01+380029.06 | 212.65 | 6.11 | 369.71 | 13.53 | -0.36 | 2763.48 | 560.31 | |
| J213206.91+002644.79 | 18.77 | 6.28 | 41.71 | 7.33 | -0.64 | 586.9 | 578.05 | |
| J031104.34+414435.59 | 33.95 | 3.97 | 88.12 | 7.35 | -0.44 | 1100.04 | 542.62 | X |
| J074140.00+171608.72 | 32.49 | 9.05 | 33.26 | 5.42 | -0.54 | 904.26 | 515.74 | X |
| J211821.44+000955.26 | 26.96 | 5.24 | 45.36 | 6.67 | -0.52 | 755.72 | 579.89 | |
| J074728.85+185520.49 | 68.75 | 9.14 | 58.08 | 8.13 | -0.24 | 697.28 | 539.31 | X |
| J073040.22+410043.40 | 12.5 | 5.73 | 40.32 | 7.32 | -0.32 | 567.7 | 547.01 | X |
| J233604.89+495742.45 | 21.79 | 3.35 | 75.17 | 7.05 | -0.64 | 1432.36 | 549.37 | |
| J233901.30+492300.94 | 18.8 | 3.14 | 34.8 | 7.98 | -0.18 | 679.08 | 551.28 | X |
| J164601.29+205702.81 | 18.3 | 8.78 | 58.29 | 7.61 | -0.66 | 1105.45 | 584.21 | |
| J185443.02+190540.09 | 15.47 | 3.66 | 36.87 | 5.99 | -0.42 | 624.29 | 588.36 | |
| J132239.99+260222.75 | 16.08 | 8.1 | 43.54 | 6.84 | -0.78 | 773.15 | 552.77 | |
| J183445.62+220630.69 | 43.51 | 4.39 | 71.84 | 12.82 | -0.18 | 724.41 | 584.62 | |

*Continued on next page*

Table 5 – *Continued from previous page*

| IAU Name | Δ P.M. mas yr$^{-1}$ | Nearest Neighbor arcseconds | Total P.M mas yr$^{-1}$ | $\sigma$ P.M. mas yr$^{-1}$ | [Fe/H] dex | V$_{Total}$ km s$^{-1}$ | V$_{esc}$ km s$^{-1}$ | Infalling |
|---|---|---|---|---|---|---|---|---|
| J180956.29+232555.23 | 14.97 | 3.78 | 57.61 | 6.15 | -0.67 | 590.76 | 585.5 | |
| J204900.31+154852.38 | 25.6 | 4.96 | 36.9 | 5.16 | -0.32 | 1562.71 | 552.88 | |
| J092504.84+190140.91 | 24.0 | 9.0 | 42.14 | 6.93 | -0.37 | 1200.57 | 524.26 | X |
| J225842.81+063935.96 | 20.93 | 5.62 | 32.13 | 6.55 | -0.31 | 565.05 | 563.64 | X |
| J073849.89+415907.92 | 109.89 | 4.18 | 169.6 | 11.18 | -0.44 | 1729.39 | 548.6 | |
| J061841.20+644628.63 | 159.39 | 5.58 | 148.18 | 6.8 | -0.66 | 1823.6 | 545.06 | |
| J201920.70+594519.14 | 16.0 | 3.34 | 46.41 | 5.04 | -0.68 | 842.05 | 558.94 | X |
| J203349.13+153932.88 | 330.96 | 5.87 | 341.56 | 7.83 | -0.45 | 1316.84 | 576.62 | |
| J080930.63-075408.47 | 22.92 | 5.32 | 84.16 | 9.3 | -0.14 | 743.39 | 553.9 | |
| J064443.12+274626.59 | 288.59 | 4.24 | 300.06 | 6.8 | -0.64 | 5327.33 | 534.31 | X |
| J023431.41+284438.98 | 47.81 | 3.97 | 42.86 | 9.56 | -0.64 | 1444.28 | 520.24 | X |
| J233942.12+082827.22 | 12.71 | 4.95 | 71.74 | 5.37 | -0.64 | 568.53 | 563.91 | |

# Acknowledgements

First and foremost, I appreciate my family for being supportive, interested, involved and encouraging. But most of all I would like to thank my mother for teaching me to always question: authority, precedence and 'the way things are.'

I would like to thank Professor Heidi J. Newberg, who introduced me to science proper, gave me a chance, criticized only in a constructive manner, invited me to barbecues, and, most importantly, let me make mistakes.

I also thank Professor Eva K. Grebel, who allowed me to work on what I wanted to work on and to just explore, treated me as a peer rather than a subordinate, and graciously always makes time for everyone.

I extend my kindest regards to Dr. Dr. Avon P. Huxor, my office mate. While we may disagree on who writes the betterest English, and on the appeal of the violin, I'm quite pleased to have spent three years sitting across from him and think his taste in cinema and music is super-par.

Special thanks to Prof. Martin C. Smith for hosting my visit to Shanghai and inviting me back to work with him. He's an excellent host and exciting to work with.

Many thanks to Dr. Coryn Bailer-Jones, for being my second referee; and to Professor Luca Amendola and Dr. Thorsten Lisker for agreeing to finish up my examination committee.

Other persons of note are: Dr. Bertrand Goldman, Dr. Veronica Lora, Dr. Anna Pasquali and Dr. Siegfried Röser..

I am grateful for the generous support provided by the Marie Curie Initial Training Networks [grant number PITN-GA-2010-264895 ITN "Gaia Research for European Astronomy Training"]. I am also a fellow at the International Max Planck Research School for Astronomy and Cosmic Physics at the University of Heidelberg and a member of the Heidelberg Graduate School for Fundamental Physics.

*The sun was shining on the sea,*
*Shining with all his might:*
*He did his very best to make*
*The billows smooth and bright*
*– And this was odd, because it was*
*The middle of the night.*

*The moon was shining sulkily,*
*Because she thought the sun*
*Had got no business to be there*
*After the day was done*
*– "It's very rude of him," she said,*
*"To come and spoil the fun!"*

*The sea was wet as wet could be,*
*The sands were dry as dry.*
*You could not see a cloud, because*
*No cloud was in the sky:*
*No birds were flying overhead*
*– There were no birds to fly.*

*In a Wonderland they lie*
*Dreaming as the days go by,*
*Dreaming as the summer die.*

- Lewis Carroll